Sustainable Recycling of Spent Lithium–ion Batteries

An In-situ Approach for Recovery and Alloying of Valuable Metals

Safoura Babanejad

Process Metallurgy

LULEÅ
UNIVERSITY
OF TECHNOLOGY

Sustainable Recycling of Spent Lithium-ion Batteries

An In-situ Approach for Recovery and Alloying of Valuable Metals

Licentiate Thesis

Safoura Babanejad

Division of Mineral and Metallurgical Engineering
Department of Civil, Environmental, and Natural Resources Engineering
Luleå University of Technology
Luleå, Sweden

April 2023

Acknowledgements

Summary

A large number of Li-ion batteries used today will reach their end-of-life (EOL) in a few years. After their EOL, the recovery of their precious elements is required. By applying physical separation, a fraction with fine particle size is left behind which is known as black mass (BM). BM is rich in LIB precious materials, including Li metal oxides and graphite. In this study, pyrometallurgical recycling of BM is investigated. In the first step, the BM high-temperature transformations are being studied, focusing on reducing Li metal oxides, Li evaporation, and F removal. In the second step, Fe and Cu oxides are added to the BM to investigate how the graphite remaining in the BM can be used as a reducing agent and form alloys with Co and Ni. The use of mechanical activation as a mean to improve the kinetics of the reactions and the efficiency of the reduction reaction was also studied. To model the experiments in this study, thermodynamic softwares (FactSage and HSC) were also employed.

Abstract

When Li-ion batteries (LIBs) reach their end-of-life, they are collected, discharged, and mechanically disintegrated. Plastic and metallic streams are separated after this process, and finally, a small particle size fraction called black mass (BM) is obtained. BM is normally composed of graphite, Li metal oxide, Al, Cu, and some polymeric materials like binders. Pyrometallurgical recycling of BM, which is the focus of this study, is an available method for recovering the BM valuable elements. BM samples from two types of LIBs were used to investigate the high-temperature transformations occurring in the BM. Thermal analyses alongside mineralogical and morphological analyses demonstrate that the decomposition of binders is done up to a temperature of 500 °C, which leads to the volatilization of hydrocarbons (not F) from BM. At a temperature of ~600 °C, Li metal oxide transforms to simpler metal oxides and by increasing the temperature to 1100 °C, Co and Ni oxides completely reduce to their metallic forms, and Li forms $LiAlO_2$ and LiF.

After studying the high-temperature behaviour of BM as the basics of a pyrometallurgical method, some of this method's downsides were taken into account, i.e., graphite loss and high energy consumption. A solution is proposed in this study by the addition of external metal oxides (Fe_2O_3 and CuO) to consume the graphite in the BM during the reduction, which results in the production of Fe/Cu-based alloys, containing Co and Ni (in the BM) as alloying elements. Regarding high energy input in pyrometallurgy methods, mechanical activation is applied in both BM reduction and alloying processes to improve the kinetics of the reaction and shift the reduction to a lower temperature range. This shift in the reduction temperature makes changes in the ratio of reduction products, i.e., the ratio of $CO:CO_2$ decreases by decreasing the temperature. Thus, in the reduction of metal oxides, the consumption of C becomes lower and consequently, more metal oxides can be added to be reduced.

The study improves our knowledge of high-temperature transformations and F behavior during medium-temperature treatments of BM from LIBs. It proposes a solution to efficiently use excess graphite and overcome the downsides of pyrometallurgy methods by utilizing external metal oxides and applying mechanical activation for in-situ reduction and alloy-making.

Keywords: Li-ion battery, black mass, recycling, pyrometallurgy, thermal analysis, fluorine, mechanical activation, alloying, graphite.

Table of contents

List of Publications

- **Babanejad S**, Ahmed H, Andersson C, Samuelsson C, Lennartsson A, Hall B, Arnerlöf L. High-Temperature Behavior of Spent Li-Ion Battery Black Mass in Inert Atmosphere. Journal of Sustainable Metallurgy. 2022;8:566-581

- **Babanejad S**, Ahmed H, Andersson C, Heikkinen E-P. Mechanical activation-assisted recovery of valuable metals from black mass in the form of Fe/Cu alloys. Journal of Sustainable Metallurgy. 2023.

List of Tables

List of Figures

1 Introduction

In recent years, attention has been drawn to a future low-carbon economy, where renewable energies play a critical role (1). The attempt is to reduce the consumption of fossil fuels and subsequently the amount of greenhouse gases emitted to the atmosphere (2). In this regard, electric vehicles have been introduced, which are completely dependent on the functionality of rechargeable batteries (3). Besides electric vehicles, rechargeable batteries are also required in the development of portable electronic devices, e.g., mobile phones, tablets, and laptops (4).

A variety of rechargeable batteries, such as Pb-acid, Ni-Cd, Ni-metal hydride, and Li-ion batteries (LIBs), have been introduced so far (4,5). Among them, LIBs with their incomparable properties, i.e., high energy density and voltage, low self-discharge, simple operation, light weight, and long lifetime, has become the most popular type of rechargeable batteries that are utilized nowadays. In 1991, Sony Corporation commercialized LIBs for the first time, when their properties were introduced in portable electronic devices. The specific energy of these batteries is twice that of standard Ni-Cd batteries and the voltage is three times that of regular Ni-based batteries (4,6).

With the drastic increase in using electric cars, it is expected that it will be required to recycle 850 thousand LIBs by 2025. As a consequence of the European commission regulation (2020), by 2025, 65 % of portable batteries should be collected, the efficiency of recycling should reach 65 %, and it will be mandatory to have a minimum recovery rate of 90, 90, 35, and 90 % for Co, Ni, Li, and Cu, respectively. All recyclers will also be obligated to declare the C footprint of the recycling process (7,8).

2 Background

2.1 Composition of LIBs

Different types of LIBs have been introduced so far, offering different properties. The intended application of the LIB determines the property that should be provided, for example if it is required to have a high energy or power density, if it matters to have a moderate cost, or if it is needed to have a long lifetime. To acquire the required properties, various LIBs have been designed by changing their main components, which are cathode, anode, electrolyte, separator, current collectors, binder, and casing. These components are briefly described below (9):

- Cathode

Cathode active materials can be classified into intercalation and conversion cathode active materials, among which the intercalation materials are the most popular ones, because of their higher operating voltage that leads to higher energy storage. In this type, the cathode active material is a solid network where the ions (Li ions in these batteries) can enter and leave this structure reversibly. The network structure can be layered, spinel, olivine, or tavorite (2). $LiCoO_2$ (LCO) with a layered structure is the first commercialized material. $LiNi_xCo_yMn_{1-x-y}O_2$ (NMC), $LiNiO_2$, $LiMn_2O_4$, $LiFePO_4$, and $Li(NiCoAl)O_2$ are also popular materials used in the cathodes. The advantageous properties of NMC (i.e., structure stability, relatively low cost, high discharge capacity, and good performance in the cyclic properties) make this material a superior candidate for cathodes, especially in electric vehicles (10).

- Anode

The main anodes that are utilized today are graphitic and $Li_4Ti_5O_{12}$ (2). The first commercialized anode material, and still the most popular one, is graphite, with its good electrochemical and physical properties, availability, and moderate price, although it lacks a proper volumetric capacity. Si is the common additive to graphite for solving this issue. The design of anodes usually varies based on its structure, not the material (9,11). $Li_4Ti_5O_{12}$ is a costly anode material, although popular yet due to its outstanding properties, like high thermal stability, volumetric capacity, and cycle life (2).

- Electrolyte

The electrolyte mainly consists of solvents and solutes. Electrolyte's role is to facilitates transferring of ions between the cathode and anode. Different combinations can be used in electrolytes: $LiClO_4$, $LiBF_4$, and more popularly $LiPF_6$ are used as solutes, while solvents can be a mixture of cyclic and linear carbonate esters, e.g., a mixture of propylene carbonate and diethyl carbonate (10,12).

- Separator

The separator is a polymeric material, which works as a selective barrier; it lets the Li ions pass while inhibiting the electrons and accordingly preventing short-circuit between the cathode and anode. Polyethylene and polypropylene are the most popular materials used for this matter (10,13).

- Current collectors

Current collectors are bridges connecting the electrodes to the external circuits, properties of which affect the performance of LIBs, such as capacity and stability. The conventional materials that are commercially used are Al and Cu in the cathode and anode, respectively, although other materials, like Ni, Ti, and carbonaceous materials, have been introduced for the next generation of these batteries (14).

- Conductive agent

Acetylene black is one of the popular agents that is added to the cathode/anode to enhance its conductivity (6,13,15).

- Binder

Binder maintains a bond between the cathode/anode active material, current collectors, and acetylene black. Polyvinylidene fluoride (PVDF, the most commonly utilized binder) and polytetrafluoroethylene are two polymeric materials used as binders (6,10,16,17).

- Casing

The batteries are packed in a casing to protect the inside (especially electrolyte as a reactive material in an oxidative atmosphere) from the surrounding atmosphere. The material used should be inert to avoid interaction with any chemical reactions occurring in the battery (13).

2.2 Recycling of LIBs

The cost breakdown of the LIBs shows that most of the cost in their manufacturing is primarily related to the cathode active materials and secondly to the anode materials (mainly graphite) (9). Co as one of the main components in the cathodes plays a crucial role in the LIBs' production costs. Furthermore, the increase in demand for the LIBs and the limitation in the Li resources on the earth's crust indicate that there will be a depletion in the Li resources, and an inclining price for this material is expected in the future (2).

After discharging and dismantling the LIBs, the casing and the majority of current collectors will be separated from the battery components, employing different techniques like comminution, classification, magnetic/electrostatic/gravity separation, and froth flotation (10,18–20). This process produces a material, rich in cathode and anode materials, which is called black mass (BM) (21,22).

The BM is commonly the input stream in the recovery of precious elements from LIBs, which can be done by hydrometallurgical, or pyrometallurgical techniques, or a combination of these two (10).

2.2.1 Hydrometallurgy

Hydrometallurgy includes a variety of processes, i.e., leaching, separation, solvent extraction (SX), precipitation, and electrowinning. The combination of these methods will lead to different procedures. Many studies have been done in this area (23–31). For instance, Li and other metals in the cathode active material were extracted from spent LIBs by Chen et al. (23), using two steps of leaching followed by carbonation. Yang et al. (24) employed leaching and SX to produce MnO_2, Li_2CO_3, Co, and $NiSO_4$, in four steps of acid-leaching, co-extraction of Mn and Co, Ni/Li separation, and Co/Mn separation. It is essential when using a hydrometallurgical method to separate the anode from the cathode material since the anode interferes with the recovery of cathode elements during the leaching steps (32). *Recupyl* process is an example of a commercial application of hydrometallurgical method, including hydrolysis, three leaching steps, and electrolysis, which leads to the recovery of Li, Co, and Cu (21). In another hydrometallurgy recycling process, *Batrec*, after pretreatment and passivation steps, acid leaching, followed by SX and precipitation steps will result in the recovery of metallic elements from cathode active material (33).

2.2.2 Pyrometallurgy

Pyrometallurgy includes the processes that deal with heating the BM to extract the valuable metals. These processes can be divided into two groups: medium-temperature and high-temperature processes. The first group represents the methods where the materials will remain in the solid state, e.g., pyrolysis, incineration, and roasting. The second group consists of the methods that smelt the BM, and subsequently metallics are collected in the melt (32).

- Medium-temperature pyrometallurgy

Roasting of the cathode active material (650-1000 °C) with graphite in the anode is one of the most popular ways for reducing the cathode active material, which leads to the production of Co/Ni, Li_2CO_3, while part of the graphite remains unreacted (34,35). In some cases, salt is added in the roasting process to produce materials with better leachability, e.g., sulfation, nitration, and chlorination roasting (32). For instance, in a study, water leaching has been done after chlorination

roasting where over 98 % recovery of Li, Ni, and Co, and 97% of Mn were reached (36). These approaches aim at recovering all precious elements in the battery, including Li, with lower consumption of energy, acid, and alkaline. In some cases, like sulfation roasting, the process generates corrosive gases, which is still a challenge in the commercialization of these methods (37).

- High-temperature pyrometallurgy

X. Hu et al. (38,39) did a high-temperature process (at 1600 °C) on BM in laboratory- and pilot-scale (electric arc furnace) to obtain a Co-Ni-Mn melt. In their study, Li reacted with the existing Al and formed $LiAlO_2$ in the slag and the rest formed Li_2CO_3 and LiF that were collected in dust. In this method, all C was lost during oxidation in the air atmosphere. In these processes, by the addition of slag formers, Li can be accumulated in the slag. R. Guoxing et al. (40) reached a Li content of 2.63 wt.% in slag, by controlling the MnO/SiO_2 ratio and Al_2O_3 content. 64.1-82.4 % of Li recovery yield by addition of SiO_2 (in form of Li aluminosilicate) is reported in another study, with Li content of 5.18-7.40 wt.% in the slag (41). In another study, the melting was done to collect Li in the slag and extract it from the slag by acid leaching. In this study, although a slag with 2.83 wt.% of Li_2O was obtained, only 50.28 % of that could be recovered in the following leaching step (42). In *Inmetco*, as a LIB recycling plant, batteries are smelted and Co, Ni, and Fe are collected in the melt, while slag (containing Li) is disposed (43). On a commercial scale, recovering Li from slag by hydrometallurgy processes after smelting is being done in *Umicore* (44,45).

Some studies have been done so far to investigate the high-temperature behaviour of BM. Kwon and Sohn (46) investigated the thermos-kinetic behaviour of LCO and C mixture. They proposed thermodynamically feasible reactions at different temperatures. Based on their observations, it is possible to find Co_3O_4 in the BM, because of the probable changes in the LIB chemistry during charging and discharging. At 810 °C, CoO, and Li_2CO_3 are the abundant phases in the sample. Furthermore, they recommended the temperature range of 880-1200 °C as the optimal range for recovering Co and Li. Li et al. (47) focused on the pyrolysis of LCO and C mixture and proposed Eq. 1 as the overall reaction in the temperature range of 500-800 °C.

$$4\ LiCoO_2 + 3\ C\ \rightarrow 2\ Li_2CO_3 + 4\ Co +\ CO_2$$
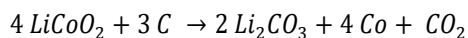
Eq. 1

Wang et al. (48) studied the high-temperature behaviour of NMC cathodes (without anode). This study demonstrated the transformation of NMC to CoO, NiO, and $LiAlO_2$ during an exothermic

thermite reaction at 557.7 °C.

There are few studies that focus on emission of hazardous F-containing gases in pyrometallurgical recycling of LIBs. Liu et al. (49) studied the high-temperature of LIBs with $LiFePO_4$ as the cathode material during pyrolysis at 450–650 °C. They demonstrated that the main sources of F in these batteries were electrolyte and PVDF. They stated that the F content in the battery reached 0.067 wt.% after pyrolysis. In another study, it is suggested to add CaO in order to capture F during decomposition of PVDF and form CaF_2. By applying this method, the emission of F-containing gases can be avoided (50).

2.2.3 A comparison between pyro- and hydrometallurgy

These two major routes of LIBs' recycling were explained in two previous sections. The question is how to select a proper method to recycle these batteries. To answer this question, a comparison between the pyro- and hydrometallurgy-based recycling methods is listed in Table 1. Pyrometallurgy, regardless of high capital cost, is an easier process compared to hydrometallurgy, since it is not necessary to apply a pretreatment method, and it is compatible with a variety of LIB types. Besides, the existing plants can be used, and it is not required to establish a plant for that purpose. Having these advantages in mind, the big problem with this process is the loss of Li to the slag, which is not easy to recover by hydrometallurgical processes and is reported to be disposed in some of the commercial processes. And, although the oxidation of graphite (in electric arc furnace) is an energy source for the reduction reaction, it is not an adequate reason for consuming graphite. The oxidation of graphite (and thus production of CO/CO_2) and emission of F-containing gases is another issue that makes this method environmentally unfavorable. By employing hydrometallurgical methods, these issues can be solved, since it does not deal with the production of large amount of off-gases, possesses a high recovery rate of Li, and does not need a high energy input since it is feasible at room temperature. Although the hydrometallurgical routes have many advantages, it bears some downsides; The process necessitates a pretreatment step to prepare it for leaching and even though, it does not produce off-gas, it produces large amounts of wastewater (32,37,51).

Table 1. Advantages and disadvantages of pyro- and hydrometallurgical processes in the recycling of LIBs (37,51)

Process	Advantages	Disadvantages
Pyrometallurgy	Easy process Easy to scale up Acid/Alkaline-free Easy (or no essential) pretreatment Optimized ready technology Generating energy (input) during exothermic reactions	Li loss in slag High energy input Off-gas emission High capital cost
Hydrometallurgy	Li recovery Room temperature High purity No off-gas emission	Complicated process Pretreatment required Producing wastewater

2.3 Aims and Objectives

- Investigation of the high-temperature behaviour of BM

As stated in the previous section, several studies have been conducted to investigate the high-temperature behaviour of BM. In most of these studies, the heat treatment was done on selective parts of the LIB, i.e., cathode and anode active materials that are separated manually and heated under different atmospheres, which would not be feasible at a commercial scale. Studies done on industrial BM are limited and hence, in the current research, BM pretreated at Stena Recycling AB has been employed. Furthermore, the BM composition is not fixed and can easily vary by changing the input LIBs. Thus, the LCO and NMC BM were investigated separately to follow if the cathode active material type can affect the employed pyrometallurgical process.

Furthermore, an element that is critical in high-temperature processes is F, which is assumed to be removed during medium-temperature heat treatments, by dissociation of electrolyte and PVDF. To examine the validity of this assumption, some trials have been designed and carried out in this study to follow the F presence in the BM after medium-temperature treatments.

- Utilization of graphite in the BM to produce Fe/Cu-based alloys

When heating the BM, graphite can act either as a source of energy (by oxidation in an exothermic reaction) or a reducing agent (for the reduction of the cathode active material), depending on the existing atmosphere. In the first condition, graphite burns out, while in the second condition, most of it remains unreacted and will thus need to be separated in the following recovery steps. In this study, external metal oxides (MeOs) (Fe_2O_3 and CuO) are added to the BM, to investigate if it is possible to benefit from the graphite in the BM in reducing MeOs, and if it is feasible to produce a Fe/Cu-based alloy, containing Co and/or Ni as alloying elements.

- Investigation of the effect of mechanical activation on the BM reduction and the alloying process

As mentioned in section 2.2.3, one of the main disadvantages of pyrometallurgical processes is the high energy input that is required to trigger the reactions. Hence, mechanical activation is employed in this study to investigate if it lowers the required energy by improving the reactions' kinetics.

3 Materials and Method

3.1 Materials

Two types of LIBs have been considered in this study: LIBs from small portable batteries (cathode active material: LCO) and LIBs from car batteries (cathode active material: $LiNi_{0.33}Mn_{0.33}Co_{0.33}O_2$ (NMC111)[1]). The original cells are shown in Fig. 1. After mechanical treatment, physical separation, and low-temperature heat treatment (250-300 °C), BM has been obtained from these spent LIBs.[2] Two particle size ranges, the first consisting of particles smaller than 150 μm and the second of particles between 150 and 700 μm were studied separately.
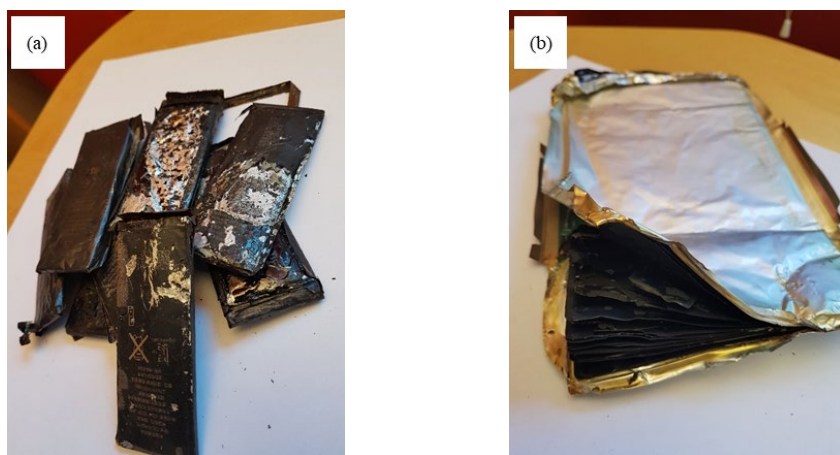
Fig. 1. The original batteries used as the source of BM: (a) mobile batteries, and (b) car batteries.

Pure synthetic materials, LCO (99.8 %, Aldrich), graphite (−300 mesh, 99 %, Alfa Aesar, and APS 7–11 micron, 99%, Alfa Aesar), Al (+325 mesh, 99.5 %, Alfa Aesar), and PVDF (HSV 900, Arkema) were utilized in order to conduct some complementary experiments concerning LCO transformation. Fe_2O_3 (−325 mesh, 98 %, Alfa Aesar) and CuO (97.5 %, AnalaR NORMAPUR) pure materials were also utilized to form Fe- and Cu-based master alloys, respectively.

---

[1] NMC111 is the only NMC-type battery that has been used in this research. Hence, the abbreviation NMC will be used instead of NMC111 hereafter.

[2] The BM samples were prepared at Stena Recycling AB.

3.2 Method

3.2.1 Characterization of BM

- Chemical analysis

Inductively coupled plasma–mass spectrometry (ICP–MS) was the main method employed in the chemical analysis of BM, performed according to SS EN ISO 17294–2:2016 and EPA method 200.8:1994. C content was measured by LECO CS230, a combustion analyzer, and EA3000, a CHNS-O elemental analyzer. The ion selective electrode (ISE) method was the approach to analyze the F content of samples, applying EPA method 9214.

- Morphological and mineralogical analysis

The morphology of the as-received BM samples was observed under a Zeiss Merlin field emission gun scanning electron microscope (SEM) equipped with an Oxford Instruments X-Max energy dispersive X-ray spectroscopy (EDS) detector with Aztec software. Particle Size Distribution (PSD) was done by Retsch Camsizer XT. X-Ray Diffraction (XRD) (using PANalytical Empyrean X-ray diffractometer) was the method employed for the mineral characterization in this study (details can be found in paper I). The same XRD instrument, equipped with an Anton Paar HTK 1200 N high-temperature chamber, was used to identify the developed phases upon heating up to a temperature of 1000 °C at a heating rate of 10 °C/min in He atmosphere. To achieve an accurate sample temperature, the sample was held at the set temperature for 1 min before the scan started. The obtained diffractograms were evaluated by HighScore Plus (v4.7, PANalytical B.V., Almelo, The Netherlands) software, and FIZ-NIST Inorganic Crystal Structure Database (ICSD) and Crystallography Open Database (COD) databases.

3.2.2 High-temperature behaviour of BM

A Netzsch STA 409, a thermogravimetric/differential thermal analyzer (TGA/DTA), was employed to investigate the high-temperature behaviour of BM in inert atmosphere (Ar), with a heating rate of 10 °C/min. The evolved gases in the experiments were continuously monitored using a quadrupole mass spectrometer (QMS) for qualitative analysis. During these trials, two phenomena were investigated more deeply in parallel which are listed below:

- LCO transformation

To identify the influential element(s) in the transformation of cathode active material, the BM

composition was simulated by synthetic materials, listed in Table 2. The ratios were set based on the LCO BM composition. The same heating profile, as applied for the industrial prepare BM, was applied to these synthetic mixtures to run TGA and DTA.

Table 2. The chemical composition used in the complementary experiments: LCO transformation

Sample	(g)				(wt.%)			
	LCO	Graphite	Al	PVDF	LCO	Graphite	Al	PVDF
LCO	55.9	-	-	-	100.0	-	-	-
LCO+Gr	55.9	35.4	-	-	61.2	38.8	-	-
LCO+Gr+Al	55.9	35.4	0.9	-	60.6	38.4	1.0	-
LCO+Gr+Al+PVDF[3]	55.9	35.4	0.9	4.42	57.9	36.6	0.9	4.6

- Fluorine behaviour

Since the presence of F at high temperatures is an important influencing factor, to investigate the effect of medium-temperature treatment on F removal, the F content in the NMC BM was studied in four different parts of the recycling process:

(i) NMC BM before heating at 250–300 °C (see "Materials" section);

(ii) the as-received NMC BM (heated at 250-300 °C);

(iii) NMC BM after pyrolysis for 1 h at 700 °C (in an Ar atmosphere); and

(iv) NMC BM after incineration for 1 h at 700 °C (in a synthetic air atmosphere).

The F content after each treatment was analyzed following the ISE method.

3.2.3 Alloying

Two types of MeOs (Fe_2O_3 and CuO) were added to the BM to consume graphite in the BM as a reducing agent. High-temperature treatment of these mixtures produced a Fe/Cu-based alloy. Reaching a net C/O molar ratio of one in the MeO-BM mixture was considered in the addition of MeO to the BM (Eq. 2).

$$\frac{C}{O} = \frac{C_{BM}}{O_{Cathode\ active\ material} + O_{MeO}} = 1$$

Eq. 2

---

[3] Due to the experimental limitations at that time, this experiment (LCO+Gr+Al+PVDF) was done using graphite with the particle size of 7–11 µm, while the graphite used in the other experiments was -300 mesh.

3.2.4 Mechanical activation

Mechanical activation is known as a method for improving energy consumption in high-temperature processes (52–60). In this regard, the BM and MeO-BM mixtures were mechanically activated by using a Fritsch Pulverisette 7 Planetary micro mill. The number of hardened balls, sample-to-ball ratio, and rotating speed was fixed, while the milling period was varied in these tests. Details can be found in paper II.

3.2.5 Alloying trials

The same TGA (Netzsch STA 409) as employed earlier was used to produce Fe/Cu-based alloys. The samples were heated at a rate of 10 °C/min up to 1450 and held at that temperature for 1 h. Afterward, they were cooled to 200 °C at a rate of 20 °C/min.

3.3 Thermodynamic Investigation

Thermodynamic calculations were applied as a supporting tool in this study. The softwares used were FactSage 8.0 and HSC chemistry v. 10.0.7.

- FactSage

This software was used to predict the thermodynamically stable phases at elevated temperatures, and following that, to study the possible occurring reactions (61). To achieve this goal, the *Equilib* module was used, employing *FactPS*, *FToxid*, and *FTmisc* databases. *Ideal gas*, *pure solids,* and the following solution phases were considered as the species in this modeling: *FToxid-SLAGA, FToxid-SPINA, FToxid-MeO_A, FToxid-NAShB, FToxid-NASlB.* In the simulation of the alloying process, *FTmisc-FeLQ* and *FTmisc-CuLQ* were added for Fe- and Cu-based alloyed, respectively.

- HSC chemistry

As explained before, energy consumption is one of the important factors that affect the efficiency of pyrometallurgical processes. Accordingly, HSC chemistry software has been used to perform the mass and energy balance calculations in the alloying processes to have an estimation of the carbon footprint and energy consumption. The input and output flows were designed as demonstrated in Fig. 2. The compounds in the output flows were set based on the XRD data and the FactSage modeling.
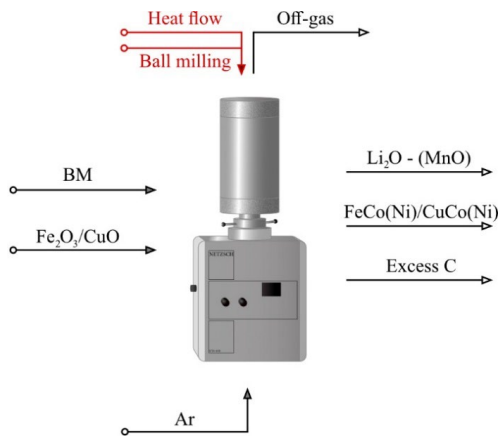
Fig. 2. Input and output flows used in mass and energy balance (62).

4 Results and Discussion

4.1 Characterization of BM

4.1.1 Chemical analysis

Table 3 lists the chemical compositions of LCO and NMC BM in the two particle size fractions. It can be observed that the composition of the two fractions is almost similar in the LCO BM, while in the NMC BM, the C content of the coarse fraction, compared to the fine fraction, is higher. Li, Co, Ni, and Mn (in the NMC BM) originate from the cathode active material, and C mainly represents the graphite existing in the anode material. As mentioned in section 2.1, Al and Cu are the materials that were used as current collectors in the electrodes. Si, P, and F are the additives employed in the anode to improve its performance. Beside the F presence in the anode and electrolyte, the main source of F in the BM is the binder, PVDF (2,63).

Table 3. Chemical compositions of LCO and NMC BM in two fractions of < 150 and 150–700 µm (wt.%)

Element (wt.%)	Li	Co	Ni	Mn	Al	Cu	Si	P	F	C
LCO < 150 µm	3.8	31.4	0.0	0.0	0.4	0.4	1.6	0.4	2.1	43.8
LCO 150–700 µm	4.0	32.3	0.0	0.0	0.9	0.6	1.6	0.5	2.6	35.4
NMC < 150 µm	6.3	17.3	15.5	15.1	0.0	0.8	1.3	0.4	4.9	12.8
NMC 150–700 µm	3.6	8.0	7.3	7.6	0.2	1.6	1.0	0.6	6.5	43.2

4.1.2 Mineralogical and morphological investigation

Diffractograms from XRD measurements are presented in Fig. 3. Based on these data, the main phases in both types of BM originate from the cathode and anode materials.
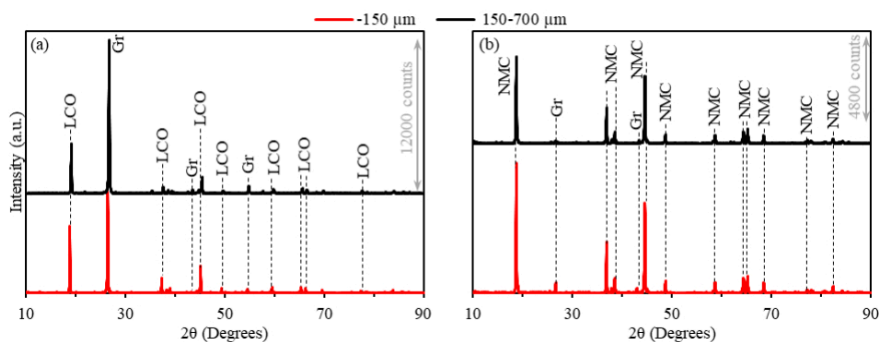
Fig. 3. XRD patterns of (a) LCO and (b) NMC BM (64).

The morphology of LCO BM is shown in Fig. 4. There are irregular and sheet-like particles in a

wide range of sizes, and large particles which are agglomerates of smaller particles. The agglomeration could possibly be caused by the residual binder or be a consequence of the physical properties of the particles, i.e., size and surface. The chemical analysis by EDS showed that the sheet-like particles mainly consist of C, hence graphite from the anode material (a1 and b3 spectra), while the other types of particles had a mixed composition rich in Co, which could be derived from the cathode active material (a2, a3, b1, and b2).
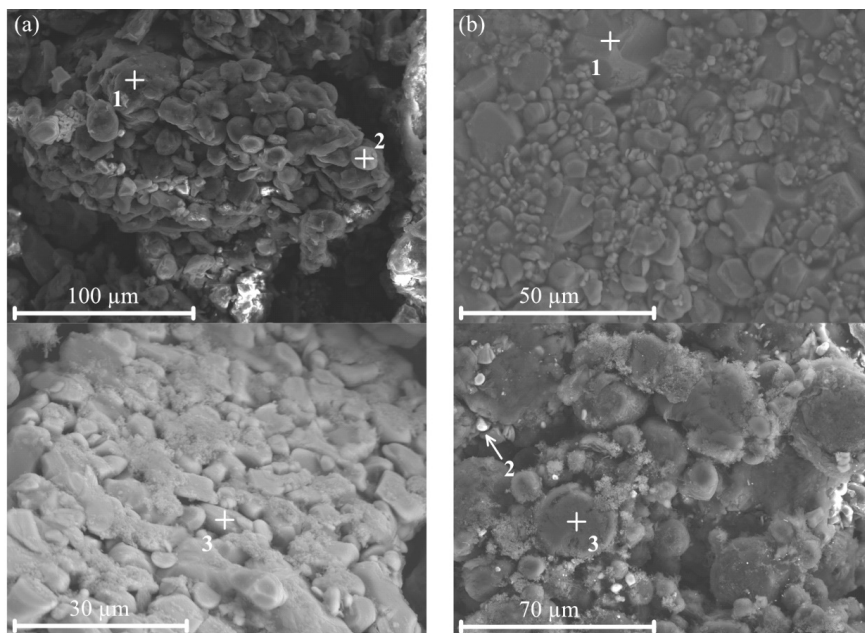
Fig. 4. SEM(SE)-EDS images of two fractions of the as-received LCO BM: (a) < 150 μm and (b) 150–700 μm (64).

The SEM images of the NMC BM in Fig. 5 show a large number of small spheres with the size of ~3–7 μm, which were made of smaller particles (a2 and a3). The EDS analysis showed that the material contained Co, Ni and Mn and thus originated from the cathode active material. EDS spectra from b1 and b4 also show the same composition. The EDS analysis demonstrated that the matrix is rich in C, e.g., a1, b2, and b3, that probably originated from the anode. F was another element detected with EDS in both LCO and NMC BM samples (Fig. 4 and Fig. 5), which was in line with the chemical analysis of BM. F was detected in some particles, but not all, originating both from the cathode and anode materials.
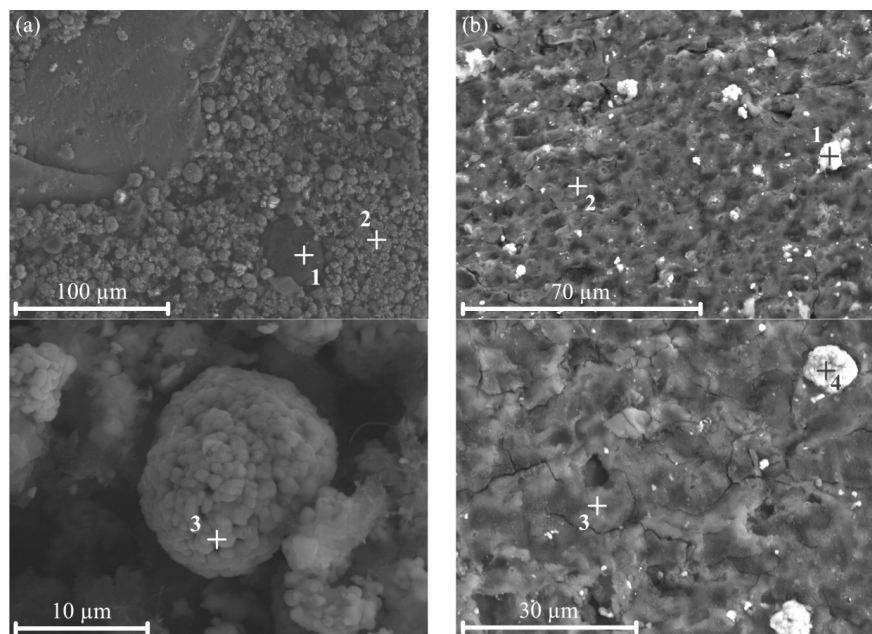
Fig. 5. SEM(SE)-EDS images of two fractions of the as-received NMC BM: (a) < 150 μm and (b) 150−700 μm (64).

4.2 High-temperature Behaviour of BM

4.2.1 BM from LCO LIBs

The high-temperature behaviour of LCO BM was studied by TGA, DTA, and QMS. The results are plotted in Fig. 6. In the fine fraction, mass loss begins at ~200−300 °C and is followed by the emission of hydrocarbons (C_xH_y) together with H_2O and CO_2 (in the QMS graph). The mass loss slope changes at ~600 °C, where an exothermic reaction takes place (DTA graph). No mass change is observed connected to that reaction, although sharp peaks of H_2O and CO_2 arise immediately thereafter. This emission synchronizes with a steeper slope in the weight curve which continues until ~900 °C. The endothermic peak at ~900 °C in the DTA graph is accompanied by a CO_2 peak.
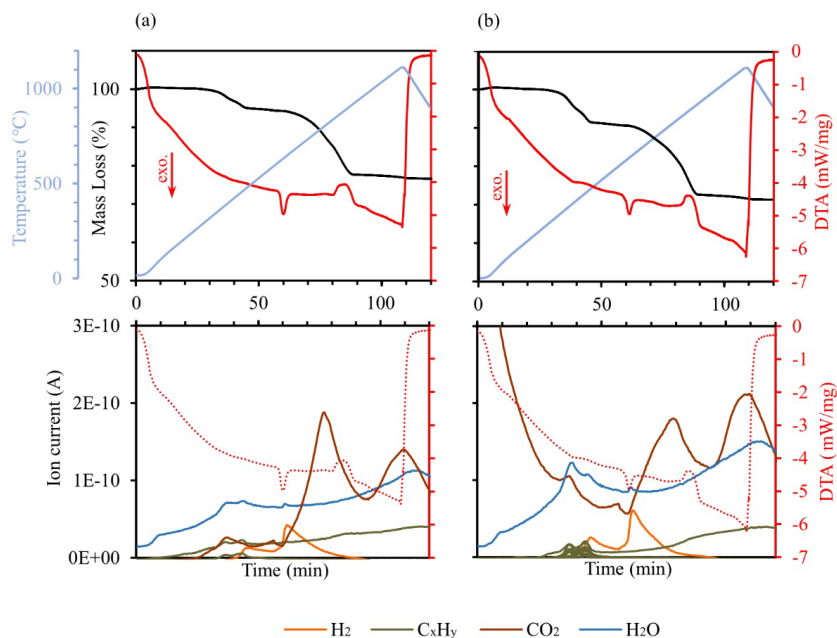
Fig. 6. TGA/DTA/QMS graphs of two fractions of the LCO BM: (a) < 150 μm and (b) 150–700 μm.

The XRD patterns from the as-received and reduced LCO BM are presented in Fig. 7. In Fig. 8, the high-temperature XRD patterns of LCO BM is shown. Fig. 7 demonstrates that the main phases in the LCO BM are LCO and graphite, and that the products of the reduction at 1100 °C are Co and graphite. Studying the phase transformations at elevated temperatures (Fig. 8) shows that at 550 °C, CoO peaks appear and LCO disappears at 700 °C, where $LiAlO_2$ and Co phases form. At 800 °C, all CoO peaks disappear. After cooling, the observed peaks in the XRD pattern are graphite, Co, SiO_2, and $LiAlO_2$.
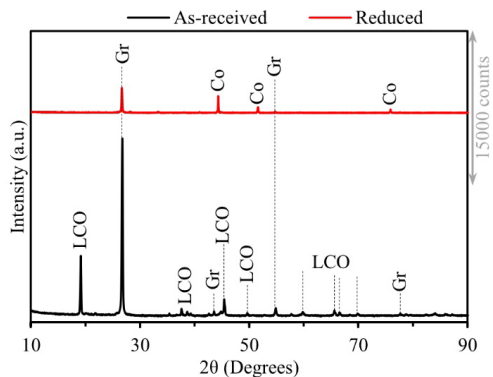
Fig. 7. XRD patterns of LCO BM before and after heat treatment at 1100 °C (64).
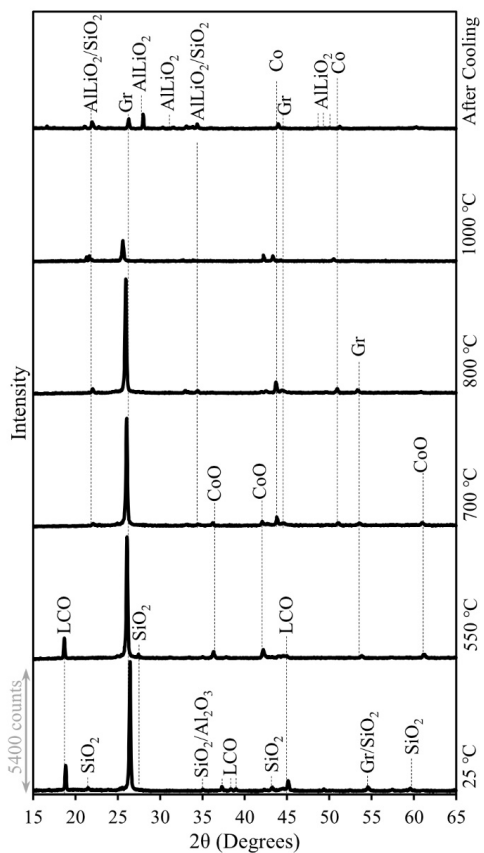
Fig. 8. XRD patterns during heating of the LCO BM to a temperature of 1000 °C (64).

The TGA curves from fine and coarse fractions in Fig. 6 show that the thermal behaviours of the two fractions are similar, hence, the following discussion is valid for both of them. By raising the

18

temperature and dissociation of organic materials in the BM (binders, like PVDF, and/or residual solvents), C_xH_y, CO_2, and H_2O emits from the sample. By ~600 °C, the transformation of LCO, in a reaction with graphite, gets complete and forms CoO (see Fig. 8), CO_2, and H_2O (QMS curves). The Li-containing compounds are not trackable in the XRD patterns, however, based on a study, it can be in form of Li_2CO_3 (65). In the regarded study, an exothermic reaction was proposed for this transformation (Eq. 3), which is an exothermic reaction that attributes no mass change, similar to what is observed in TGA curves.

$$2\ LiCoO_2 + C \rightarrow Li_2CO_3 + Co + CoO$$
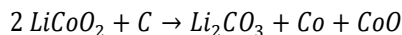
Eq. 3

To identify the influencing factors in the LCO transformation, some trials have been designed that were explained in the *Method* section (*LCO transformation*). The results of these experiments are presented in Fig. 9.[4] In these trials, LCO was first placed in Ar atmosphere and heated to 1100 °C. It did not decompose up to ~1100 °C. With the addition of graphite, the decomposition began at 630-670 °C, which is indicated by the associated exothermic reaction. The addition of Al and PVDF to this mix did not affect the transformation temperature. Based on these observations, it can be deduced that the transformation of LCO to its components is feasible in the presence of graphite. Plus, this transformation is required for the following mass loss in the BM.

---

[4] It should be mentioned that the temperature difference (~40 °C) of the exothermic reaction in the LCO+Gr+Al+PVDF sample is due to the smaller graphite particle size, which improves the kinetics of the reaction.
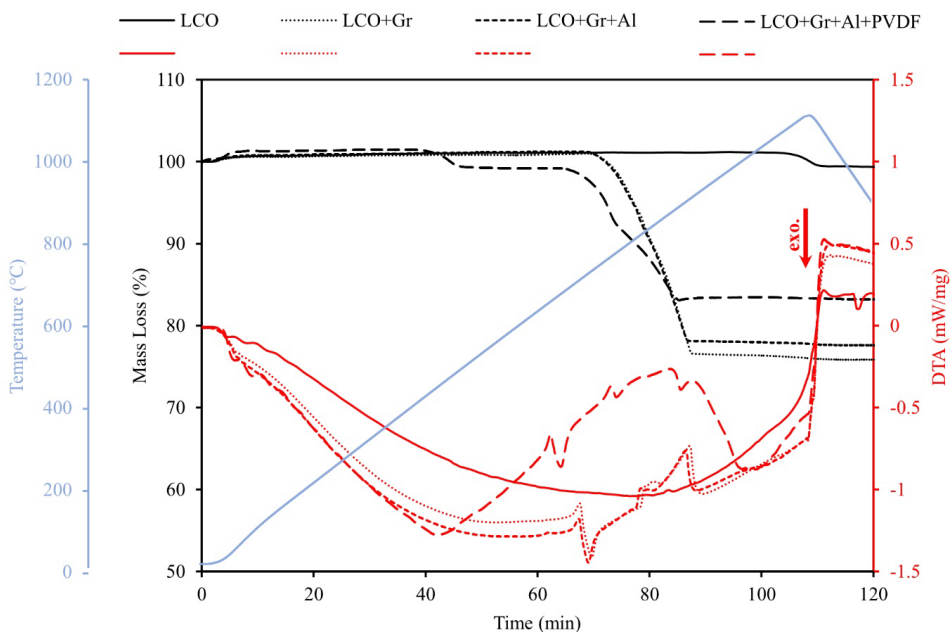
Fig. 9. TGA/DTA graphs of three different chemical grade LCO compositions heated to 1100 °C (64).

Getting back to the actual LCO BM, after LCO transformation, CoO reduction begins at a temperature of 700 °C and is accompanied by CO_2 emission. Considering the TGA/DTA and QMS graphs, the temperature of 800 °C can be attributed to the decomposition of Li_2CO_3 to Li_2O and CO_2. These statements are elaborated more in paper I.

Regarding the endothermic reaction at ~900 °C (Fig. 6), there are two possible explanations: gasification of C (Boudouard reaction) (66) or volatilization of Li_2O (67). According to the FactSage calculations, Li_2O percentage in the emitted gas should be very low and QMS data presented an emission of CO_2. Hence, the gasification of C seems to be a more probable explanation.

- Thermodynamic modeling

Fig. 10 shows the results from thermodynamic calculations by FactSage. After reduction at 1100 °C, the sample mainly consists of Co (in solid state), graphite, and gas. The least abundant phase is the slag phase[5], which mainly consists of Li_2O (not detected by XRD). $LiAlO_2$, LiF, and SiO_2 are also

---

[5] referred to liquid/glass solution in FactSage

thermodynamically probable at this temperature.

Fig. 10. LCO BM heat treated at 1100 °C, calculated by FactSage: Phase distribution and the slag calculated components (64).

The reduction of the cathode active material can be simplified to Eq. 4, assuming graphite is the only reductant in the BM. The ratio of CO to CO_2 was set based on the Boudouard reaction at a temperature of 600-900 °C. Based on this equation, the mass loss was ~23 wt.%, which is in agreement with the experimental mass loss deduced from the TGA curves.[6]

$$LiCoO_2 + 1.2\ C \rightarrow 0.5\ Li_2O + Co + 0.9\ CO + 0.3\ CO_2$$
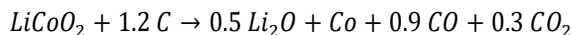
Eq. 4

4.2.2   BM from NMC LIBs

The TGA, DTA, and QMS results from the NMC BM are illustrated in Fig. 11. At ~300 °C, PVDF decomposes and C_xH_y gases form. By heating the BM, four exothermic reactions can be observed at ~300, ~400, ~600, and ~800 °C. The two latter reactions are followed by intense CO_2 and H_2O peaks in the QMS graphs.

---

[6] To compare the theoretical and experimental results, the mass loss ratio was calculated after reaching a temperature of 500 °C because the mass loss before that is related to PVDF decomposition, which is not included in the equation.
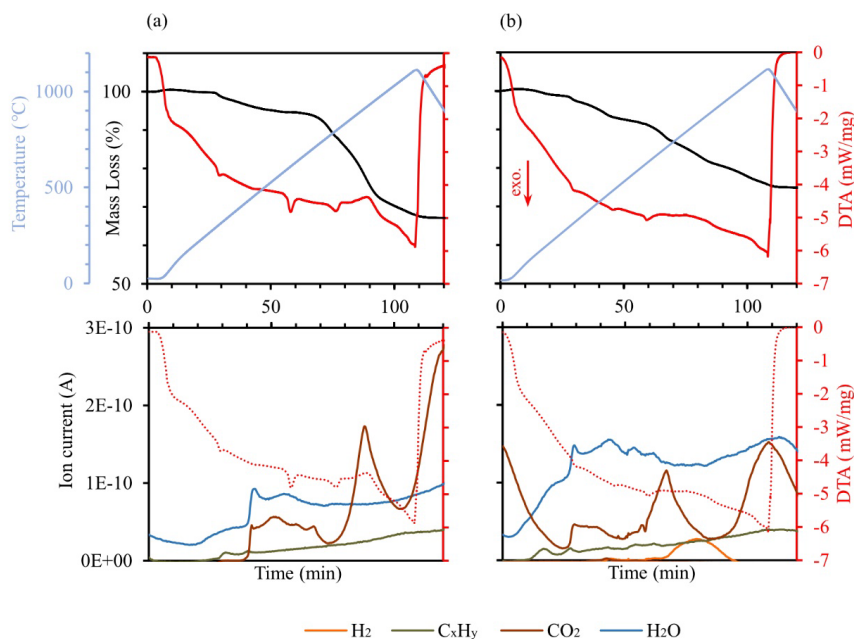
Fig. 11. TGA/DTA/QMS graphs of two fractions of the NMC BM: (a) < 150 μm and (b) 150−700 μm.

Fig. 12 illustrates the diffractograms of NMC BM, before and after reduction. The diffractograms show that the as-received BM consists of NMC and graphite and the reduced BM consists of LiF, graphite, metallic Co, and Ni. The high-temperature XRD patterns in Fig. 13 show SiO_2 beside cathode and anode active material. By increasing the temperature to 700 °C, the NMC peaks were replaced by the Co/Ni and MnO peaks, and the patterns remain almost constant up to 1000 °C. After cooling from 1000 °C to room temperature, the phases that appeared are SiO_2, Co/Ni, graphite, MnO, LiF, and Cu.
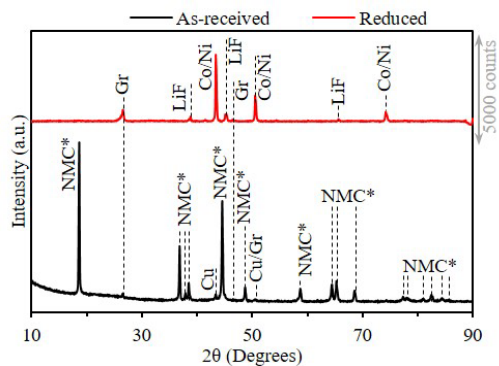
Fig. 12. XRD patterns of NMC BM before and after heat treatment at 1100 °C (64).
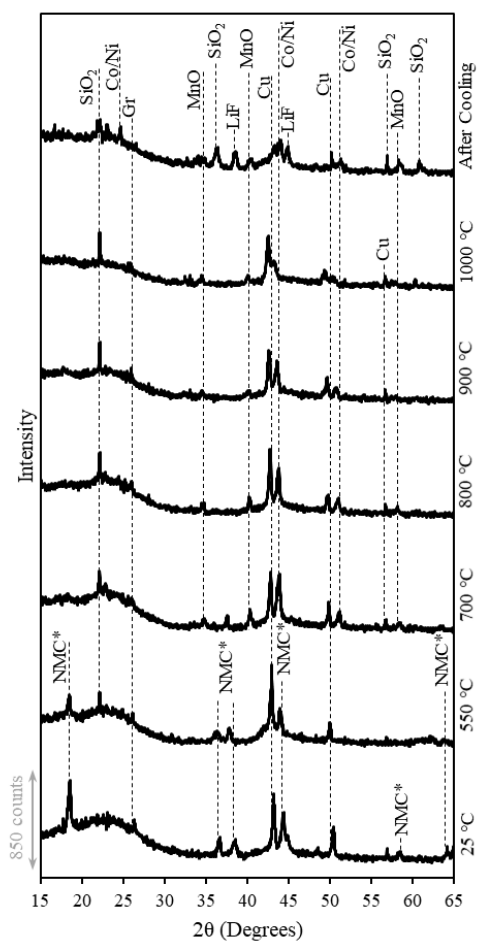
Fig. 13. XRD patterns during heating of the NMC BM to a temperature of 1000 °C (64).

It can be comprehended from the results presented in Table 3 that, unlike the LCO BM, fractionation has a significant effect on the composition in the NMC BM, and the C content is higher in the coarse fraction. This difference leads to different mass losses in the fine and coarse fractions (Fig. 11). The total mass loss amounts were ~33 and ~25 wt.% in the fine and coarse fractions, respectively. Similar to LCO BM, during the exothermic reaction at ~600 °C, NMC transforms to its components and results in emission of CO_2 and H_2O. After the transformation, the rate of the mass decrease is the highest. The reaction between 700 and 800 °C (a bump in the DTA curve) can be attributed to the decomposition of Li_2CO_3 into Li_2O and CO_2, similar to the discussion in the LCO BM section. After reduction, a Co/Ni phase forms, while part of the graphite remains unreacted. Moreover, the presence of LiF can be attributed to the higher content of F in the NMC BM (compared to LCO BM) (Table 3).

- Thermodynamic modeling

Fig. 14 presents the phases that formed according to FactSage after the reduction of NMC BM. The FactSage results are in agreement with the experimental results. Compared to LCO BM, it shows the formation of more F-containing compounds (LiF, MnF_2, and SiF_4) that is related to the higher F content in the NMC BM.
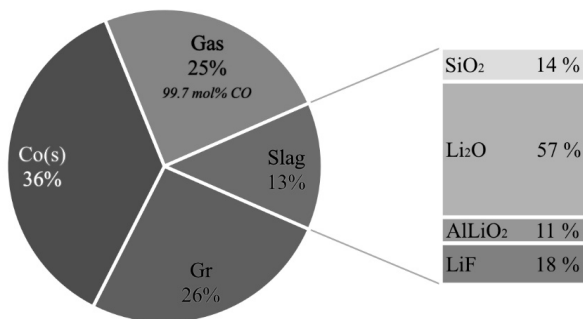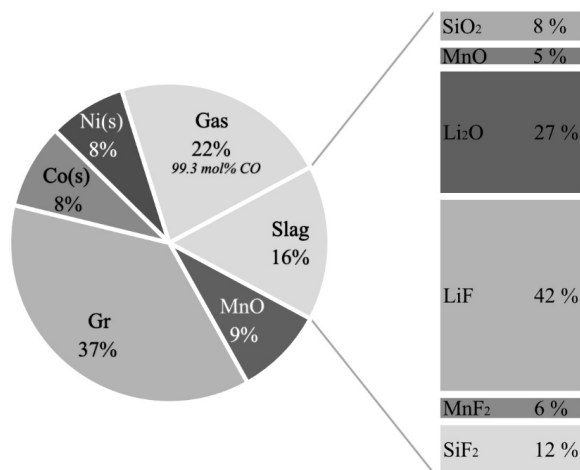

Fig. 14. NMC BM heat treated at 1100 °C, calculated by FactSage: Phase distribution and the slag calculated components (64).

By assuming C as the main reductant and a production of CO and CO_2 with the molar ratio of 3:1 (as explained before), the following reactions can be considered to calculate the mass loss during the

carbothermic reduction:[7]

$$LiNi_{0.33}Mn_{0.33}Co_{0.33}O_2 + 1.6\,C \rightarrow 0.33\,Ni + 0.33\,Mn + 0.33\,Co + Li + 1.2\,CO + 0.4\,CO_2$$

Eq. 5

$$LiNi_{0.33}Mn_{0.33}Co_{0.33}O_2 + 1.2\,C$$
$$\rightarrow 0.33\,Ni + 0.33\,Mn + 0.33\,Co + 0.5\,Li_2O + 0.9\,CO + 0.3\,CO_2$$

Eq. 6

$$LiNi_{0.33}Mn_{0.33}Co_{0.33}O_2 + 0.9\,C$$
$$\rightarrow 0.33\,Ni + 0.33\,MnO + 0.33\,Co + 0.5\,Li_2O + 0.7\,CO + 0.2\,CO_2$$
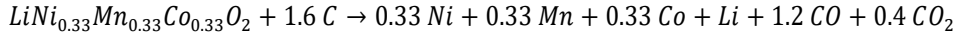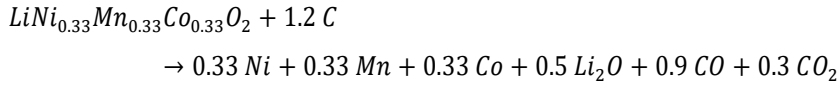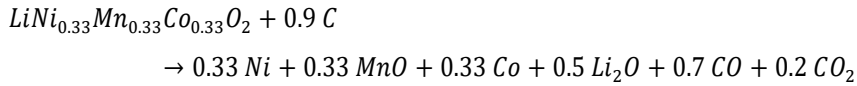
Eq. 7

The calculated mass losses in Eq. 5, Eq. 6, and Eq. 7 are 28.2, 21.1, and 15.6 wt.%, respectively. To compare them with the experimental mass losses, the experimental mass loss was calculated after 500 °C, the temperature at which PVDF decomposes completely. 20.4 wt.% and 29.5 wt.% of mass loss were observed for the coarse and fine fractions of NMC BM, respectively. From the comparison, it can be deduced that

- Ni and Co oxides are completely reduced to metallic form; and

- Part of the Li₂O and MnO lose O. It does not necessarily mean that they are reduced, since they can form Li and Mn fluorides and remain in the BM after heat treatment.

Regarding the fine fraction, the high mass loss can be attributed to the late devolatilization of organic materials (binders).

4.2.3 Effect of medium-temperature treatment on fluorine removal

Since the F content of NMC BM was higher than that of LCO BM, NMC BM was chosen for this section. The F content in four different stages is presented in Fig. 15. The primary NMC BM had only 2.91 wt.% F. By thermal treatment at 250–300 °C, the F content increased to 6.46 wt.%, and by increasing the temperature to 700 °C in Ar and air atmosphere, the F reached 7.19 wt.% and 12.30 wt.%, respectively.

---

[7] Since the total mass loss is the concern of this calculation, the formation of Mn/Li fluorides are considered as reduced Mn and Li in the equations.
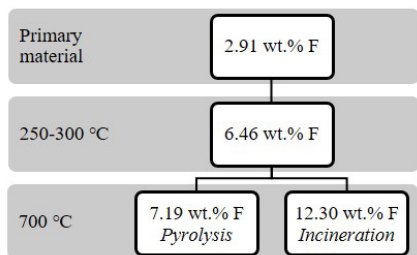
Fig. 15. F content after various heat treatment conditions (64).

It was stated in sections 4.2.14.2.2 and 4.2.2 that PVDF decomposes at temperatures lower than 500 °C and produces C_xH_y. Fig. 15 indicates that although PVDF decomposes, F does not evaporate even by heating up to 700 °C. After normalizing the F content at 700 °C (pyrolysis and incineration), the absolute F amounts that evaporated from 100 g of BM are approximately 0.63 and 0.56 g in Ar and air atmospheres, respectively. This implies that only 9.7 wt.% of the existing F is removed in the Ar atmosphere and 8.7 wt.% in the air atmosphere, and the rest will remain in the sample.

- Thermodynamic modeling

The FactSage results also concur that, after heating to 700 °C, F does not go into the gas phase. Table 4 shows the resemblance of experimental and modelled data. Based on FactSage, after pyrolysis, F forms LiF, and after incineration 70 wt.% of F is found in the form of LiF and the rest is in the form of $Li_2SiO_3(LiF)_2$.

Table 4. Calculated thermodynamic data regarding the F behaviour at 700 °C

Heat treatment/Atmosphere	F content (s) *Experimental*	F content (s) *Calculated*	F-containing phases *Calculated*
Pyrolysis/Ar	7.19	8.31	LiF
Incineration/Air	12.30	13.21	LiF, $Li_2SiO_3(LiF)_2$

4.3 Alloying

4.3.1 Fe-based alloys

As mentioned in section 3.2.3, Fe_2O_3 was added to the BM to reach a C:O molar ratio of 1:1. The new mixtures are presented in Table 5.

Table 5. Description of utilized Fe$_2$O$_3$-BM mixtures

Mixture	Fe$_2$O$_3$ (g) : BM (g)
MixFeLCO	55.0:45.0 Fe$_2$O$_3$:LCO
MixFeNMC	60.5:39.5 Fe$_2$O$_3$:NMC

The mass losses of MixFeLCO and MixFeNMC during heating, which are 44 wt.% and 43 wt.%, respectively, are plotted in Fig. 16. The mass loss begins at 150-200 °C and continues until 1450 °C for both BMs.
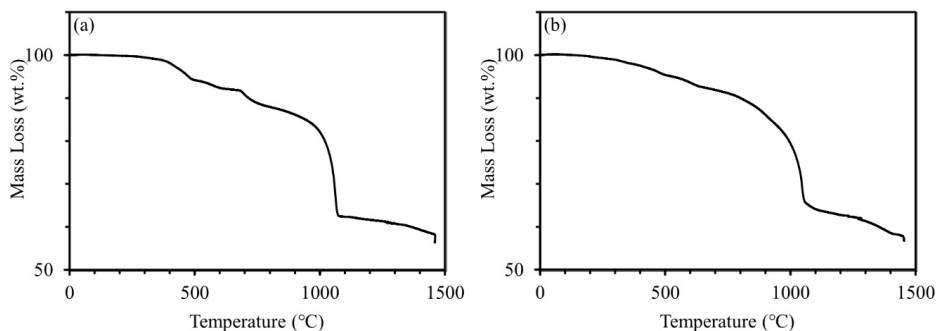
Fig. 16. Mass loss as a function of temperature during reduction of (a) MixFeLCO, and (b) MixFeNMC (62).

Reduction of Fe$_2$O$_3$ occurs in multiple steps by reducing to first Fe$_3$O$_4$, then FeO, and finally, Fe (68,69). If a reducing agent is available, it is possible to completely reduce Fe$_2$O$_3$ to metallic Fe at and below 1200 °C (68). Hence, the mass loss at higher temperatures can be attributed to:

- the late reduction of some oxides, which were not in contact with the reducing agent at lower temperature; or
- the reaction of irreducible oxides like Li$_2$O and MnO with F, which causes mass loss when CO is emitted (Eq. 8 and Eq. 9).

$$Li_2O + 2\,F + C \rightarrow 2\,LiF + CO$$

Eq. 8

$$MnO + 2\,F + C \rightarrow MnF_2 + CO$$
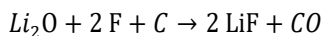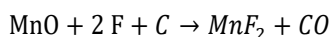
Eq. 9

The XRD patterns of the mixtures after heating at 1450 °C (Fig. 17) show the complete reduction of Fe, Co, and Ni oxides, with graphite remaining.
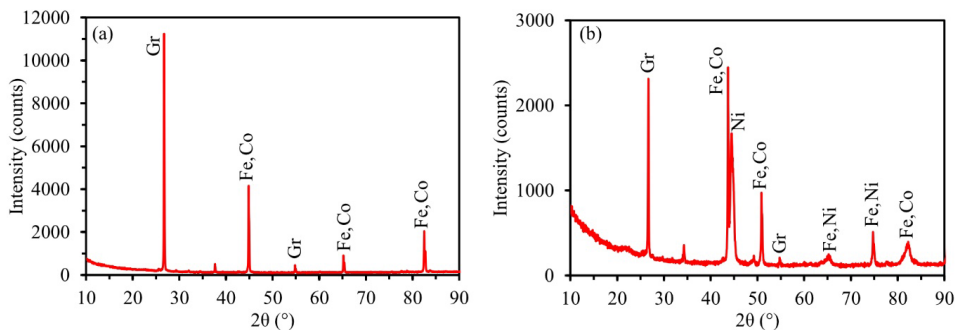
Fig. 17. XRD patterns of reduced (a) MixFeLCO, and (b) MixFeNMC (62).

C analysis of reduced mixtures also demonstrates that the reduced MixFeLCO and MixFeNMC have 3.2 wt.% and 3.5 wt.% C, respectively, meaning that 88.8 wt.% and 88.3 wt.% of the C in the BM was consumed when Fe_2O_3 was added.

- Thermodynamic modeling

Thermodynamic calculation for MixFeLCO and MixFeNMC (Fig. 18) demonstrates that at 1450 °C, a FeCo and FeCoNi alloy forms, respectively. In contrast to the experimental results, C is not found in the model. This can be explained by the fact that the modeling was done at 1450 °C and that the $CO:CO_2$ ratio at 1450 °C is different from the actual $CO:CO_2$ ratio in the experiment. During the experiment, reduction occurred gradually from lower temperatures, which result in lower $CO:CO_2$ ratios and consequently lower C consumption. Experimentally, when all the oxides present in the sample are consumed, part of the graphite will remain unreacted. According to FactSage, almost all Li remains in the slag phase (in form of oxide and fluoride) and Mn remains mainly in the oxide form, and the rest forms fluoride.
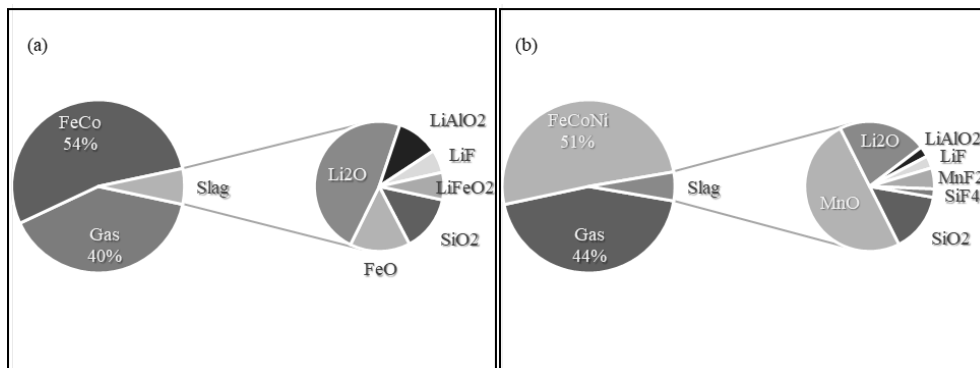
Fig. 18. (a) MixFeLCO, and (b) MixFeNMC reduced at 1450 °C, calculated by FactSage: Phase distribution and slag calculated components (62).

4.3.2 Cu-based alloys

Cu-based alloys were made applying the same strategy as explained for the Fe-based alloys. The CuO-BM mixtures are presented in Table 6.

Table 6. Description of utilized CuO-BM mixtures

Mixture	CuO (g) : BM (g)
MixCuLCO	59.5:40.5 CuO:LCO
MixCuNMC	67.0:33.0 CuO:NMC

The reduction of MixCuLCO and MixCuNMC is presented in Fig. 19, with a total mass loss of 33 wt.% and 30 wt.%, respectively, in the temperature range of 250-1450 °C. The beginning of the mass loss is related to the PVDF decomposition and reduction of CuO. Reduction of CuO to Cu in presence of C is thermodynamically feasible at room temperature (according to thermodynamic modeling), and it also has been seen by Kirakosyan et al. that CuO reduction begins at 440 °C (61,70). In general, since CuO reduction is thermodynamically possible, the kinetics factors like the heating rate, the particle size, and the contact between the reducing agent and the CuO will affect at what temperature reduction will become noticeable (~300 °C in the current study). The slope change in the mass loss curve at ~600 °C is related to the transformation and following reduction of the cathode active material. The continuation of the mass loss at higher temperatures can be the consequence of i) the late reduction of remaining oxides or ii) the reaction of the irreducible oxides with F, as explained in the *Fe-based alloys* section.
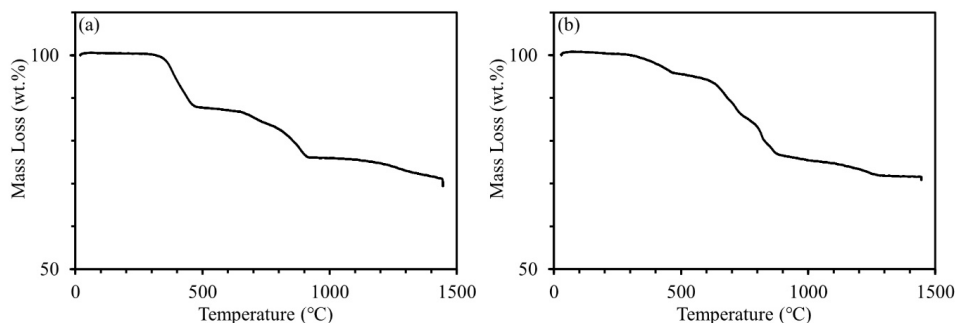
Fig. 19. Mass loss as a function of temperature during reduction of (a) MixCuLCO, and (b) MixCuNMC (62).

The XRD measurement (Fig. 20) revealed that metallic Cu, Co, and Ni (particularly in MixCuNMC) formed after reduction, and part of the graphite remained. The amount of graphite, that remained was determined and corresponded to 0.9 wt.% and 2.0 wt.% in reduced MixFeLCO and MixCuNMC, respectively. It means that 95.8 wt.% and 90.2 wt.% of the C in the BM was consumed to reduce the added CuO.
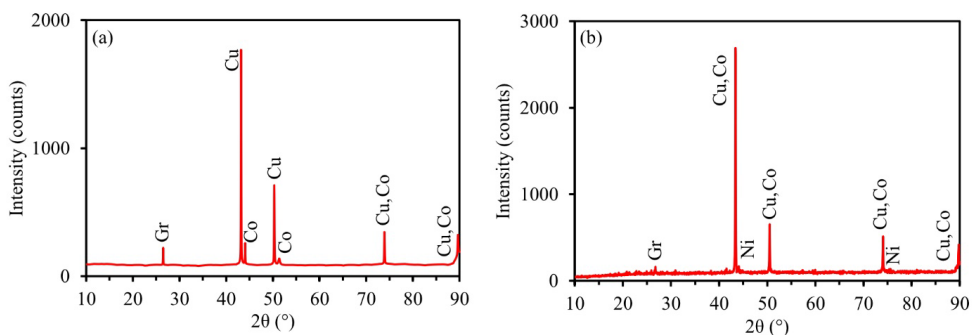
Fig. 20. XRD patterns of reduced (a) MixCuLCO, and (b) MixCuNMC (62).

- Thermodynamic modeling

FactSage calculations at 1450 °C (Fig. 21) show a complete reduction of MeOs in the mixture and consumption of graphite. The calculation also showed that Li was found in the form of Li_2O, $LiAlO_2$, and LiF.
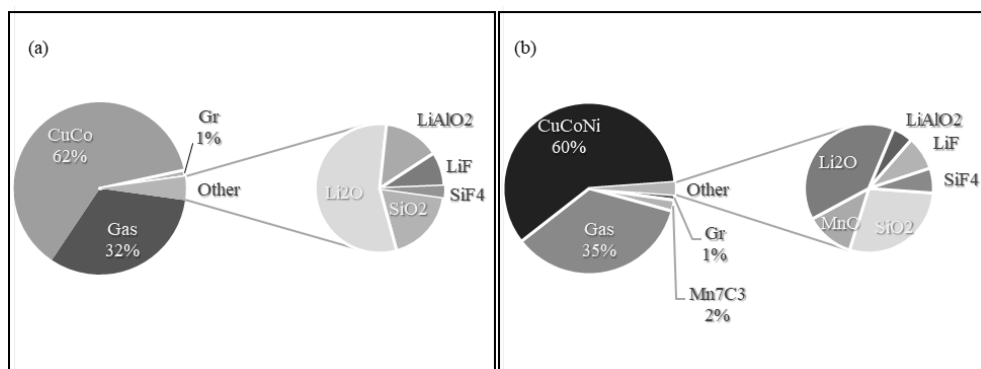
Fig. 21. (a) MixCuLCO, and (b) MixCuNMC reduced at 1450 °C, calculated by FactSage: Phase distribution and slag calculated components (62).

4.4 Effect of Mechanical Activation

4.4.1 Effect of mechanical activation on reduction of BM

Fig. 22 presents the PSD of the BM, before and after milling, from LCO and NMC BM, including d10, d50, and d90 values. The results show that 1 h of milling was the most effective and longer milling periods effect did not improve the particle size significantly.
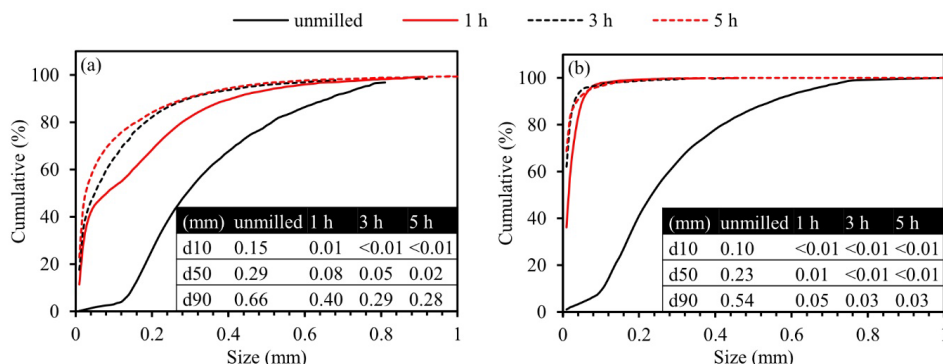
Fig. 22. Cumulative PSD of (a) LCO, and (b) NMC BM in four conditions (unmilled, milled for 1 h, milled for 3 h, and milled for 5 h) (62).

The effect of mechanical activation on the thermal reactivity of BM was further studied using TGA. The mass loss curves of BM after different milling periods are plotted in Fig. 23. Up to a temperature of ~600 °C, the curves overlap, while after this temperature, they do not follow the same rate, so different mass losses can be observed when increasing the temperature. By increasing the milling time, the reduction shift to a lower temperature range, although the effect of milling for 3 and 5 h is not as significant as milling for 1 h. 600 °C is the temperature where the cathode active

material transforms to simpler oxides, and the reduction of the metal oxides occurs at higher temperature. A higher rate of reduction in the milled BM shifts the reduction to lower temperatures.
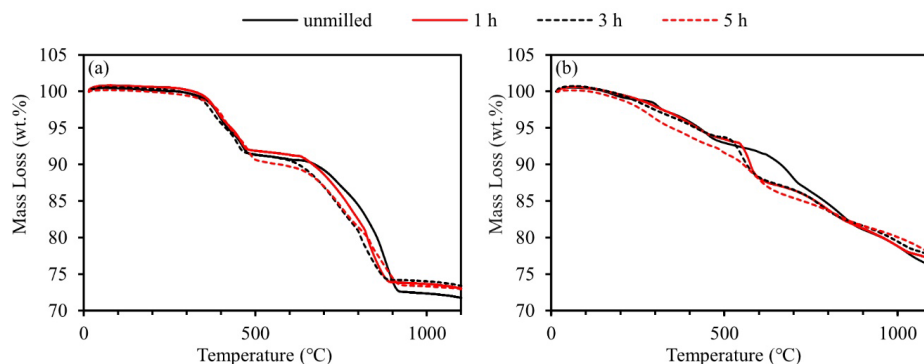
Fig. 23. Mass loss as a function of temperature during reduction of (a) LCO, and (b) NMC BM, before and after milling for 1, 3, and 5 h (62).

4.4.2 Effect of mechanical activation on alloying

In section 4.4.1, it was seen that milling for 1 h has the most significant effect. By comparing the effect of milling for 3 and 5 h on BM particle size and thermal reactivity, it was deduced that milling for 5 h in the LCO BM is not beneficial, and in the NMC BM, its effect is very insignificant hence further milling (5 h) is unnecessary, in particular from an energy point of view. Accordingly, 5 h milling was omitted for the Fe_2O_3-BM mixture. Instead, the condition with 3 h of milling was kept to see if it influences the thermal behaviour of Fe_2O_3-BM mixture or not.

- Fe-based alloys

The effect of milling on the thermal reactivity of MixFeLCO and MixFeNMC is illustrated in Fig. 24. Similar to the effect of mechanical activation on BM thermal reactivity, the significant effect on the reduction rate is observed on the material milled for 1 h, while longer milling times (3 h) does not have any significant effect on the reduction rate and thus, the effect of milling for 3 h compared to 1 h is negligible.
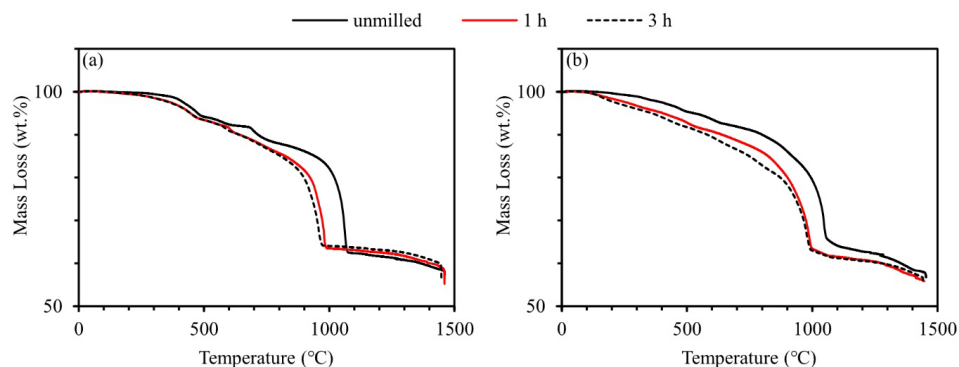
Fig. 24. Mass loss as a function of temperature during reduction of (a) MixFeLCO, and (b) MixFeNMC, before and after milling for 1 and 3 h (62).

The chemical composition of unmilled and milled mixtures after reduction is listed in Table 7. With milling, the C content of the reduced mixture is increased. It must be mentioned that the C content in samples that were milled for 1 and 3 h are almost equal.

Table 7. Chemical composition of unmilled and milled Fe_2O_3-BM mixtures after reduction at 1450 °C

Mixture	Milling time	Chemical composition						
		Fe	Co	Mn	Ni	C	Li	Other
MixFeLCO	unmilled	63.4	26.9	0.0	0.0	3.2	2.3	4.2
	1 h	62.7	26.3	0.0	0.0	6.0	1.5	3.4
	3 h	61.1	26.1	0.0	0.0	6.8	2.5	3.5
MixFeNMC	unmilled	68.9	8.2	6.5	7.5	3.5	2.5	2.9
	1 h	70.5	6.2	5.2	6.0	7.6	2.3	2.3
	3 h	69.5	6.4	5.4	6.1	7.7	2.9	2.0

The effect of mechanical activation on the reduction of these mixtures was observed from ~600 °C (cathode active material transformation) up to ~1100 °C (1147 °C reported as the temperature that is required for complete reduction of FeO to Fe (68)).

The remaining C in the mixtures after reduction reveals that C can be added by a C:O ratio of more than one. The increase in the remaining C by increasing milling time is related to Boudouard reaction. According to this reaction, by increasing the reduction temperature, the CO:CO₂ ratio increases, which results in higher consumption of C. Since mechanical activation decreases the temperature at which the reduction is occurring, less C is consumed in the reduction, and

accordingly, higher amount of C is left at the end of the reaction.

- Cu-based alloys

It was shown that mechanical activation for 3 h, compared to the 1 h, does not have an extra effect in the Fe-based alloys. Hence, the use of 3 h of milling was ignored in the Cu-based alloys.

The mass loss curves of MixCuLCO and MixCuNMC are depicted in Fig. 25. the effect of milling is mainly distinguishable from 300 °C to 900 °C.
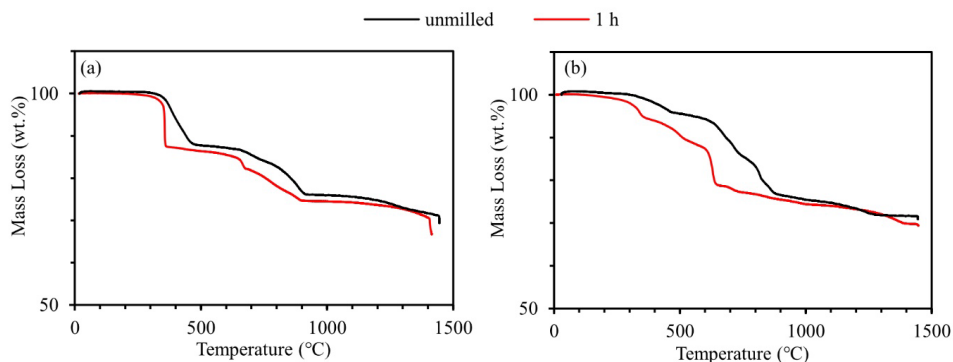
Fig. 25. Mass loss as a function of temperature during reduction of (a) MixCuLCO, and (b) MixCuNMC, before and after milling for 1 h (62).

The chemical composition of reduced mixtures (Table 8) shows that mechanical activation can save a significant amount of C.

Table 8. Chemical composition of unmilled and milled CuO-BM mixtures after reduction at 1450 ºC

Mixture	Milling time	Chemical composition						
		Cu	Co	Mn	Ni	C	Li	Other
MixCuLCO	unmilled	70.5	25.0	0.1	0.1	0.9	1.4	2.0
	1 h	70.5	17.0	0.0	0.0	8.9	1.9	1.8
MixCuNMC	unmilled	84.9	4.4	3.2	3.5	2.0	1.3	0.7
	1 h	76.4	3.7	3.2	3.4	10.5	1.6	0.9

In the CuO-BM mixtures, the effect of mechanical activation is observable before the transformation of cathode active material (~600 °C), at ~200-300 °C, when reduction of CuO begins. This effect continues up to ~1000 °C in MixCuLCO and ~800 °C in MixCuNMC. As simulated by FactSage, these mentioned temperatures are where Cu begins to melt. Since the role of mechanical activation is to affect the surface properties of solid particles, after the melting of the

main components in the system, this effect will disappear.

4.4.3 Thermodynamic investigation on the effect of mechanical activation

- Fe-based alloys

HSC chemistry was the tool that was employed in this part of the study for the mass and energy balance calculations. A summary of the input and output streams is listed in Table 9 and Table 10. These tables present the streams of the unmilled mixtures. The highlighted numbers show the numbers that were changing in modelling of different milling periods.

Table 9. Input/output streams in the mass and energy balance of MixFeLCO

Input streams @ 25 °C	Flow rate		Output streams @ 1450 °C	Flow rate	
LCO BM	45	kg/h	Li$_2$O	4.44	kg/h
64.6 wt.% LiCoO$_2$ 35.4 wt.% C			100 wt.% Li$_2$O		
Fe$_2$O$_3$	55	kg/h	FeCo	55.97	kg/h
100 wt.% Fe$_2$O$_3$			68.73 wt.% Fe(l) 31.27 wt.% Co(l)		
Ar	10	Nm³/h	Off-gas	36.35	Nm³/h
100 vol.% Ar			27.51 vol.% Ar(g) 52.57 vol.% CO(g) 19.92 vol.% CO$_2$(g)		
Heat flow	96.23	kw	Excess C	2	kg/h
Electricity flow	0	kw	100 wt.% C		

Table 10. Input/output streams in the mass and energy balance of MixFeNMC

Input streams @ 25 °C	Flow rate		Output streams @ 1450 °C	Flow rate	
NMC BM	39.5	kg/h	Li$_2$O, MnO	8.97	kg/h
56.8 wt.% LiNi$_{0.33}$Mn$_{0.33}$Co$_{0.33}$O$_2$ 43.2 wt.% C			38.96 wt.% Li$_2$O 61.04 wt.% MnO		
Fe$_2$O$_3$	60.5	kg/h	FeCoNi	51.40	kg/h
100 wt.% Fe$_2$O$_3$			82.33 wt.% Fe(l) 8.85 wt.% Co(l) 8.82 wt.% Ni(l)		
Ar	10	Nm³/h	Off-gas	38.13	Nm³/h
100 vol.% Ar			26.23 vol.% Ar(g) 63.53 vol.% CO(g) 10.24 vol.% CO$_2$(g)		
Heat flow	100.46	kw	Excess C	2.19	kg/h
Electricity flow	0	kw	100 wt.% C		

The energy input needed for different milling periods was calculated and presented in Fig. 26. The emission of CO and CO_2 was also considered in the calculations. The x-axis represents the final C content. It is indicated that increasing the milling time decreases the input energy requirement and increases the CO_2:CO ratio. The modeling results are similar to the experimental results (Fig. 16). By increasing the reduction rate, the reduction occurs in a lower temperature range, and consequently requires lower energy input.

Fig. 26. Energy consumption and CO/CO_2 production during reduction of (a) MixFeLCO, and (b) MixFeNMC at 1450 °C, calculated by HSC chemistry.

- Cu-based alloys

A summary of input and output streams in the copper system is presented in Table 11 and Table 12.

Table 11. Input/output streams in the mass and energy balance of MixCuLCO

Input streams @ 25 °C	Flow rate		Output streams @ 1450 °C	Flow rate	
LCO BM	40.5	kg/h	**Li$_2$O**	3.99	kg/h
64.6 wt.% LiCoO$_2$ 35.4 wt.% C			100 wt.% Li$_2$O		
CuO	59.5	kg/h	**CuCo**	63.29	kg/h
100 wt.% CuO			75.11 wt.% Cu(l) 24.89 wt.% Co(l)		
Ar	10	Nm³/h	**Off-gas**	35.95	Nm³/h
100 vol.% Ar			27.81 vol.% Ar(g) 71.80 vol.% CO(g) 0.39 vol.% CO$_2$(g)		
Heat flow	65.04	kw	**Excess C**	0.61	kg/h
Electricity flow	0	kw	100 wt.% C		

Table 12. Input/output streams in the mass and energy balance of MixCuNMC

Input streams @ 25 °C	Flow rate		Output streams @ 1450 °C	Flow rate	
NMC BM	33.5	kg/h	**Li$_2$O, MnO**	7.61	kg/h
56.8 wt.% LiNi$_{0.33}$Mn$_{0.33}$Co$_{0.33}$O$_2$ 43.2 wt.% C			38.96 wt.% Li$_2$O 61.04 wt.% MnO		
CuO	66.5	kg/h	**CuCoNi**	60.83	kg/h
100 wt.% CuO			87.34 wt.% Cu(l) 6.34 wt.% Co(l) 6.32 wt.% Ni(l)		
Ar	10	Nm³/h	**Off-gas**	34.25	Nm³/h
100 vol.% Ar			29.20 vol.% Ar(g) 70.78 vol.% CO(g) 0.03 vol.% CO$_2$(g)		
Heat flow	58.42	kw	**Excess C**	1.65	kg/h
Electricity flow	0	kw	100 wt.% C		

Fig. 27 demonstrates the results from mass and energy balance calculations. Similar to what was discussed in the previous section, milling of CuO–BM mixtures results in higher reaction rates, which makes the reduction occur in a lower temperature range thus requiring less energy input. This also results in a lower CO:CO$_2$ ratio that leads to a lower C consumption.
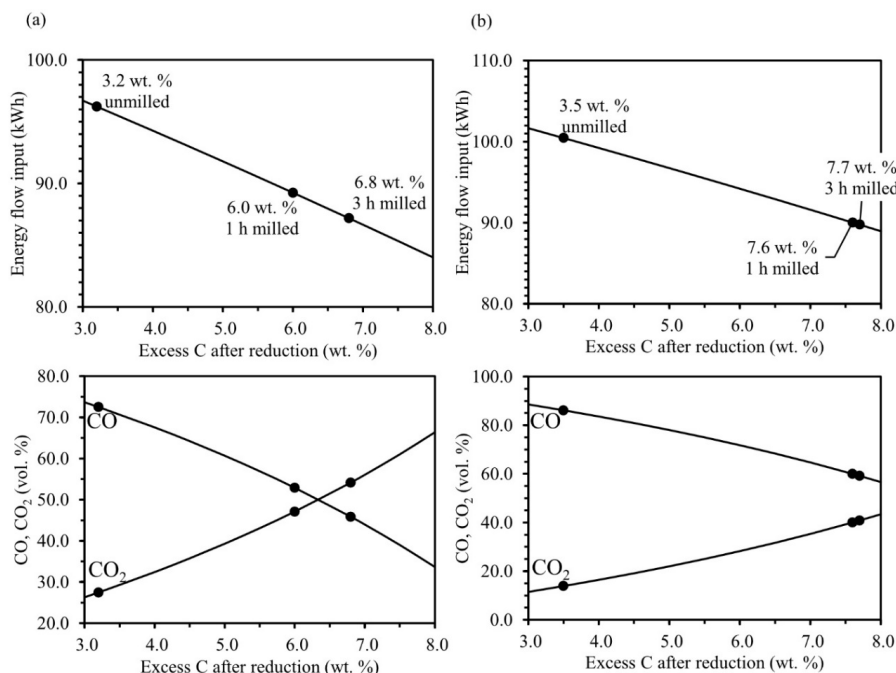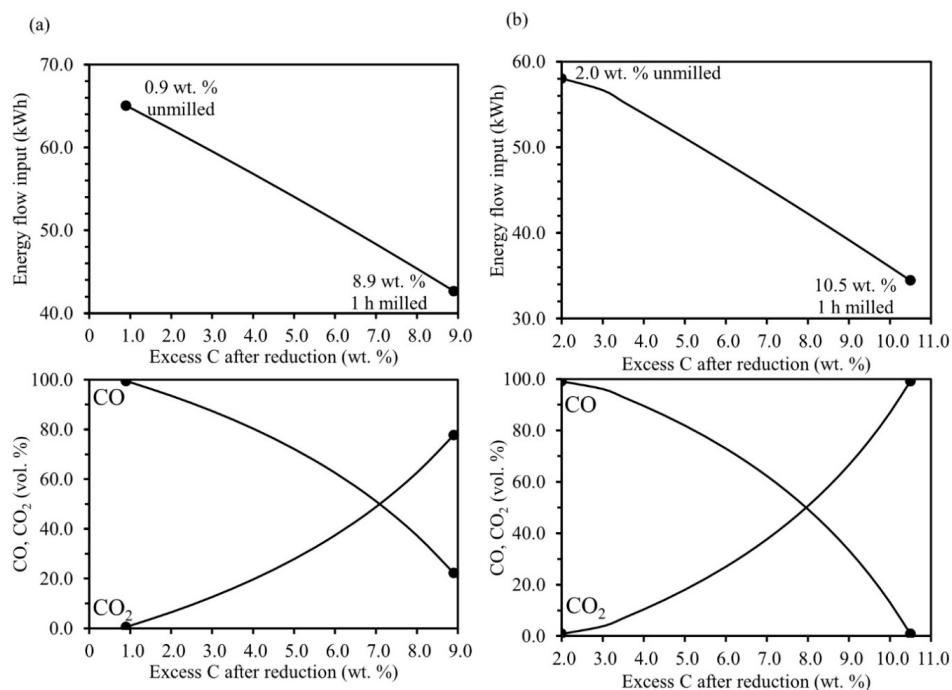
Fig. 27. Energy consumption and CO/CO₂ production during reduction of (a) MixCuLCO, and (b) MixCuNMC at 1450 °C, calculated by HSC chemistry.

In accordance with the Fe-based alloys, a similar effect on energy requirement connected to milling time and C content after reduction can be observed in the Cu-based alloys.

5 Conclusion

In this study, two types of Black Mass (BM) were thoroughly characterized, focusing on their high-temperature behaviour. Li and F were tracked during reduction and their behaviour was modelled thermodynamically. From the findings, one can deduce that i) a characterization routine was developed, including chemical, morphological, mineralogical, and thermal analyses; ii) the combination of ICP, ISE, and combustion methods seem to be appropriate to quantify the main elements in the BM: Co, Ni, Mn, Li, F, and C; iii) the mass loss in the temperature range of 200–500 °C was associated to the loss of hydrocarbons from BM and acetylene black, which was 5-10 wt.% of the BM. The transformation of cathode active material, in presence of C, to the constituting metal oxides occurred at ~600 °C and is associated with a heat release. The reduction of these oxides was enabled only after the transformation of cathode active material. After heating to 1100 °C, the majority of Li is found in some compounds, like $LiAlO_2$ and LiF; and iv) methods like pyrolysis and incineration do not help with the removal of F from BM.

Since it was shown that only part of the graphite was consumed during the reduction of cathode active material, Fe_2O_3 and CuO were added to benefit from the remaining C. It was shown that it is feasible to employ this method to produce Fe/Cu-based alloys containing Co (and Ni) as alloying elements.

To make this method more efficient, mechanical activation was further employed to improve the reduction kinetics, reduce the external metal oxides in a lower temperature range, and consequently consume less energy/carbon. Based on the results, it can be inferred that mechanical activation lowers the C consumption, and consequently decreases the CO_2 emission. It also lowers the energy required for producing an alloy and increases the Fe/Cu oxides that can be reduced.

6 References

1. Peters JF, Baumann M, Zimmermann B, Braun J, Weil M. The environmental impact of Li-Ion batteries and the role of key parameters – A review. Renew Sustain Energy Rev [Internet]. 2017;67:491–506. Available from http://dx.doi.org/10.1016/j.rser.2016.08.039

2. Nitta N, Wu F, Lee JT, Yushin G. Li-ion battery materials: present and future. Mater Today [Internet]. 2015 Jun;18(5):252–64. Available from: http://dx.doi.org/10.1016/j.mattod.2014.10.040

3. Dunn JB, Gaines L, Kelly JC, James C, Gallagher KG. The significance of Li-ion batteries in electric vehicle life-cycle energy and emissions and recycling's role in its reduction. Energy Environ Sci. 2015;8:158–68.

4. Liang Y, Zhao C, Yuan H, Chen Y, Zhang W, Huang J, et al. A review of rechargeable batteries for portable electronic devices. InfoMat. 2019;1(1):6–32.

5. Boddula R, Pothu R, Asiri AM. Rechargeable Batteries: History, Progress, and Applications [Internet]. Wiley; 2020. Available from: https://books.google.se/books?id=O1TdDwAAQBAJ

6. An L, editor. Recycling of Spent Lithium-Ion Batteries [Internet]. Cham: Springer International Publishing; 2019. Available from: http://link.springer.com/10.1007/978-3-030-31834-5

7. Melin E. State-of-the-art in reuse and recycling of lithium-ion batteries – A research review [Internet]. Circular Energy Storage. 2019 [cited 2021 Aug 4]. Available from: http://www.energimyndigheten.se/globalassets/forskning--innovation/overgripande/state-of-the-art-in-reuse-and-recycling-of-lithium-ion-batteries-2019.pdf

8. European Commission. Proposal for a REGULATION OF THE EUROPEAN PARLIAMENT AND OF THE COUNCIL concerning batteries and waste batteries, repealing Directive 2006/66/EC and amending Regulation (EU) No 2019/1020 [Internet]. Vol. COM(2020). 2020 [cited 2021 Aug 26]. Available from: https://eur-lex.europa.eu/legal-content/EN/TXT/?uri=CELEX%3A52020PC0798

9. Berckmans G, Messagie M, Smekens J, Omar N, Vanhaverbeke L. Cost Projection of State of the Art Lithium-Ion Batteries for Electric Vehicles Up to 2030. Energies [Internet]. 2017 Sep 1;10(9):1314. Available from: https://www.mdpi.com/1996-1073/10/9/1314

10. Zheng X, Zhu Z, Lin X, Zhang Y, He Y, Cao H, et al. A Mini-Review on Metal Recycling from Spent Lithium Ion Batteries. Engineering. 2018;4(3):361–70.

11. Zeng X, Li J, Singh N. Recycling of Spent Lithium-Ion Battery: A Critical Review. Crit Rev Environ Sci Technol [Internet]. 2014 May 19;44(10):1129–65. Available from: http://www.tandfonline.com/doi/abs/10.1080/10643389.2013.763578

12. Yoshino A. 1 - Development of the Lithium-Ion Battery and Recent Technological Trends. In: Pistoia GBT-L-IB, editor. Amsterdam: Elsevier; 2014. p. 1–20. Available from: https://www.sciencedirect.com/science/article/pii/B9780444595133000017

13. Foreman E, Zakri W, Hossein Sanatimoghaddam M, Modjtahedi A, Pathak S, Kashkooli AG, et al. A Review of Inactive Materials and Components of Flexible Lithium-Ion Batteries. Adv Sustain Syst. 2017;1(11):1700061.

14. Zhu P, Gastol D, Marshall J, Sommerville R, Goodship V, Kendrick E. A review of current collectors for lithium-ion batteries. J Power Sources [Internet]. 2021;485(November 2020):229321. Available from: https://doi.org/10.1016/j.jpowsour.2020.229321

15. Jiang Q, Du K, He Y. A novel method for preparation of LiNi1/3Mn1/3Co1/3O2 cathode material for Li-ion batteries. Electrochim Acta [Internet]. 2013 Sep;107:133–8. Available from: https://linkinghub.elsevier.com/retrieve/pii/S0013468613011080

16. Lombardo G, Ebin B, Foreman MR, Steenari BM, Petranikova M. Incineration of EV Lithium-ion batteries as a pretreatment for recycling − Determination of the potential formation of hazardous by-products and effects on metal compounds. J Hazard Mater [Internet]. 2020;393(January):122372. Available from: https://doi.org/10.1016/j.jhazmat.2020.122372

17. Ross BJ, LeResche M, Liu D, Durham JL, Dahl EU, Lipson AL. Mitigating the Impact of Thermal Binder Removal for Direct Li-Ion Battery Recycling. ACS Sustain Chem Eng [Internet]. 2020 Aug 24;8(33):12511–5. Available from: https://pubs.acs.org/doi/10.1021/acssuschemeng.0c03424

18. Kim S, Bang J, Yoo J, Shin Y, Bae J, Jeong J, et al. A Comprehensive Review on the Pretreatment Process in Lithium-ion Battery Recycling. J Clean Prod [Internet]. 2021;294:126329. Available from: https://doi.org/10.1016/j.jclepro.2021.126329

19. Zhang G, He Y, Feng Y, Wang H, Zhu X. Pyrolysis-Ultrasonic-Assisted Flotation Technology for Recovering Graphite and LiCoO 2 from Spent Lithium-Ion Batteries. ACS Sustain Chem Eng [Internet]. 2018 Aug 6;6(8):10896–904. Available from: https://pubs.acs.org/doi/10.1021/acssuschemeng.8b02186

20. Ruismäki R, Rinne T, Dańczak A, Taskinen P, Serna-Guerrero R, Jokilaakso A. Integrating Flotation and Pyrometallurgy for Recovering Graphite and Valuable Metals from Battery Scrap. Metals (Basel) [Internet]. 2020 May 21;10(5):680. Available from: https://www.mdpi.com/2075-4701/10/5/680

21. Velázquez-Martínez O, Valio J, Santasalo-Aarnio A, Reuter M, Serna-Guerrero R. A Critical Review of Lithium-Ion Battery Recycling Processes from a Circular Economy Perspective. Batteries [Internet]. 2019 Nov 5;5(4):68. Available from: https://www.mdpi.com/2313-0105/5/4/68

22. Harper G, Sommerville R, Kendrick E, Driscoll L, Slater P, Stolkin R, et al. Recycling lithium-ion batteries from electric vehicles. Nature [Internet]. 2019 Nov 6;575(7781):75–86. Available from: http://dx.doi.org/10.1038/s41586-019-1682-5

23. Chen X, Kang D, Li J, Zhou T, Ma H. Gradient and facile extraction of valuable metals from spent lithium ion batteries for new cathode materials re-fabrication. J Hazard Mater [Internet]. 2020;389(December 2019):121887. Available from: https://doi.org/10.1016/j.jhazmat.2019.121887

24. Yang Y, Lei S, Song S, Sun W, Wang L. Stepwise recycling of valuable metals from Ni-rich cathode material of spent lithium-ion batteries. Waste Manag [Internet]. 2020;102:131–8. Available from: https://doi.org/10.1016/j.wasman.2019.09.044

25. Chen W, Ho H-J. Recovery of Valuable Metals from Lithium-Ion Batteries NMC Cathode Waste Materials by Hydrometallurgical Methods. Metals (Basel) [Internet]. 2018 May 6;8(5):321. Available from: http://www.mdpi.com/2075-4701/8/5/321

26. Zhou W. Hydrometallurgical Treatment of Spent Lithium-Ion Batteries : A study of optimal conditions for the leaching. Chalmers University of Technology; 2017.

27. Zheng R, Zhao L, Wang W, Liu Y, Ma Q, Mu D, et al. Optimized Li and Fe recovery from spent lithium-ion batteries via a solution-precipitation method. RSC Adv [Internet]. 2016;6(49):43613–25. Available from: http://xlink.rsc.org/?DOI=C6RA05477C

28. Lupi C, Dell'Era A, Pasquali M. Ni-Co Alloy Production from Secondary Spent Batteries by Electrowinning. Curr Phys Chem. 2015;4(4):324–9.

29. Shuva MAH, Kurny A. Hydrometallurgical Recovery of Value Metals from Spent Lithium Ion Batteries. Am J Mater Eng Technol [Internet]. 2013;1(1):8–12. Available from: http://pubs.sciepub.com/materials/1/1/2/index.html

30. Shu-guang Z, Wen-zhi HE, Guang-ming LI, Xu Z, Xiao-jun Z, Ju-wen H, et al. Recovery of Co and Li from spent lithium-ion batteries by combination method of acid leaching and chemical precipitation. Trans Nonferrous Met Soc China [Internet]. 2012;22(9):2274–81. Available from: https://www.sciencedirect.com/science/article/pii/S100363261161460X

31. Li L, Lu J, Ren Y, Zhang XX, Chen RJ, Wu F, et al. Ascorbic-acid-assisted recovery of cobalt and lithium from spent Li-ion batteries. J Power Sources [Internet]. 2012;218:21–7. Available from: http://dx.doi.org/10.1016/j.jpowsour.2012.06.068

32. Makuza B, Tian Q, Guo X, Chattopadhyay K, Yu D. Pyrometallurgical options for recycling spent lithium-ion batteries: A comprehensive review. J Power Sources [Internet]. 2021;491(November 2020):229622. Available from: https://doi.org/10.1016/j.jpowsour.2021.229622

33. Windisch-Kern S, Gerold E, Nigl T, Jandric A, Altendorfer M, Rutrecht B, et al. Recycling chains for lithium-ion batteries: A critical examination of current challenges, opportunities and process dependencies. Vol. 138, Waste Management. Elsevier Ltd; 2022. p. 125–39.

34. Xiao J, Li J, Xu Z. Challenges to Future Development of Spent Lithium Ion Batteries Recovery from Environmental and Technological Perspectives. Environ Sci Technol. 2020;54:9–25.

35. Li J, Wang G, Xu Z. Environmentally-friendly oxygen-free roasting/wet magnetic separation technology for in situ recycling cobalt, lithium carbonate and graphite from spent LiCoO2/graphite lithium batteries. J Hazard Mater [Internet]. 2016;302:97–104. Available from: http://dx.doi.org/10.1016/j.jhazmat.2015.09.050

36. Jian Y, Zongliang Z, Gang Z, Liangxing J, Fangyang L, Ming J, et al. Process study of chloride roasting and water leaching for the extraction of valuable metals from spent

lithium-ion batteries. Hydrometallurgy [Internet]. 2021;203(February):105638. Available from: https://doi.org/10.1016/j.hydromet.2021.105638

37. Liu C, Lin J, Cao H, Zhang Y, Sun Z. Recycling of spent lithium-ion batteries in view of lithium recovery: A critical review. J Clean Prod [Internet]. 2019;228(1):801–13. Available from: https://doi.org/10.1016/j.jclepro.2019.04.304

38. Hu X, Mousa E, Tian Y, Ye G. Recovery of Co, Ni, Mn, and Li from Li-ion batteries by smelting reduction - Part I: A laboratory-scale study. J Power Sources [Internet]. 2021;483(September):228936. Available from: https://doi.org/10.1016/j.jpowsour.2020.228936

39. Hu X, Mousa E, Ye G. Recovery of Co, Ni, Mn, and Li from Li-ion batteries by smelting reduction – Part II: A pilot-scale demonstration. J Power Sources [Internet]. 2021;483(November 2020):229089. Available from: https://doi.org/10.1016/j.jpowsour.2020.229089

40. Guoxing R, Songwen X, Meiqiu X, Bing P, Youqi F, Fenggang W, et al. Recovery of Valuable Metals from Spent Lithium-Ion Batteries by Smelting Reduction Process Based on MnO-SiO2-Al2O3 Slag System. In: Advances in Molten Slags, Fluxes, and Salts: Proceedings of the 10th International Conference on Molten Slags, Fluxes and Salts 2016 [Internet]. Cham: Springer International Publishing; 2016. p. 211–8. Available from: http://link.springer.com/10.1007/978-3-319-48769-4_22

41. Sommerfeld M, Vonderstein C, Dertmann C, Klimko J, Oráč D, Miškufová A, et al. A combined pyro-and hydrometallurgical approach to recycle pyrolyzed lithium-ion battery black mass part 1: Production of lithium concentrates in an electric arc furnace. Metals (Basel). 2020;10(8):1–27.

42. Xiao S, Ren G, Xie M, Pan B, Fan Y, Wang F, et al. Recovery of Valuable Metals from Spent Lithium-Ion Batteries by Smelting Reduction Process Based on MnO–SiO2–Al2O3 Slag System. J Sustain Metall. 2017;3:703–10.

43. Or T, Gourley SWD, Kaliyappan K, Yu A, Chen Z. Recycling of mixed cathode lithium-ion batteries for electric vehicles: Current status and future outlook. Carbon Energy. 2020;2(1):6–43.

44. Klimko J, Oráč D, Miškufová A, Vonderstein C, Dertmann C, Sommerfeld M, et al. A

Combined Pyro- and Hydrometallurgical Approach to Recycle Pyrolyzed Lithium-Ion Battery Black Mass Part 2: Lithium Recovery from Li Enriched Slag—Thermodynamic Study, Kinetic Study, and Dry Digestion. Metals (Basel) [Internet]. 2020 Nov 23;10(11):1558. Available from: https://www.mdpi.com/2075-4701/10/11/1558

45. Meshram P, Pandey BD, Mankhand TR. Hydrometallurgy Extraction of lithium from primary and secondary sources by pre-treatment , leaching and separation : A comprehensive review. Hydrometallurgy [Internet]. 2014;150:192–208. Available from: http://dx.doi.org/10.1016/j.hydromet.2014.10.012

46. Kwon OS, Sohn I. Fundamental thermokinetic study of a sustainable lithium-ion battery pyrometallurgical recycling process. Resour Conserv Recycl [Internet]. 2020;158(October 2019):104809. Available from: https://doi.org/10.1016/j.resconrec.2020.104809

47. Li J, Lai Y, Zhu X, Liao Q, Xia A, Huang Y, et al. Pyrolysis kinetics and reaction mechanism of the electrode materials during the spent LiCoO2 batteries recovery process. J Hazard Mater [Internet]. 2020;398(May):122955. Available from: https://doi.org/10.1016/j.jhazmat.2020.122955

48. Wang W, Zhang Y, Zhang L, Xu S. Cleaner recycling of cathode material by in-situ thermite reduction. J Clean Prod [Internet]. 2020 Mar;249:119340. Available from: https://doi.org/10.1016/j.jclepro.2019.119340

49. Liu W, Zhong X, Han J, Qin W, Liu T, Zhao C, et al. Kinetic Study and Pyrolysis Behaviors of Spent LiFePO4 Batteries. ACS Sustain Chem Eng. 2019;7(1):1289–99.

50. Wang M, Tan Q, Liu L, Li J. A Facile, Environmentally Friendly, and Low-Temperature Approach for Decomposition of Polyvinylidene Fluoride from the Cathode Electrode of Spent Lithium-ion Batteries. ACS Sustain Chem Eng [Internet]. 2019 Aug 5;7(15):12799–806. Available from: https://pubs.acs.org/doi/10.1021/acssuschemeng.9b01546

51. Mossali E, Picone N, Gentilini L, Rodrìguez O, Pérez JM, Colledani M. Lithium-ion batteries towards circular economy: A literature review of opportunities and issues of recycling treatments. J Environ Manage [Internet]. 2020 Jun;264:110500. Available from: https://linkinghub.elsevier.com/retrieve/pii/S0301479720304345

52. Hu H, Chen Q, Yin Z, Zhang P, Zou J, Che H. Study on the kinetics of thermal decomposition of mechanically activated pyrites. Thermochim Acta. 2002;389(1–2):79–83.

53. Hu H, Chen Q, Yin Z, Zhang P, Ye L. The thermal behavior of mechanically activated galena by thermogravimetry analysis. Metall Mater Trans A Phys Metall Mater Sci. 2003;34(13):793–7.

54. Kosmac T, Courtney TH. Milling and mechanical alloying of inorganic nonmetallics. J Mater Res [Internet]. 1992;7(6):1519–25. Available from: https://doi.org/10.1557/JMR.1992.1519

55. Pourghahramani P, Forssberg E. Reduction kinetics of mechanically activated hematite concentrate with hydrogen gas using nonisothermal methods. Thermochim Acta. 2007;454(2):69–77.

56. Pourghahramani P, Forssberg E. Effects of mechanical activation on the reduction behavior of hematite concentrate. Int J Miner Process. 2007;82(2):96–105.

57. Zdujić M, Jovalekić Č, Karanović L, Mitrić M, Poleti D, Skala D. Mechanochemical treatment of α-Fe2O3 powder in air atmosphere. Mater Sci Eng A. 1998;245(1):109–17.

58. Welham NJ. Activation of the carbothermic reduction of manganese ore. Int J Miner Process. 2002;67(1–4):187–98.

59. Hu H, Chen Q, Yin Z, Zhang P. Thermal behaviors of mechanically activated pyrites by thermogravimetry (TG). Thermochim Acta. 2003;398(1–2):233–40.

60. Guzmán D, Fernández J, Ordoñez S, Aguilar C, Rojas PA, Serafini D. Effect of mechanical activation on the barite carbothermic reduction. Int J Miner Process [Internet]. 2012 Jan;102–103:124–9. Available from: https://linkinghub.elsevier.com/retrieve/pii/S0301751611001748

61. Bale CW, Bélisle E, Chartrand P, Decterov SA, Eriksson G, Gheribi AE, et al. FactSage Thermochemical Software and Databases - 2010 - 2016 [Internet]. Vol. 54, Calphad. 2016. p. 35–53. Available from: www.factsage.com

62. Babanejad S, Ahmed H, Andersson C, Heikkinen E-P. Mechanical Activation-Assisted Recovery of Valuable Metals from Black Mass in the Form of Fe/Cu Alloys. J Sustain Metall [Internet]. 2023 Mar 6; Available from: https://link.springer.com/10.1007/s40831-023-00665-6

63. Brückner L, Frank J, Elwert T. Industrial Recycling of Lithium-Ion Batteries—A Critical

Review of Metallurgical Process Routes. Metals (Basel) [Internet]. 2020 Aug 18;10(8):1107. Available from: https://www.mdpi.com/2075-4701/10/8/1107

64. Babanejad S, Ahmed H, Andersson C, Samuelsson C, Lennartsson A, Hall B, et al. High-Temperature Behavior of Spent Li-Ion Battery Black Mass in Inert Atmosphere. J Sustain Metall [Internet]. 2022 Mar 28;8(1):566–81. Available from: https://doi.org/10.1007/s40831-022-00514-y

65. Kuzuhara S, Ota M, Tsugita F, Kasuya R. Recovering lithium from the cathode active material in lithium-ion batteries via thermal decomposition. Metals (Basel). 2020;10(4):1–13.

66. Vishvakarma S, Dhawan N. Recovery of Cobalt and Lithium Values from Discarded Li-Ion Batteries. J Sustain Metall [Internet]. 2019 Jun 23;5(2):204–9. Available from: http://link.springer.com/10.1007/s40831-018-00208-4

67. Wang W, Zhang Y, Liu X, Xu S. A Simplified Process for Recovery of Li and Co from Spent LiCoO2 Cathode Using Al Foil As the in Situ Reductant. ACS Sustain Chem Eng [Internet]. 2019 Jun 26;7:acssuschemeng.9b01564. Available from: https://pubs.acs.org/doi/10.1021/acssuschemeng.9b01564

68. Jung SM, Yi SH. A kinetic study on carbothermic reduction of hematite with graphite employing thermogravimetry and quadruple mass spectrometry. Steel Res Int. 2013;84(9):908–16.

69. Szendrei T, Van Berge PC. Thermogravimetry and evolved gas analysis of the reduction of hematite (Fe2O3) with graphite. Thermochim Acta [Internet]. 1981;44(1):11–9. Available from: https://linkinghub.elsevier.com/retrieve/pii/0040603181802663

70. Kirakosyan H, Minasyan T, Niazyan O, Aydinyan S, Kharatyan S. DTA/TG study of CuO and MoO3 co-reduction by combined Mg/C reducers. J Therm Anal Calorim. 2016;123(1):35–41.

Paper I

RESEARCH ARTICLE

High-Temperature Behavior of Spent Li-Ion Battery Black Mass in Inert Atmosphere

Safoura Babanejad[1] · Hesham Ahmed[1,2] · Charlotte Andersson[1] · Caisa Samuelsson[1] · Andreas Lennartsson[1] · Björn Hall[3] · Linn Arnerlöf[4]

Abstract

The increased demand for Li-ion batteries has prompted the scientific community to improve recycling routes in order to reuse the valuable materials in batteries. After their end-of-life, the batteries are collected, discharged, and mechanically disintegrated, generating plastic and metallic streams that are recycled directly; this leaves behind a small particle size fraction known as black mass (BM). BM is composed mainly of graphite and Li-metal complex oxides. Pyrometallurgy is a route known for recycling of BM, in which identifying the BM's behavior at high temperatures is essential. In this study, two types of BM are characterized in two fractions of 150–700 μm and smaller than 150 μm. The thermal behavior of the BM is studied with thermal analysis techniques. The analyses demonstrate that the mineralogical and morphological properties of the two fractions do not significantly differ, while the amounts of C and organic materials might vary. When the BM was thermally treated, the binders decomposed until a temperature of 500 ℃ was reached, where the volatilization of hydrocarbons was observed, although F mostly persisted in the BM. The Li-metal oxide was partially reduced to lower oxides and Li carbonate at ~ 600 ℃, and the main mass loss was caused by carbothermic reduction immediately thereafter. As the products of this process, metallic Co and Ni phases were formed, and part of the graphite remained unreacted. Regarding the Li behavior, it was observed that in the presence of Al, $AlLiO_2$ is the most likely composition to form, and it changes to LiF by increasing the F concentration in the composition.

Graphical Abstract

Introduction

Since the beginning of the 1990s, Li-ion batteries (LIBs) have been regarded as the most promising energy storage solution for various applications due to their high energy density, low memory effect, low self-discharge, and long lifespan. Due to the increasing demand in fossil-free energy, a large amount of LIBs is produced today. It is predicted that the number of electric vehicles will increase from 4 million in 2018 to 900 million in 2048 [1–4]. By 2025, it is expected that ∼ 850,000 tons of LIBs will need to be recycled globally. In the regulatory proposal concerning batteries and waste batteries published by the European Commission, special attention should be given to recycling of end-of-life (EOL) batteries and closing the material loops. The regulation states that the recycling efficiency of LIBs should exceed 65% by 2025 [5]. The use of eco-friendly

and resource-efficient methods for handling LIB components after EOL relieves environmental contamination pressure, generates remarkable economic and social benefits, and reduces the dependency on primary materials [6, 7].

After their EOL, LIBs are mechanically collected, discharged, and disintegrated. This generates plastic and metallic streams, which can be recycled directly by physical separation, leaving behind a small particle size fraction, known as black mass (BM) [8, 9]. The BM contains anode materials (mainly graphite), cathode materials (e.g., $LiMeO_2$), binders (usually polyvinylidene fluoride (PVDF)), conductive additives (acetylene black), traces of electrolyte (typically Li salt dissolved in an organic solvent), and electrode current collector residuals (Cu and Al) [1, 10, 11].

The process for recycling of BM typically starts with a pretreatment process, to liberate the battery components, and enhance the efficiency of target elements recovery.

According to the literature, thermal pretreatment at 500–600 ℃ can be used to evaporate organic materials in BM (e.g., electrolyte, separator, and PVDF residuals) that contain F, which is known as a hazardous and corrosive element [10, 12–14]. Chemical and thermal procedures can be employed separately to remove binders and facilitate BM particle separation. Flotation, which is a physical pretreatment method, is used to separate the graphite particles in the BM based on their wettability properties [10, 15]. Pyro- and hydrometallurgical processes, as the main methods for extracting metals, usually follow the pretreatment step. In pyrometallurgy, valuable metals are recovered at high temperatures based on their physical and chemical properties [4], while in hydrometallurgy, the process of metal recovery is performed based on aqueous chemistry at low temperatures, in which a combination of different techniques, e.g., leaching, solvent extraction, and precipitation, are performed [16–20]. These two major methods have pros and cons, such as the emission of hazardous gas in pyrometallurgy and the production of wastewater in hydrometallurgy processes. The higher efficiency of the hydrometallurgical routes makes them more popular for the recycling of LIBs. This effect stands out in particular in the recovery of Li, of which most is lost in the slag in almost all commercial pyrometallurgical processes, such as Umicore and Inmetco. However, in hydrometallurgical recycling processes, LIB pretreatment, such as passivation, is often a prerequisite to facilitate processes like leaching [9]. The main advantage of the pyrometallurgical methods is their industrial simplicity, e.g., the technology is currently ready, and there is no obligation to apply passivation steps [9–11, 17]. The use of pyrometallurgical methods, under efficient conditions, would be an easier option for the recycling of LIBs. To develop such a method, the initial stage is to determine the high-temperature properties and behavior of the material—in this case, BM. There are various battery types that generates different BM compositions. In this regard, some studies have been performed to investigate the effect of high-temperature treatment on different battery compositions both on the cathode/anode active material, a mix of them, or unaltered BM.

In 2019, Wang et al. roasted the *cathodes of LCO batteries* (cathode material: $LiCoO_2$—anode material: graphite) that consisted of Al foil, PVDF, acetylene black, and $LiCoO_2$. Roasting was performed under an Ar atmosphere, where the formation of Li_2O, $AlLiO_2$, and CoO plus incomplete degradation of PVDF was observed after reaching a temperature of 600 ℃. This study revealed that Al acts as the primary reductant of $LiCoO_2$ to CoO [21]. Lombardo et al. showed that pyrolysis of BM from *NMC batteries* (cathode material: $LiNi_xMn_yCo_zO_2$—anode material: graphite) at 600 and 700 ℃ completely decomposed the cathode active material via a carbothermic reaction to its constituents, including Co, Ni, and Mn_3O_4, and Al remained unreacted. In analyzing

the released gas from the samples, no F-containing compounds were detected [22]. Incineration of these batteries was also investigated by these authors, where F was detected in the gaseous products and byproducts after thermal treatment [23]. Kwon and Sohn studied the thermokinetics of *$LiCoO_2$ and graphite* up to 1500 ℃ in an Ar atmosphere and reported a temperature range of 880–1200 ℃ as the optimal temperature for the recovery of Li and Co. They stated that part of $LiCoO_2$ is reduced to Co_3O_4 at 500 ℃ and that the total transformation to CoO and Li_2CO_3 occurs at 607–689 ℃. Li_2CO_3 decomposes to Li_2O and CO_2 at 689–882 ℃, and Co forms as the product of CoO reduction at 882–1128 ℃. The mass loss at higher temperatures was assigned to the Boudouard reaction toward producing CO in this study [24]. The literature mentions that heating the *LFP cathode material* ($LiFePO_4$) at 450–650 ℃ would remove PVDF (up to 96.85 wt%), in which the F content decreases from 8.51 wt% (before pyrolysis) to 1.67% (collected oil after pyrolysis). In this study, the decrease in F content was attributed to the evaporation of HF [13].

To develop a sustainable pyrometallurgical method that enables efficient BM recycling, a thorough understanding of its behavior at high temperatures is needed. In terms of cathode material decomposition, there are some contradictory comprehensions of the reactions that occur, and the following work aims to clarify these reactions. Moreover, an element of importance at high temperature is F and its behavior, which is poorly understood. Special attention is devoted to this aspect in the current work, mainly by tracking F in the solid-state. In this study, two types of BM obtained from commercial spent LIBs via mechanical separation routes were characterized with focus on their thermal behavior.

Experimental

Materials

The BM from the following two types of LIBs were considered in this study: LCO batteries from portable mobile phones and NMC batteries from car batteries ($LiNi_{0.33}Mn_{0.33}Co_{0.33}O_2$ as the cathode active material in this study). The as-received BM samples were produced, mechanically separated, and heat treated at 250–300 ℃ (to remove the electrolyte) by Stena Recycling International AB, Sweden. The samples were in two particle size ranges: particles smaller than 150 μm and particles between 150 and 700 μm.

To more deeply investigate the $LiCoO_2$ transformation, $LiCoO_2$ (99.8%, Aldrich) together with graphite (− 300 mesh, 99%, Alfa Aesar, and APS 7–11 micron, 99%, Alfa Aesar), Al (+ 325 mesh, 99.5%, Alfa Aesar), and PVDF (HSV 900, Arkema) were used to investigate the effect of

some elements, i.e., C, Al, and F, in the BM on the decomposition of $LiCoO_2$.

Characterization

A variety of methods were employed to chemically, mineralogically, and morphologically characterize BM at both room and high temperatures. For chemical analysis, inductively coupled plasma–mass spectrometry (ICP–MS) was used to analyze most of the elements. The procedure was performed according to SS EN ISO 17294–2:2016 and EPA method 200.8:1994. In addition, measurement of the C content was conducted by combustion analysis using a LECO CS230. The ion selective electrode (ISE) method was utilized to analyze the amount of F in the samples, applying EPA method 9214. To employ this method in analyzing the solid samples, 0.5 g of the sample was mixed with ~ 2 g Na_2O_2 in a Ni crucible and covered with ~ 1 g Na_2O_2. The mixture was subsequently melted at 800 ℃ for 8 min and after cooling in room temperature for 10 min, 20 mL of deionized water was added to entirely dissolve the solid sample. The solution was thereafter adjusted to 1000 mL with the addition of deionized water. 20 mL of the new solution was transferred to another beaker and the pH of the solution was regulated to neutral with acetic acid using phenolphthalein as an indicator, and then 20 mL of TISAB buffer solution was added. The titration was performed using a Metrohm 888 Titrando.

Mineralogical characterization was performed by particle size distribution (PSD) (Retsch Camsizer XT) and X-ray diffraction (XRD). A PANalytical Empyrean X-ray diffractometer in θ-θ geometry with Cu-Kα radiation ($\lambda = 0.154184$ nm), a beam current of 40 mA, and a beam voltage of 45 kV was used for the measurement. The XRD pattern was measured in the 2θ range of 20°–90° with a step size of 0.026°/s. A curved graphite crystal monochromator mounted in front of a PIXcel 3D detector was used to remove the fluorescence due to the presence of Fe in the samples. The measured data were evaluated for phase identification using HighScore Plus (v4.7, PANalytical B.V., Almelo, The Netherlands) software, and FIZ-NIST Inorganic Crystal Structure Database (ICSD) and Crystallography Open Database (COD) databases. The morphology of the as-received BM samples was investigated under a Zeiss Merlin field emission gun scanning electron microscope (SEM) equipped with an Oxford Instruments X-Max energy dispersive X-ray spectroscopy (EDS) detector with AZtec software.

Thermal Analysis

To detect the high-temperature behavior of BM in a reductive atmosphere, a Netzsch STA 409 instrument with a detection limit of 1 μg was utilized to conduct thermogravimetric/differential thermal analysis (TGA/DTA) under an Ar atmosphere (flow rate of 100 mL/min) and with a heating rate of 10 ℃/min. The gases that evolved during the experiments were continuously monitored using a quadrupole mass spectrometer (QMS) for qualitative analysis.

Additionally, the phases that developed upon heating were identified by the same XRD instrument used for the mineralogical characterization, which was equipped with an Anton Paar HTK 1200 N high-temperature chamber that was used to heat the sample to 1000 ℃ at a heating rate of 10 ℃/min and He flow rate of 10 mL/min. To analyze the sample at the desired temperature, the sample was held at the set temperature for 1 min before acquiring the XRD pattern, which was measured in the 2θ range of 15°–65° with a step size of 0.083°/s.

$LiCoO_2$ Reduction

The transformation of LCO BM to its components was simulated by the synthetic materials as listed in Table 1. The proportions were set based on the LCO BM composition. The heating trial, which was applied to the LCO BM, was repeated in these experiments to perform TGA/DTA. For the last experiment with LCO + Gr + Al + PVDF, the graphite that was used had the particle size of 7–11 μm.

F Behavior

To monitor whether F evaporates during heating in the pretreatment step, the BM was analyzed by the ISE method on the following occasions: (i) before heating at 250–300 ℃ (see "Materials" section); (ii) the as-received BM; (iii) BM after pyrolysis at 700 ℃ in an Ar atmosphere for 1 h; and (iv) BM after incineration at 700 ℃ (in a synthetic air atmosphere) for 1 h.

Table 1 Chemical composition used in the complementary experiments

Sample	(g)				(wt%)			
	$LiCoO_2$	Graphite	Al	PVDF	$LiCoO_2$	Graphite	Al	PVDF
LCO	55.9	–	–	–	100.0	–	–	–
LCO + Gr	55.9	35.4	–	–	61.2	38.8	–	–
LCO + Gr + Al	55.9	35.4	0.9	–	60.6	38.4	1.0	–
LCO + Gr + Al + PVDF	55.9	35.4	0.9	4.42	57.9	36.6	0.9	4.6

Thermodynamic Modeling

To identify the reaction mechanisms and evaluate/support the experimental results, a set of calculations using the *Equilib* module in the thermodynamic software FactSage 8.0 were conducted [25]. The *FactPS* and *FToxid* databases were used in the present calculations. When using FactSage, the low-concentration elements were omitted. The *FToxid-SLAGA*, *FToxid-SPINA*, *FToxid-MeO_A*, *FToxid-NAShB*, and *FToxid-NASlB* solution phases were selected together with the *ideal gas* phase and *pure solids* species. To simulate the synthetic air atmosphere, the O_2 activity was set to 0.2.

Results and Discussion

Chemical Analysis

The chemical compositions of both BM types in the coarse and fine fractions are listed in Table 2. The data reveal that for the LCO BM, the composition of the fine and coarse fractions is approximately the same. In addition to Li, Co, and C, some traces of Al, Cu, P, and F are detected. In contrast, a difference in the compositions of the two fractions is observed for the NMC BM. The main difference is the amount of C, which is much higher in the coarse fraction, while there is a lower amount of the other main elements—e.g., Li, Co, and Ni. The amounts of the other elements are approximately the same in both fractions.

The Li-to-Co ratio in the LCO case (both fractions) is the same as the Li-to-Co ratio in $LiCoO_2$, the cathode material in the LCO batteries. In the NMC BM, the ratio between the Li, Co, Ni, and Mn amounts is equivalent to the $LiNi_{0.33}Mn_{0.33}Co_{0.33}O_2$ phase. The high amount of C in the compositions of both types of BM is attributed to the graphite in the anode. In the NMC case, the C content is much higher in the coarse fraction, leading to a lower proportion of cathode material (Li, Co, Ni, and Mn). In other words, for NMC, C accumulates in the coarse fraction, while the $LiNi_{0.33}Mn_{0.33}Co_{0.33}O_2$ ratio in the fine fraction is higher. The Al and Cu traces likely originate from current collector residuals in the BM. Si and P are from the additive materials

in the anode, and F is the corrosive element that exists mainly in PVDF, but there are also some other F sources, such as electrolyte and anode additives [17, 26].

Mineralogical and Morphological Investigation

The PSD results of the LCO BM show d10, d50, and d90 values of 0.02, 0.06, and 0.14 mm in the fine fraction and 0.15, 0.31, and 0.71 mm in the coarse fraction, respectively. In the NMC BM, the results were < 0.01, 0.04, and 0.13 mm for d10, d50, and d90 in the fine fraction, and 0.15, 0.34, and 0.71 mm in the coarse fraction, respectively. The analysis indicates that in each fraction, the d10, d50, and d90 values are almost equal in the LCO and NMC BM. The main difference might stem from the d10 of the fine fractions, which has a much smaller particle size in the NMC BM.

XRD measurements were conducted on the two fractions of LCO and NMC BM provided. The XRD data obtained from the LCO BM (Fig. 1a) reveal that the active cathode material is mainly $LiCoO_2$ and that the anode material primarily consists of graphite (shown as Gr in the figures). $LiNi_{0.33}Mn_{0.33}Co_{0.33}O_2$ (denoted by NMC* in the figures) is the primary active cathode material detected in the NMC BM (Fig. 1b). The XRD results from the different fractions (coarse and fine) are similar in terms of the phase types, while they exhibit a slight difference in the intensity of detected peaks in the BM fractions.

As shown in Fig. 2, the SEM images from the as-received LCO BM show irregular and sheet-like particles in a wide size range. The SEM images also show that larger particles are actually agglomerates of smaller particles. The agglomeration could be caused by the residual binder or could be connected to the material's physical properties (size and surface). EDS analyses show that the sheet-like particles mainly consisted of C (a1 and b3 spectra), while the other types of particles were rich in Co (a2, a3, b1, and b2). Li was not detectable by EDS but based on XRD data it can be assumed that the particles rich in Co could represent the $LiCoO_2$ phase.

The SEM images of the BM samples from NMC batteries (Fig. 3) show a large number of small spheres in the range of ~ 3–7 μm. Higher magnification revealed that each sphere

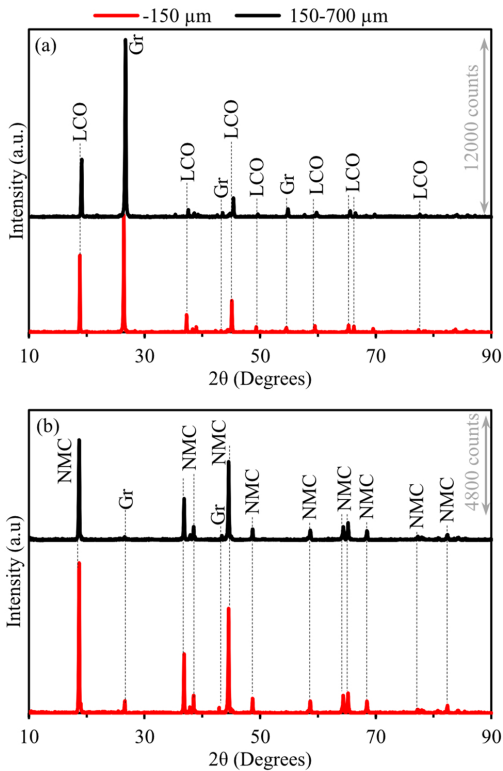| Table 2 Chemical compositions of LCO and NMC BM in two fractions of < 150 and 150–700 μm (wt%)	Sample (wt%)	Li	Co	Ni	Mn	Al	Cu	Si	P	F	C
	LCO < 150 μm	3.8	31.4	0.0	0.0	0.4	0.4	1.6	0.4	2.1	43.8
	LCO 150–700 μm	4.0	32.3	0.0	0.0	0.9	0.6	1.6	0.5	2.6	35.4
	NMC < 150 μm	6.3	17.3	15.5	15.1	0.0	0.8	1.3	0.4	4.9	12.8
	NMC 150–700 μm	3.6	8.0	7.3	7.6	0.2	1.6	1.0	0.6	6.5	43.2

Fig. 1 XRD pattern of **a** LCO and **b** NMC BM

were comprised of much smaller particles (a2 and a3). This assembly possibly originated from the cathode materials as these particles are rich in cathode material elements, i.e., Co, Ni, and Mn. A similar cathode composition is also observed in b1 and b4 in the NMC coarse fraction (see Fig. 3). Irregularly shaped particles were found in all samples with a wide range of sizes from a few microns up to a 100 μm or slightly more. The small particles were aggregated into irregular agglomerates with a size range of several hundred microns. According to the EDS results, the matrix is rich in C, e.g., a1, b2, and b3. In addition, F was detected with EDS both in LCO and NMC (Fig. 2 and Fig. 3) supporting the results from the chemical analysis showing the presence of F-containing compounds (e.g., PVDF) in the as-received BM.
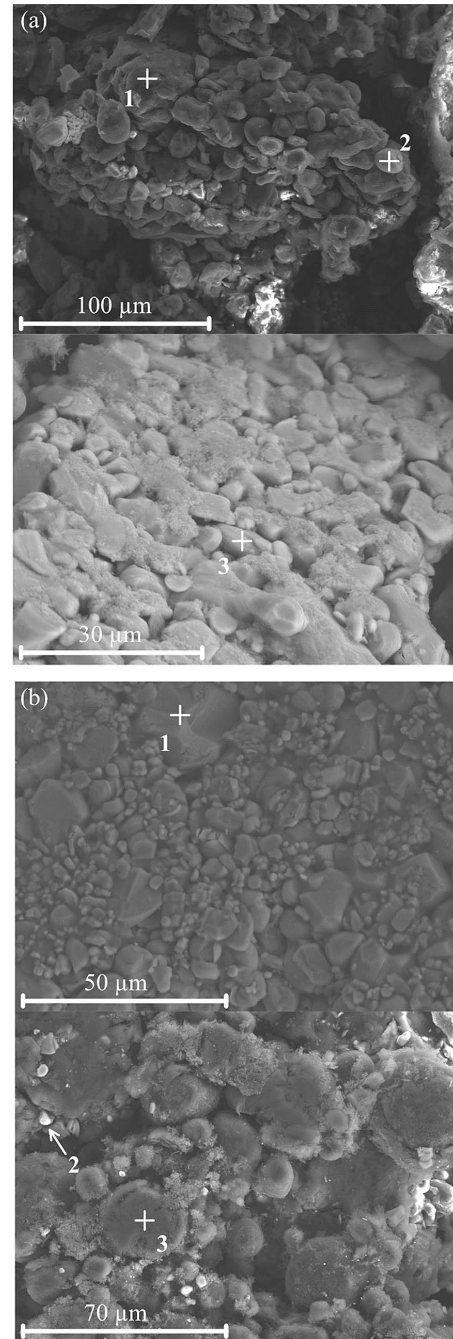

Fig. 2 SEM(SE)-EDS images of two fractions of the as-received LCO BM: **a** < 150 μm and **b** 150–700 μm
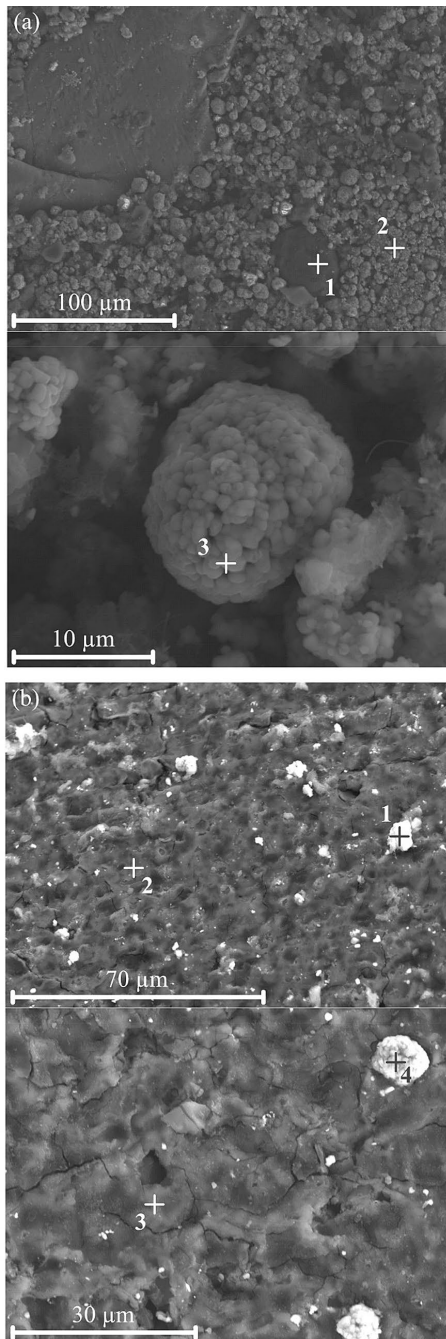
Fig. 3 SEM(SE)-EDS images of two fractions of the as-received NMC BM: **a** < 150 μm and **b** 150–700 μm

Thermal Analysis

BM from LCO Batteries

The TGA, DTA, and QMS results of the BM from LCO batteries are plotted in Fig. 4. To explain the behavior during heating, the heating profile was divided into three sections according to the mass loss slope and the occurring reactions. In section I, the mass loss, in the fine fraction, begins at ∼ 200–300 ℃ and continues until 5 wt% of the original mass is lost, while in the coarse fraction, it continues even further to approximately 10 wt% mass loss. Section I is associated with the production of hydrocarbons (C_xH_y), together with H_2O and CO_2, as depicted in the QMS graph. In the middle of this section, a breakpoint (for both fractions) is observed, which synchronizes with a slight bump in the DTA graph that is even more apparent in the coarse fraction. Section I is followed by a gentle slope in section II, where an exothermic reaction takes place at ~600 ℃. This reaction is not accompanied by any mass loss at that temperature, while sharp peaks of H_2O and CO_2 arise immediately thereafter (at slightly higher temperature) which synchronizes with a steeper slope in section III and continues until ∼ 900 ℃. The main mass loss, which is approximately 15–20 wt%, occurs in section III. At ∼ 900 ℃, an endothermic peak appears in the DTA graph accompanied by a CO_2 peak in the QMS graph.

In Fig. 5, XRD patterns obtained before and after reduction are shown. The as-received LCO BM mainly consists of $LiCoO_2$ and graphite, while the main phases in the reduced BM were Co and graphite. High-temperature XRD was also conducted to better comprehend the exo/endothermic reactions noticed in the DTA graphs (Fig. 6). Similar to the as-received LCO BM in Fig. 5, the pattern at 25 ℃ shows $LiCoO_2$ and graphite as the main phases, along with the less intense peaks of SiO_2 and Al_2O_3. When increasing the temperature to 550 ℃, CoO peaks arise, and when a temperature of 700 ℃ is reached the $LiCoO_2$ peaks disappear entirely and $AlLiO_2$ and Co phases appear. At 800 ℃, all CoO peaks disappear. When a temperature of 1000 ℃ is reached, a shift to the left in the peaks can be observed, an affect that could be attributed to lattice parameter changes by increasing temperature [27, 28]. After cooling the LCO BM from 1000 ℃, graphite, Co, SiO_2, and $AlLiO_2$ are the peaks recognized in the XRD pattern.

The TGA curves in Fig. 4b show that the mass reduction of the coarse fraction is slightly higher than that of the fine fraction (Fig. 4a). Even so, the thermal behaviors of the two fractions are almost similar in the two fractions; subsequently, the following explanations apply to both (fine and coarse LCO BM).

The chemical composition (Table 2) gives an indication that the amount of $LiCoO_2$ is the same in the fine and coarse
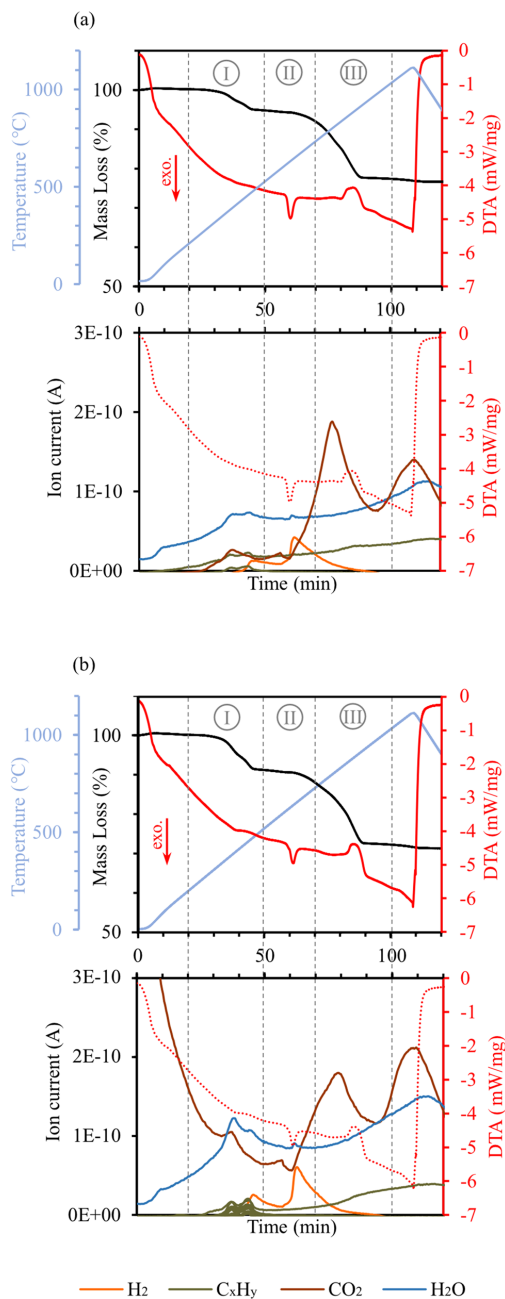
(a)

(b)

— H2   — CxHy   — CO2   — H2O

Fig. 4 TGA/DTA/QMS graphs of two fractions of the LCO BM: **a** < 150 μm and **b** 150–700 μm

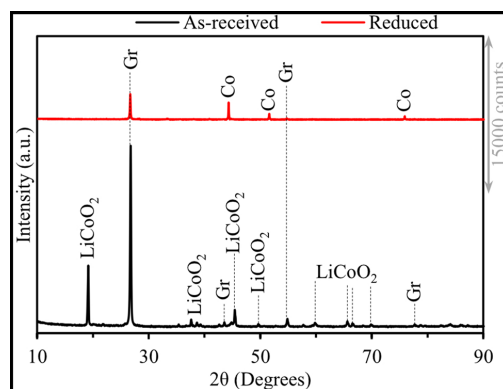**Fig. 5** XRD patterns of LCO BM before and after heat treatment at 1100 ℃

fractions of LCO BM, while more C was present in the fine fraction. Moreover, the XRD results (Fig. 5) demonstrate that graphite remains in the reduced coarse fraction, which has a lower amount of C. This implies that more C was present than what was needed to ultimately reduce $LiCoO_2$. In conclusion, more C in the fine fraction would result in more remaining C after the reduction and finally a lower total mass reduction.

In Fig. 4 section I, the evolved gases (C_xH_y, CO_2, and H_2O) indicate dissociation or decomposition of an organic compound, which could be the binder and/or residual solvents. PVDF, as a binder, is spread on the particles to maintain a bond between the cathode/anode active material, current collectors, and acetylene black [29, 30]. With the decomposition of PVDF, it is possible for the acetylene black to oxidize. Since compared to graphite, acetylene black oxidizes at a lower temperature [31], the breakpoint in the TGA curve (section I) can be addressed to the reduction reaction of LCO in the presence of acetylene black. This reaction reduces the cathode active material metals from a higher oxidation state to a lower oxidation state [32], followed by the formation of H_2O and CO_2 in the QMS results. This can also be verified by the high-temperature XRD patterns (Fig. 6), where CoO peaks appear at 550 ℃ while $LiCoO_2$ is still present. This implies that $LiCoO_2$ has been partially altered to its components.

Figure 4 section II shows a plateau in the mass loss curve and an exothermic peak at approximately 600 ℃ in the DTA graph. The XRD patterns at 550 and 700 ℃ (Fig. 6) are literally measured before and after this reaction. Given these patterns, $LiCoO_2$ has totally transformed to its components, of which one is CoO, and according to the QMS data CO_2 and H_2O also release. Consequently, the exothermic reaction at ~ 600 ℃ (Fig. 4) can be interpreted as a $LiCoO_2$
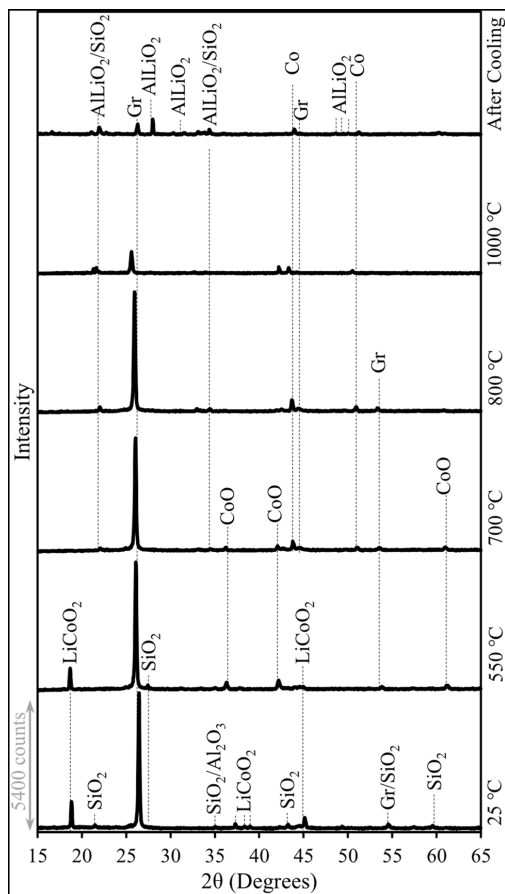
Fig. 6 XRD patterns during heating of the LCO BM to a temperature of 1000 ℃

transformation to simpler components. In addition, an H_2 peak is observed in the QMS data that can be interpreted as the product of the secondary devolatilization of organic materials/binder or residual plastics [33]. The diffractogram at 700 ℃ shows the beginning of CoO reduction where a Co phase forms.

To determine the nature of this reaction, chemical-grade $LiCoO_2$ reduction trials were performed as explained in the *Experimental* "$LiCoO_2$ Reduction" section. The results are plotted in Fig. 7. It should be mentioned that the temperature difference (~ 40 ℃) of the exothermic reaction in the LCO + Gr + Al + PVDF sample is due to the smaller graphite particle size, which improves the kinetics of the reaction.

First of all, $LiCoO_2$ was placed in an inert atmosphere and heated to 1100 ℃ and the figure shows that it did not

decompose until the temperature reached almost 1100 ℃; however, when graphite was added, the decomposition began at a much lower temperature (630–670 ℃). The same scenario is observed by the addition of Al and PVDF. The DTA graphs show that an exothermic reaction occurs at 630–670 ℃. The notable point is that the TGA graph shows no mass loss, implying that the reduction has not started at this point. S. Kuzuhara et al. (2020) reported that this exothermic reaction can be due to Eq. 1, which has no accompanying mass loss and is thermodynamically feasible at temperatures higher than 488 ℃ [34].

$$2LiCoO_2 + C \rightarrow Li_2CO_3 + Co + CoO \qquad (1)$$
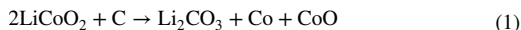
Increasing the temperature to ~ 680 ℃, the mass loss begins. It can be concluded that the reaction occurring at 630–670 ℃ (Eq. 1) facilitates reduction at higher temperatures (680 ℃). It is worth mentioning that the difference in reaction temperature between the synthetic $LiCoO_2$ mixture and LCO BM may be related to kinetic reasons such as the surface area and size of particles. The $LiCoO_2$ phase transformation is followed by the main mass loss. Considering Fig. 6 with the high-temperature XRD patterns (Fig. 6), it can be concluded that the reduction of Co oxides to metallic Co begins after the $LiCoO_2$ phase transformation.

The endothermic peak observed at ~ 800 ℃ is synchronized with a slope change in the mass loss. This reaction can be addressed to the decomposition of Li_2CO_3 to Li_2O and CO_2. This reaction can also be expected in the LCO BM, where CO_2 peaks are rising at this temperature (Fig. 4); however, Li_2CO_3 peaks were not detected by high-temperature XRD (Fig. 6). This may be because during LCO BM reduction, Li_2CO_3 forms at a temperature that is close to its melting point (733 ℃ [35]). Accordingly, the loss of the crystal structure at that temperature range might be the reason that Li_2CO_3 peaks are not identified in the XRD pattern.

The endothermic reaction detected at ~ 900 ℃ is attributed to the gasification of C (Boudouard reaction) [14] or Li_2O volatilization [21]. According to the FactSage calculations performed in this study, the emitted gas phase has a very low content of Li_2O, while the CO_2 peak after this reaction can be seen in the QMS graphs (Fig. 4). Hence, the gasification of C seems to be more feasible.

Total mass loss values of ~ 23 and ~ 29 wt% were observed in the case of fine and coarse fractions, respectively. To conclude, heating the LCO BM to 1100 ℃ in an inert atmosphere results in the production of Co as a metallic part, leaving behind excess unreacted graphite.

The equilibrium was calculated with FactSage (Fig. 8), which shows that the most abundant stable phases at 1100 ℃ would be the Co(s), graphite, and gas phases. The slag phase (referred to liquid/glass solution in FactSage) would mainly consists of Li_2O, which was not detected by XRD. $AlLiO_2$,

Fig. 7 TGA/DTA graphs of three different chemical-grade LCO compositions heated to 1100 °C
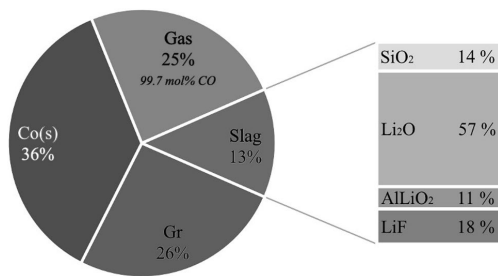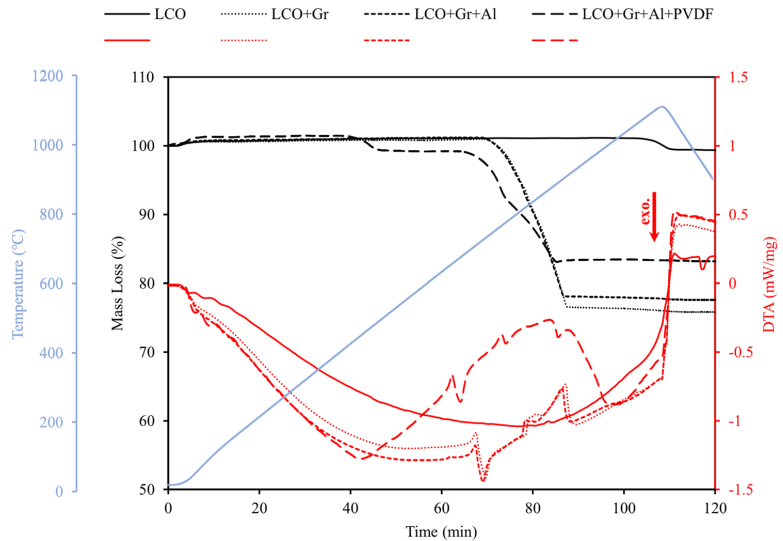

Fig. 8 LCO BM heat treated at 1100 °C, calculated by FactSage: Phase distribution and the slag calculated components

Fig. 9 Equilibrium mole fraction of CO and CO_2 with C based on the Boudouard reaction

LiF, and SiO_2 are also thermodynamically probable at this temperature. The thermodynamically estimated behavior of BM upon heating in an inert atmosphere is in line with the experimental results, except for Li-containing compounds. It seems that the Al content in the high-temperature XRD sample was higher than the average chemical composition, which made the $AlLiO_2$ the abundant Li-containing phase during heating. This difference might be due to the inhomogeneity of BM that commonly contains large current collector particles (Al and Cu), which might change the local chemical composition and make it difficult to obtain a representative sample.

To calculate the mass reduction by theoretical stoichiometry equations, the amount of O in the LCO BM should be considered. Theoretically, 32.7 wt% O exists in the $LiCoO_2$. To eliminate O, the C amount needed depends on the gas produced, i.e., CO or CO_2, which can be studied by the
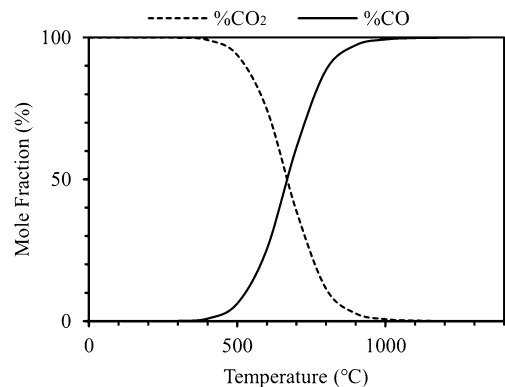
Boudouard reaction (Fig. 9). Therefore, it can be deduced that the $CO:CO_2$ ratio in the temperature range of LCO BM carbothermic reactions (600–900 °C) is approximately 3:1.

The total reduction of the cathode material by graphite (as the main reductant in the BM), considering the thermodynamics calculations, can be simplified to Eq. 2. In this case, the mass loss was ~ 23 wt%, which agrees with the total mass loss in the TGA curves. It is worth mentioning that in comparing the theoretical and experimental results, the mass loss ratio should be calculated after reaching a temperature of 500 °C because the mass loss before that is related to PVDF decomposition, which is not included in Eq. 2.

$$LiCoO_2 + 1.2C \rightarrow 0.5Li_2O + Co + 0.9CO + 0.3CO_2 \quad (2)$$
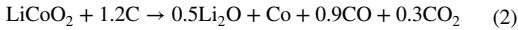
BM from NMC Batteries

Figure 10 depicts the TGA, DTA, and QMS results from the NMC BM during heating. Similar to the LCO BM, the mass loss trend has been divided into the following three sections: the mass loss begins in section I, slope plateaus form in section II, and section III begins with a steeper slope. Prior to section I and at its beginning, C_xH_y peaks arise at ~300 ℃ most likely attributed to the decomposition of PVDF. Fine and coarse fractions of NMC BM show four exothermic reactions at ~ 300, ~ 400, ~ 600, and ~ 800 ℃. The two latter reactions are followed by intense CO_2 and H_2O peaks in the QMS graphs.

The XRD patterns of the NMC BM before and after heating are illustrated in Fig. 11. The main phases in the as-received BM are $LiNi_{0.33}Mn_{0.33}Co_{0.33}O_2$ and graphite with a weak peak. The intensity of the graphite peak does not match the C content analyzed by combustion analysis. Hence, part of the C amount can be accounted for by acetylene black, whose main XRD peak is in the same 2θ as graphite, while, compared to graphite, its main peak is weak and broad [36]. This assumption will be discussed later in this section. The XRD pattern indicates that LiF and metallic Co and Ni are formed in addition to graphite after reduction.

The high-temperature XRD patterns in this case (Fig. 12) include a broad hump that is more discernible at room temperature and disappears gradually with increasing temperature. This bump might be related to an amorphous phase such as PVDF [22]. The phases detected at 25 ℃ were previously identified (Fig. 11) in the as-received BM XRD pattern (Fig. 11). There were also Cu peaks originating from the current collector residuals in the BM. At 550 ℃, SiO_2 was identified alongside $LiNi_{0.33}Mn_{0.33}Co_{0.33}O_2$, graphite, and Cu. At 700 ℃, the Co/Ni and MnO peaks replaced the $LiNi_{0.33}Mn_{0.33}Co_{0.33}O_2$ peaks. The pattern remained almost constant at 900 and 1000 ℃. After cooling from 1000 ℃ to room temperature, the final phases can be summarized as SiO_2, Co/Ni, graphite, MnO, LiF, and Cu.

Unlike the BM from LCO, the NMC BM fractions showed significant variations in their compositions with fractionation (Table 2). This difference is distinguishable in the mass loss curves in Fig. 10, where the coarse fraction with the higher amount of C has a lower total mass reduction. The limited amount of reducible oxygen can explain the lower mass loss in the coarse fraction compared to the fine fraction. The total mass loss amounts were found to be ~ 33 and ~ 25 wt% for the fine and coarse fractions, respectively. The same TGA trend as for the LCO BM is observed in section I of the TGA curve for NMC BM, where PVDF decomposition (~ 300 ℃) and acetylene black oxidation
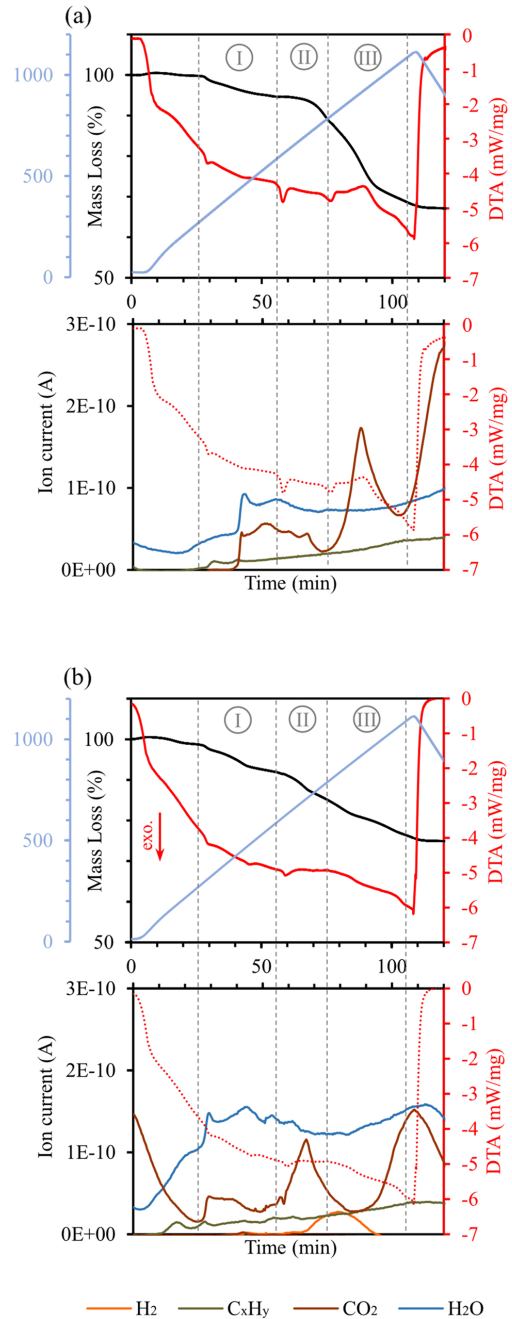

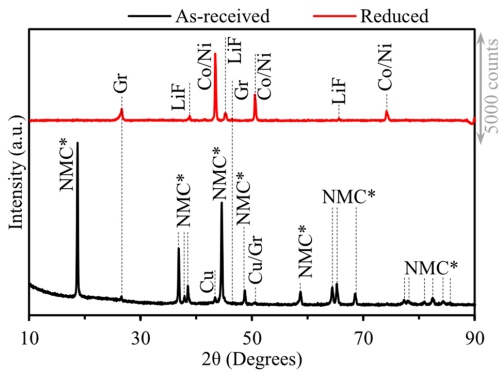**Fig. 10** TGA/DTA/QMS graphs of two fractions of the NMC BM: **a** < 150 μm and **b** 150–700 μm

Fig. 11 XRD patterns of NMC BM before and after heat treatment at 1100 ℃

(~ 400 ℃) occurred. The mass loss in section II continues with a different slope, and QMS peaks corresponding to CO_2 and H_2O are observed immediately after the exothermic reaction at ~ 600 ℃ (Fig. 10). The XRD patterns at 550 and 700 ℃ in Fig. 12 show that $LiNi_{0.33}Mn_{0.33}Co_{0.33}O_2$ transformed to metallic Co and Ni and MnO in that temperature interval. Accordingly, at ~ 600 ℃, the transformation of $LiNi_{0.33}Mn_{0.33}Co_{0.33}O_2$ in the BM occurs, which has also been reported by Vishvakarma and Dhawan [14]. Unlike in the LCO BM, mass loss can also be observed at ~ 600 ℃ for NMC BM, where the main transformation of $LiNi_{0.33}Mn_{0.33}Co_{0.33}O_2$ occurs. Moreover, as discussed, it seems that a significant part of the C in the BM is acetylene black, whose oxidation was detectable (because of its content) at ~ 400 ℃ in the DTA graph. Therefore, it can be concluded that part of the transformation and reduction of the NMC cathode material begins at ~ 400 ℃, where acetylene black acts as the reductant.

Section III, including the highest mass loss rate, begins immediately after phase transformation at ~ 600 ℃. A bump between 700 and 800 ℃ is observed in the DTA curve, which is more obvious in the fine fraction (Fig. 10a). Similar to the discussion in the LCO BM section, it can be accounted for by the decomposition of Li_2CO_3 into Li_2O and CO_2. After reduction, the Co/Ni phase forms, while part of the graphite remains unreacted. MnO and SiO_2 remain in the sample, which agrees with the FactSage calculations (Fig. 13), and part of the MnO remains unreacted even at 1100 ℃. Moreover, there are LiF peaks that do not exist in the LCO XRD pattern. In Table 2, the F amounts are reported as 2.6 and 6.5 wt% in the LCO and NMC BM, respectively. Hence, the higher concentration of F in the NMC BM might lead to the formation of a detectable amount of LiF in the XRD pattern.

The experimental data obtained were compared to the FactSage modeling results (Fig. 13). FactSage shows that
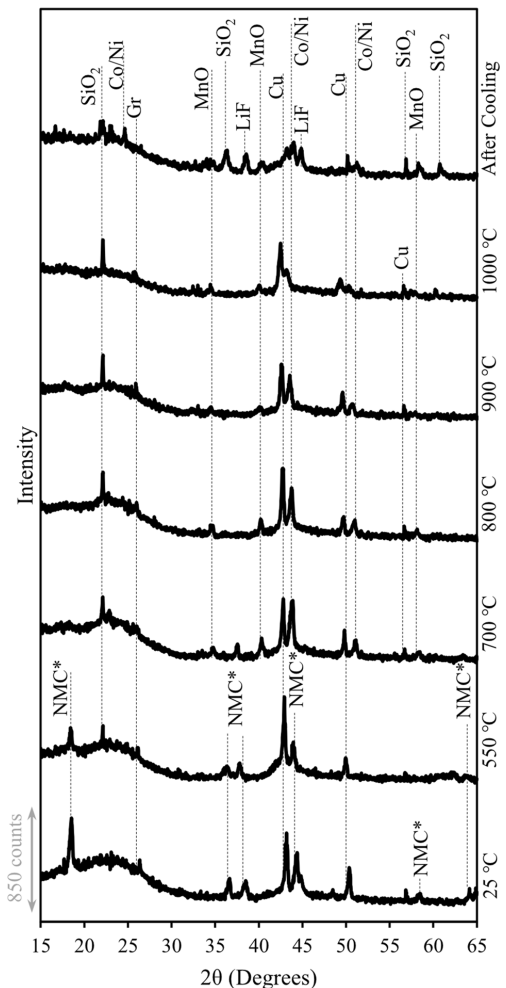
Fig. 12 XRD patterns during heating of the NMC BM to a temperature of 1000 ℃

a higher amount of F in NMC resulted in the formation of some fluorides—e.g., LiF, MnF_2, and SiF_4. In the other words, the thermodynamic calculations demonstrated that MnO and Li_2O partially react with F and form Mn and Li fluorides.

In the mass balance calculations, the reduction was assumed to be performed with C as the main reductant. In that regard, a $CO:CO_2$ ratio of 3:1 was selected as the composition of the produced gas, as previously explained. Since the total mass loss is the concern of this calculation, the formation of Mn/Li fluorides are considered as reduced Mn

and Li in the equations. Accordingly, three types of equations can be considered based on their products, as follows:

- Co, Ni, Mn, and Li (Eq. 3);
- Co, Ni, Mn, and Li_2O (Eq. 4); and
- Co, Ni, MnO, and Li_2O (Eq. 5).

$$LiNi_{0.33}Mn_{0.33}Co_{0.33}O_2 + 1.6C \rightarrow 0.33Ni + 0.33Mn + 0.33Co + Li + 1.2CO + 0.4CO_2 \tag{3}$$

$$LiNi_{0.33}Mn_{0.33}Co_{0.33}O_2 + 1.2 \rightarrow 0.33Ni + 0.33Mn + 0.33Co + 0.5Li_2O + 0.9CO + 0.3CO_2 \tag{4}$$

$$LiNi_{0.33}Mn_{0.33}Co_{0.33}O_2 + 0.9C \rightarrow 0.33Ni + 0.33MnO + 0.33Co + 0.5Li_2O + 0.7CO + 0.2CO_2 \tag{5}$$
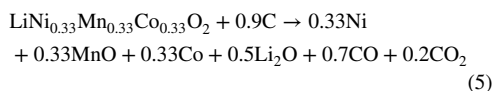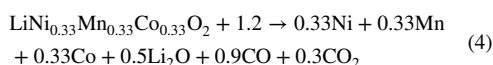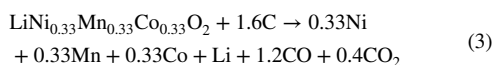
The experimental mass loss percentages were calculated after a temperature of 500 ℃ (PVDF decomposition) was reached and they were 20.4 wt% in the coarse fraction and 29.5 wt% in the fine fraction. The calculated mass loss percentages in Eqs. 3, 4, and 5 were 28.2 wt%, 21.1 wt%, and 15.6 wt%, respectively. Then, it can be speculated that in the coarse fraction, Ni and Co were fully reduced; however, Li and Mn oxides partially reacted with F. Regarding the fine fraction, the high mass loss can be attributed to the late devolatilization of organic materials (binders).

F Behavior

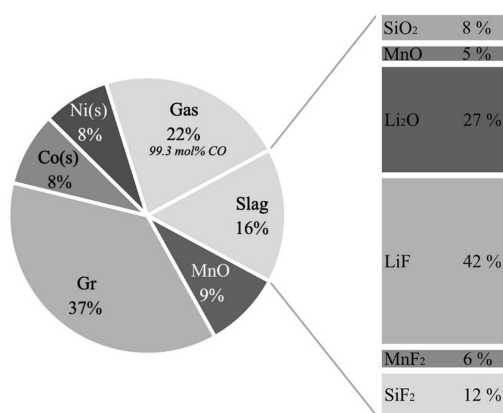NMC had a larger amount of F than LCO, and based on that, it was selected as the primary sample in this part of the

Fig. 13 NMC BM heat treated at 1100 ℃, calculated by FactSage: Phase distribution and the slag calculated components
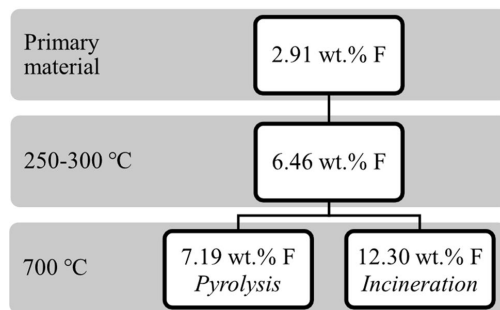

Fig. 14 F content after various heat treatment conditions

study. The F content after four different thermal treatments is listed in Fig. 14. The primary NMC BM had only 2.91 wt% F, while it increased to 6.46 wt% by removal of electrolyte at 250–300 ℃. After pyrolysis at 700 ℃, there was 7.19 wt% F in the BM, whereas it increased to 12.30 wt% after incineration at the same temperature.

As explained before, after transformation of the cathode material, Li_2CO_3 forms, decomposing into Li_2O and CO_2 at higher temperatures. The possible reactions that might occur with F and the oxides can be summarized as Eqs. 6 and 7, as simulated by FactSage:

$$2Li_2CO_3 + 4F \rightarrow 4LiF + 2CO_2 + O_2 \tag{6}$$

$$2Li_2O + 4F \rightarrow 4LiF + O_2 \tag{7}$$
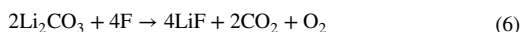
The QMS results in Fig. 10 show that hydrocarbons (C_xH_y) were released in section I—i.e., at temperatures lower than 500 ℃—which is a sign of PVDF decomposition in the BM. Comparing those data with the variation in F content in Fig. 14 indicates that heat treatment, even at 700 ℃, might produce hydrocarbons but does not remove F at that temperature. In addition, it seems that incineration results in a higher final F content than pyrolysis. It should be taken into account that in an oxidative atmosphere (incineration), graphite reacts with oxygen in the atmosphere and produces CO/CO_2. Thus, the BM mass loss in the air ($\sim$ 52 wt%) is higher than that in the Ar atmosphere ($\sim$ 19 wt%). Normalizing the F content after heating at 700 ℃ based on the mass loss in both the pyrolysis and incineration processes demonstrates that the F amount removed from 100 g of BM are approximately 0.63 and 0.56 g in Ar and air atmospheres, respectively. This reveals that there might be some emission of C_xH_y, but it does not significantly affect the absolute F content.

The FactSage calculations, in line with the experimental results, show that F accumulated in the solid-state and did not evaporate in this range of working temperatures. It can

Table 3 Calculated thermodynamic data regarding the F behavior at 700 ℃

Heat treatment/atmosphere	F content (s) Experimental	F content (s) Calculated	F-containing phases Calculated
Pyrolysis/Ar	7.19	8.31	LiF
Incineration/air	12.30	13.21	LiF, $Li_2SiO_3(LiF)_2$

be observed in Table 3 that the experimental and calculated data agree. Based on these thermodynamic calculations, F accumulates in the solid-state in the form of LiF after pyrolysis, and after incineration, LiF and $Li_2SiO_3(LiF)_2$ are supposed to form. According to thermodynamic modeling, 79% of F in the solid-state is in the form of LiF, and the rest is in the $Li_2SiO_3(LiF)_2$ phase.

In this study, it was shown that regardless of the BM particle size, the morphological and mineralogical properties of the BM were almost the same. The main difference was in the amount of binders and graphite, which had a direct effect on the mass loss. The amounts of Li and F in the solid-state were also analyzed and tracked in the XRD measurements and the thermodynamic calculations. During thermal treatment of the BM, 600 ℃ was found to be a critical temperature for breaking the complex structure of the cathode material, which was followed by carbothermic reduction of the metallic oxides in the BM to obtain metallic Co and Ni (in the case of the NMC BM). Li was found in the form of $AlLiO_2$ after heat treatment at a low concentration of F, while the Li-containing phase changed to LiF at a high F content in the BM. F persisted in the BM, even after PVDF decomposition and the emission of hydrocarbons, regardless of whether the heat treatment was conducted in an inert or an oxidative atmosphere.

Conclusion

A characterization routine including the BM thermal behavior was investigated based on chemical, morphological, mineralogical, and thermal analyses. ICP seems to be the most appropriate tool to quantify the main elements in the BM, such as Co, Ni, Mn, and Li. The ISE method was found to be a reliable technique to quantify F. The volatile content in the BM was determined utilizing TGA coupled with QMS. Although the total volatile content can be quantified, it was not possible to obtain detailed information on the volatile composition using the existing analytical tools. The presence of residual binder was identified in the SEM images, and its quantity along with acetylene black was further determined by TGA in the temperature range of 200–500 ℃. It was found that 5–10 wt% of the BM consisted of residual binders (mainly PVDF) and acetylene black. During thermal analysis, an exothermic peak at ~ 600 ℃ in both BM types was attributed to the transformation of $LiCoO_2$ and

$LiNi_{0.33}Mn_{0.33}Co_{0.33}O_2$ to their constituting metal oxides/lower oxides. Transformation in both BM types was followed by the main mass loss, which indicated that reduction was possible only after the transformation of complex oxides to simpler oxides. The XRD results confirmed this observation at high temperatures. In the BM from NMC batteries, where F is higher in concentration than in the BM from LCO batteries, LiF formation was also observed. All observations were thermodynamically calculated and confirmed through FactSage software.

By following the F behavior during heating as a pretreatment and employing the ISE method for the analysis of F in the solid sample, it was proven that although hydrocarbons were emitted from binder decomposition, F remained in the sample even after heat treatment at 700 ℃ in both oxidative and inert atmospheres.

Based on this study, it can be stated that a considerable amount of graphite in the BM can be utilized as a reducing agent, and Co-based alloys can be successfully produced through simple pyrometallurgical treatment of BM. A study on the addition of external oxygen to the BM to efficiently utilize excess graphite will be performed later.

Declarations

References

1. Zhang W, Xu C, He W, Li G, Huang J (2018) A review on management of spent lithium ion batteries and strategy for resource recycling of all components from them. Waste Manag Res J Sustain Circ Econ 36:99–112. https://doi.org/10.1177/0734242X17744655

2. Zheng X, Zhu Z, Lin X, Zhang Y, He Y, Cao H, Sun Z (2018) A mini-review on metal recycling from spent lithium ion batteries. Engineering 4:361–370. https://doi.org/10.1016/j.eng.2018.05.018

3. Ruismäki R, Rinne T, Dańczak A, Taskinen P, Serna-Guerrero R, Jokilaakso A (2020) Integrating flotation and pyrometallurgy for recovering graphite and valuable metals from battery scrap. Metals 10:680. https://doi.org/10.3390/met10050680

4. Makuza B, Tian Q, Guo X, Chattopadhyay K, Yu D (2021) Pyrometallurgical options for recycling spent lithium-ion batteries: a comprehensive review. J Power Sources 491:229622. https://doi.org/10.1016/j.jpowsour.2021.229622

5. European Commission (2020) Proposal for a REGULATION OF THE EUROPEAN PARLIAMENT AND OF THE COUNCIL concerning batteries and waste batteries, repealing Directive 2006/66/EC and amending Regulation (EU) No 2019/1020. https://eur-lex.europa.eu/legal-content/EN/TXT/?uri=CELEX%3A52020PC0798. Accessed 26 Aug 2021

6. Melin E (2019) State-of-the-art in reuse and recycling of lithium-ion batteries—a research review. Circ. Energy Storage. http://www.energimyndigheten.se/globalassets/forskning--innovation/overgripande/state-of-the-art-in-reuse-and-recycling-of-lithium-ion-batteries-2019.pdf. Accessed 4 Aug 2021

7. Boyden A, Soo VK, Doolan M (2016) The environmental impacts of recycling portable lithium-ion batteries. Procedia CIRP 48:188–193. https://doi.org/10.1016/j.procir.2016.03.100

8. Velázquez-Martínez O, Valio J, Santasalo-Aarnio A, Reuter M, Serna-Guerrero R (2019) A critical review of lithium-ion battery recycling processes from a circular economy perspective. Batteries 5:68. https://doi.org/10.3390/batteries5040068

9. Harper G, Sommerville R, Kendrick E, Driscoll L, Slater P, Stolkin R, Walton A, Christensen P, Heidrich O, Lambert S, Abbott A, Ryder K, Gaines L, Anderson P (2019) Recycling lithium-ion batteries from electric vehicles. Nature 575:75–86. https://doi.org/10.1038/s41586-019-1682-5

10. Mossali E, Picone N, Gentilini L, Rodrìguez O, Pérez JM, Colledani M (2020) Lithium-ion batteries towards circular economy: a literature review of opportunities and issues of recycling treatments. J Environ Manag 264:110500. https://doi.org/10.1016/j.jenvman.2020.110500

11. Or T, Gourley SWD, Kaliyappan K, Yu A, Chen Z (2020) Recycling of mixed cathode lithium-ion batteries for electric vehicles: current status and future outlook. Carbon Energy 2:6–43. https://doi.org/10.1002/cey2.29

12. Zhang G, He Y, Feng Y, Wang H, Zhu X (2018) Pyrolysis-ultrasonic-assisted flotation technology for recovering graphite and LiCoO$_2$ from spent lithium-ion batteries. ACS Sustain Chem Eng 6:10896–10904. https://doi.org/10.1021/acssuschemeng.8b02186

13. Liu W, Zhong X, Han J, Qin W, Liu T, Zhao C, Chang Z (2019) Kinetic study and pyrolysis behaviors of spent LiFePO$_4$ batteries. ACS Sustain Chem Eng 7:1289–1299. https://doi.org/10.1021/acssuschemeng.8b04939

14. Vishvakarma S, Dhawan N (2019) Recovery of cobalt and lithium values from discarded Li-ion batteries. J Sustain Metall 5:204–209. https://doi.org/10.1007/s40831-018-00208-4

15. Yu J, He Y, Ge Z, Li H, Xie W, Wang S (2018) A promising physical method for recovery of LiCoO$_2$ and graphite from spent lithium-ion batteries: grinding flotation. Sep Purif Technol 190:45–52. https://doi.org/10.1016/j.seppur.2017.08.049

16. Kim S, Bang J, Yoo J, Shin Y, Bae J, Jeong J, Kim K, Dong P, Kwon K (2021) A comprehensive review on the pretreatment process in lithium-ion battery recycling. J Clean Prod 294:126329. https://doi.org/10.1016/j.jclepro.2021.126329

17. Brückner L, Frank J, Elwert T (2020) Industrial recycling of lithium-ion batteries—a critical review of metallurgical process routes. Metals 10:1107. https://doi.org/10.3390/met10081107

18. Chen X, Kang D, Li J, Zhou T, Ma H (2020) Gradient and facile extraction of valuable metals from spent lithium ion batteries for new cathode materials re-fabrication. J Hazard Mater 389:121887. https://doi.org/10.1016/j.jhazmat.2019.121887

19. Yang Y, Lei S, Song S, Sun W, Wang L (2020) Stepwise recycling of valuable metals from Ni-rich cathode material of spent lithium-ion batteries. Waste Manag 102:131–138. https://doi.org/10.1016/j.wasman.2019.09.044

20. Jian Y, Zongliang Z, Gang Z, Liangxing J, Fangyang L, Ming J, Yanqing L (2021) Process study of chloride roasting and water leaching for the extraction of valuable metals from spent lithium-ion batteries. Hydrometallurgy 203:105638. https://doi.org/10.1016/j.hydromet.2021.105638

21. Wang W, Zhang Y, Liu X, Xu S (2019) A simplified process for recovery of Li and Co from spent LiCoO$_2$ cathode using Al foil as the in situ reductant. ACS Sustain Chem Eng. https://doi.org/10.1021/acssuschemeng.9b01564

22. Lombardo G, Ebin B, St Foreman MRJ, Steenari BM, Petranikova M (2019) Chemical transformations in Li-ion battery electrode materials by carbothermic reduction. ACS Sustain Chem Eng 7:13668–13679. https://doi.org/10.1021/acssuschemeng.8b06540

23. Lombardo G, Ebin B, Foreman MR, Steenari BM, Petranikova M (2020) Incineration of EV Lithium-ion batteries as a pretreatment for recycling—determination of the potential formation of hazardous by-products and effects on metal compounds. J Hazard Mater 393:122372. https://doi.org/10.1016/j.jhazmat.2020.122372

24. Kwon OS, Sohn I (2020) Fundamental thermokinetic study of a sustainable lithium-ion battery pyrometallurgical recycling process. Resour Conserv Recycl 158:104809. https://doi.org/10.1016/j.resconrec.2020.104809

25. Bale CW, Bélisle E, Chartrand P, Decterov SA, Eriksson G, Gheribi AE, Hack K, Jung IH, Kang YB, Melançon J, Pelton AD, Petersen S, Robelin C, Sangster J, Spencer P, Van E-A (2016) FactSage thermochemical software and databases—2010–2016. Calphad 54:35–53

26. Nitta N, Wu F, Lee JT, Yushin G (2015) Li-ion battery materials: present and future. Mater Today 18:252–264. https://doi.org/10.1016/j.mattod.2014.10.040

27. Hallam KR, Darnbrough JE, Paraskevoulakos C, Heard PJ, Marrow TJ, Flewitt PEJ (2021) Measurements by X-ray diffraction of the temperature dependence of lattice parameter and crystallite size for isostatically-pressed graphite. Carbon Trends 4:100071. https://doi.org/10.1016/j.cartre.2021.100071

28. Suryanarayana C, Norton MG (1998) X-ray diffraction: a practical approach. Springer, New York

29. An L (2019) Recycling of spent lithium-ion batteries. Springer, Cham

30. Ross BJ, LeResche M, Liu D, Durham JL, Dahl EU, Lipson AL (2020) Mitigating the impact of thermal binder removal for direct Li-ion battery recycling. ACS Sustain Chem Eng 8:12511–12515. https://doi.org/10.1021/acssuschemeng.0c03424

31. Hanisch C, Loellhoeffel T, Diekmann J, Markley KJ, Haselrieder W, Kwade A (2015) Recycling of lithium-ion batteries: a novel method to separate coating and foil of electrodes. J Clean Prod 108:301–311. https://doi.org/10.1016/j.jclepro.2015.08.026

32. Yang Y, Huang G, Xu S, He Y, Liu X (2016) Thermal treatment process for the recovery of valuable metals from spent lithium-ion batteries. Hydrometallurgy 165:390–396. https://doi.org/10.1016/j.hydromet.2015.09.025

33. Ahmed H, Sideris D, Björkman B (2020) Injection of H_2-rich carbonaceous materials into the blast furnace: devolatilization, gasification and combustion characteristics and effect of increased H_2–H_2O on iron ore pellets reducibility. J Mater Res Technol 9:16029–16037. https://doi.org/10.1016/j.jmrt.2020.11.042

34. Kuzuhara S, Ota M, Tsugita F, Kasuya R (2020) Recovering lithium from the cathode active material in lithium-ion batteries via thermal decomposition. Metals 10:1–13. https://doi.org/10.3390/met10040433

35. Kim JW, Lee HG (2001) Thermal and carbothermic decomposition of Na_2CO_3 and Li_2CO_3. Metall Mater Trans B Process Metall Mater Process Sci 32:17–24. https://doi.org/10.1007/s11663-001-0003-0

36. Yang L, Yang L, Xu G, Feng Q, Li Y, Zhao E, Ma J, Fan S, Li X (2019) Separation and recovery of carbon powder in anodes from spent lithium-ion batteries to synthesize graphene. Sci Rep 9:9823. https://doi.org/10.1038/s41598-019-46393-4

Paper II

Mechanical Activation-Assisted Recovery of Valuable Metals from Black Mass in the Form of Fe/Cu Alloys

Safoura Babanejad[1] · Hesham Ahmed[1,2] · Charlotte Andersson[1] · Eetu-Pekka Heikkinen[3]

Abstract

Pyrometallurgy is a popular industrial method that is employed in the recovery of valuable elements from black mass (BM), which is produced by pretreatment of Li-ion batteries. This method struggles with some downsides, such as the incineration of graphite and high energy consumption. In this study, the goal is to utilize graphite in the BM to produce a master alloy in an attempt to decrease the energy input requirement. To achieve this, metal oxides (Fe_2O_3 and CuO) are added to the BM to produce an Fe/Cu-based alloy containing Co/Ni as alloying elements. Mechanical activation is also employed to decrease the energy requirement and to increase the amount of metal oxide that can be reduced by the graphite in the BM. The results revealed that it is possible to produce the aforementioned alloys, the efficiency of which can be improved by applying mechanical activation. After 1 h of milling, the required heat flow for producing Fe- and Cu-based alloys is lowered for ~10 and ~25 kWh, respectively. Plus, the direct CO_2 emission decreases for 13–17% in the iron system and 43–46% in the copper system.

Graphical Abstract
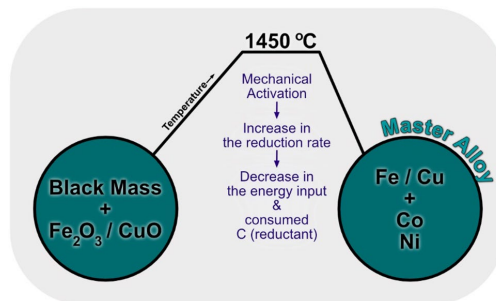
The contributing editor for this article was Markus Reuter.

✉ Safoura Babanejad
   safbab@ltu.se

✉ Hesham Ahmed
   hesham.ahmed@ltu.se

1   Department of Civil, Environmental and Natural Resource Engineering, Process Metallurgy, Minerals and Metallurgical Engineering, Luleå University of Technology, 971 87 Luleå, Sweden

2   Central Metallurgical Research and Development Institute, P.O. Box 87, Helwan 114 21, Egypt

3   University of Oulu, Process Metallurgy, PO Box 4300, 90014 Oulu, Finland

🖄 Springer

Abbreviations

LIB	Li-ion battery
EU	European Union
BM	Black mass
MeO	Metal oxide
$LiMeO_2$	Li metal oxide
LCO	A type of battery consisting of $LiCoO_2$ as the cathode material and graphite as the anode material
NMC	A type of battery consisting of $LiNi_xMn_yCo_zO_2$ (in this study: $x = y = z = 0.33$) as the cathode material and graphite as the anode material
TGA	Thermogravimetric analysis
PSD	Particle size distribution
XRD	X-ray diffraction

Introduction

"Lithium-ion batteries have indeed become the critical pillar for building a fossil fuel-free economy" [1]. The consumption of fossil fuels has led to global warming. This issue drag the public attention to renewable energies, which are not applicable unless by using rechargeable batteries, especially LIBs [2]. The production technologies for manufacturing batteries have been developed significantly in the recent years; New battery chemistries have been introduced, new manufacturing methods have been developed, and scale of manufacturing has increased. These have led to a price drop (almost 90% since 2010) in the LIBs for electric vehicles [3]. This drop in the manufacturing costs make the recycling seem costly. Moreover, the global recycling rate of LIBs is already low today, with less than 5% of LIBs being recycled in 2020 [1]. Hence, if efficient and economical recycling methods are developed, the recovery of LIB elements would replace the extraction of these elements from primary resources. It will have a direct effect on the economic and resource issues in this sector. The importance of recycling and its positive outcome has also been asserted by the EU Battery Directive (2006/66/EC) [4]. Co, graphite, and Li (key elements in a broad range of portable batteries and electric vehicles) are known as critical raw materials in the EU due to limitations in their geological availability, geopolitics, and market [5, 6].

The recycling methods mostly begin with a pretreatment step that can be mechanical, chemical, or thermal. During pretreatment step, the LIB particles are liberated and the critical and precious elements are concentrated in a fine fraction, called black mass (BM) [7, 8]. The main process to recover valuable metals from BM is either hydrometallurgical, pyrometallurgical, or a combination of these two. In stand-alone hydrometallurgical processes, such as Recupyl and Batrec, special attention is given to pretreatment to prepare the BM for subsequent leaching and solvent extraction. While in the pyrometallurgical process, e.g., Inmetco and Glencore, an alloy consisting of Ni, Co, Cu and Fe is produced with Al and Li accumulated in a slag phase. Thereafter, the produced alloy can be refined in a hydrometallurgical procedure, as is done in Umicore [9–11].

Compared to hydrometallurgical, the advantages of the pyrometallurgical methods can be listed as follows: (i) it is more flexible since the technology does not need to be specified for different LIB types and some of the current technologies are capable of recycling all types of batteries, e.g., Valdi, Glencore, and Dowa; (ii) there are high capacity available technologies; and (iii) the passivation step is not necessarily required [7, 12]. However, high energy demand plus CO_2 emission limits the implementation of pyrometallurgical processes [12, 13]. Since the pyrometallurgical process is done at elevated temperatures, in an oxidative atmosphere, graphite can burns out, like what occurs during incineration [14–16]. If the process would be in a reductive atmosphere, graphite can be used as a reducing agent, although the graphite in the BM is more than the required C for the reduction of $LiMeO_2$ in the BM. It can thus be expected that part of the graphite remains unreacted after reduction [17–20].

A decrease in working temperature of a pyrometallurgy process would lower the energy consumption in this method. To achieve this, mechanical activation can be employed. Mechanical activation of minerals and mixed oxides through milling decreases the particle size and increases their energy state, which leads to an increase in the thermal reactivity and subsequently a decrease in the required working temperature. Mechanical activation of, for example, hematite concentrate, galena, and pyrite has been investigated, and their thermal behaviour was compared to that of nonactivated minerals. The reduction temperature of hematite as well as thermal decomposition of galena and pyrite was lowered significantly [21–26]. It has been reported that the mechanical activation of carbon-containing mixed oxide systems enhances the carbothermic reduction kinetics [27]. BM is also a material containing C and MeOs, however, the effect of mechanical activation on its thermal behaviour has not been studied thus far.

In the known pyrometallurgical recovery methods, the graphite in the BM is mostly incinerated before or during melting, which is not a proper method for its utilization. On the other hand, the process is energy-intensive, where mechanical activation can be a method for lowering energy consumption during recovery. In the current study, a pyrometallurgy-based method is proposed for recycling of LIB components. This study aims at taking advantage of the graphite present in the BM. Two different MeOs (Fe_2O_3 and CuO) were added to the BM to utilize its graphite as a reducing agent. The feasibility of producing a master alloy

containing Co/Ni (in the BM) as alloying elements was assessed. Additionally, mechanical activation was employed as a process for creating disorder and defects in the lattice structure and increasing the active surface area to increase the reduction efficiency of the BM or BM/MeO mixture by changing the required energy and C consumption.

Experimental

Materials

The BMs from LCO and NMC LIBs were provided by Stena Recycling International AB, Sweden. Samples with a particle size of 150–700 μm were the focus of the present investigation, and their detailed description was given in an earlier publication [28]. Their composition is listed in Table 1. Fe_2O_3 (−325 mesh, 98%, Alfa Aesar) and CuO (97.5%, AnalaR NORMAPUR) were utilized in the alloying trials.

Characterization

A PSD analyzer (Retsch Camsizer XT) was utilized in this study to determine the size of the BM particles. A PANalytical Empyrean X-ray diffractometer using CuKα radiation ($\lambda = 0.154184$ nm) was used in a 2θ range of 10–90° with a step size of 0.026°/s. Phase identification was performed using HighScore Plus software (v4.7, PANalytical B.V., Almelo, The Netherlands). To analyze the C content in the BM, an EA3000 CHNS-O elemental analyzer from Eurovector Srl was employed (DIN 51,732). Inductively Coupled Plasma–Mass Spectrometry (ICP–MS) was used to analyze the chemical composition. The analysis was done according to SS EN ISO 17294–2:2016 and EPA method 200.8:1994.

Reduction-Alloying Trials

Initially, Fe/Cu oxides were added to the BM to utilize its excess graphite and to produce Fe/Cu-based alloys. The MeOs were mixed with BM in such a way that the net C/O molar ratio was equal to unity. The C content of the BM was accounted for in this C/O molar ratio. O in the cathode active material plus O in the added MeO (Fe_2O_3 or CuO) were considered as the reducible O in the C/O molar ratio. In this regard, the ratio of added MeOs to the BM is listed in Table 2. In the following parts of this paper, the prepared mixtures will be addressed as noted in this table.

Table 2 Description of utilized mixtures

Mixture	MeO (g):BM (g)
MixFeLCO	55.0:45.0 Fe_2O_3:LCO
MixFeNMC	60.5:39.5 Fe_2O_3:NMC
MixCuLCO	59.5:40.5 CuO:LCO
MixCuNMC	67.0:33.0 CuO:NMC

Second, a Fritsch Pulverisette 7 Planetary micromill was used to mechanically activate the BM and MeO-BM mixtures. The 80 ml cups in this ball mill consisted of 10 hardened steel balls with a diameter of 15 mm. To avoid excessive heat during milling, each 30 min of milling was followed by 15 min of cooling. The sample-to-balls ratio and rotating speed were fixed to 20 g of sample and 10 balls and 700 rpm, respectively, for the predetermined periods.

The prepared BM and MeO-BM mixtures underwent reduction-alloying experiments utilizing TGA (Netzsch STA 409) with a detection limit of 1 μg and an Ar flow rate of 100 ml/min. ~1 g sample was used in each experiment. In the trials applied on the BM, the temperature was increased linearly at a heating rate of 10 °C/min up to 1100 °C. The heating was followed by linear cooling to 200 °C at a rate of 20 °C/min. In the MeO-BM mixture trials, the samples were heated linearly up to 1450 °C at a heating rate of 10 °C/min, held at that temperature for 1 h, and then cooled to 200 °C at a rate of 20 °C/min.

Thermodynamic Modeling

FactSage 8.0™ software has been utilized as a thermodynamic calculation tool to study the reactions occurring at high temperature [29]. The Equilib module, employing FactPS, FToxid, and FTmisc databases, was used in these calculations. The ideal gas and pure solids as the main species along with the solution phases, as listed below, were considered:

- *FToxid-SLAGA*;
- *FToxid-SPINA*;
- *FToxid-MeO_A;*
- *FToxid-NAShB*;
- *FToxid-NASlB*;
- *FTmisc-FeLQ*; and
- *FTmisc-CuLQ* (since Co is not included in this solution phase, *Co(liq)* was added as an ideal solution).

Table 1 The chemical compositions of LCO and NMC BM (wt. %) [28]

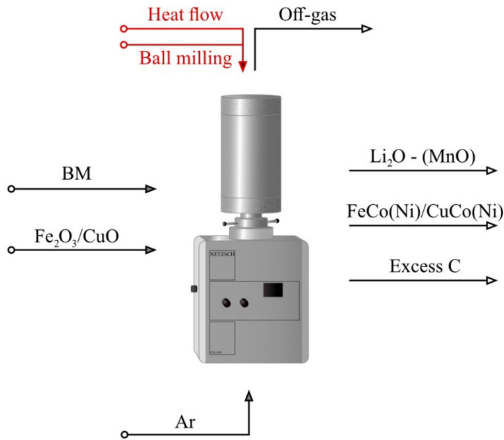| Sample (wt.%)	Li	Co	Ni	Mn	Al	Cu	Si	P	F	C
LCO BM	4.0	32.3	0.0	0.0	0.9	0.6	1.6	0.5	2.6	35.4
NMC BM	3.6	8.0	7.3	7.6	0.2	1.6	1.0	0.6	6.5	43.2

Fig. 1 Input and output flows used in the mass and energy balance

Mass and energy balances were made to estimate the energy requirements, the exergy loss, as well as CO_2 emissions of different cases and they were made by means of HSC Chemistry v. 10.0.7 and the regarded databases. The key elements during reduction were considered in these calculations, i.e., Co, Ni, Mn, C, Fe, O, and Li. The input and output flows were designed as demonstrated in Fig. 1. The output components were selected based on the results from XRD and FactSage modeling, which will be discussed later in this manuscript.

Results and Discussion

Effect of Mechanical Activation on BM Reduction

The PSD of the BM before and after milling from the LCO and NMC is given in Fig. 2. The d10, d50, and d90 values are also listed in Fig. 2. d10 decreases by 10 times in both BM types after 1 h of milling, and a further decrease is not distinguishable with the utilized equipment. The average particle size (d50) for the LCO BM is 0.29 mm in the unmilled sample, which decreases drastically to 0.08, 0.05, and 0.02 mm after 1, 3, and 5 h of milling, respectively. The lowest effect is on the d90 value, which decreases by 40% after 1 h of milling and ~60% after 3 and 5 h. In the NMC BM, d50 and d90 decrease by 96 and 90%, respectively, after 1 h of milling, while longer milling periods do not influence the particle size considerably.

The effect of milling on thermal reactivity was further studied using TGA. Figure 3 shows the mass loss as a
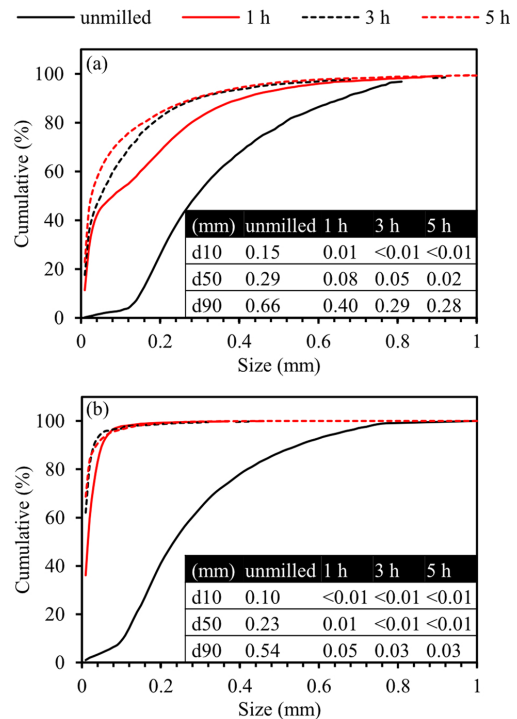

Fig. 2 Cumulative PSD of **a** LCO BM and **b** NMC BM under four conditions: unmilled, milled for 1 h, milled for 3 h, and milled for 5 h

function of temperature at different milling times. Mass loss begins at ~200–300 °C and continues until ~600 °C in both types of BM. The curves of the mixtures with different milling times overlap in this period, while after ~600 °C, they do not follow the same rate, and at a fixed temperature, different mass losses are observed in these samples. As an example, in the LCO BM at 800 °C, a mass loss of 16% occurs in the unmilled samples, which increases to 23% in the samples milled for 1 and 3 h. The mass loss decreases to 19% after milling for 5 h. The change in the NMC BM mass loss, caused by mechanical activation, can be better observed at ~650 °C, where the mass loss is 10% in the unmilled sample and 13, 13, and 17% in the samples milled for 1, 3, and 5 h, respectively. Generally, it can be stated that after 1 h of milling, an increase in the mass loss rate is observed, while 3 h of milling does not cause any changes to the BM compared with the BM milled for 1 h. After 5 h of milling, the mass loss rate in the LCO BM decreases, and in the NMC BM, it increases slightly.
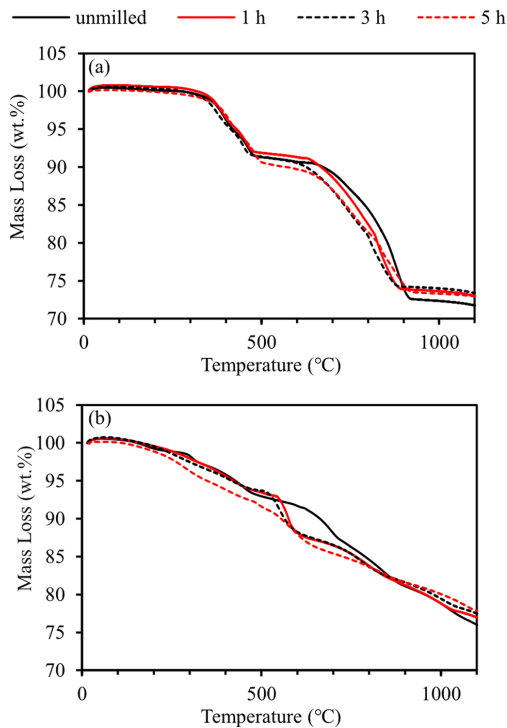
Fig. 3 Mass loss as a function of temperature during the reduction of **a** LCO BM and **b** NMC BM before and after milling for 1, 3, and 5 h

Fig. 4 Mass loss as a function of temperature during the reduction of **a** MixFeLCO and **b** MixFeNMC

The TGA graphs reveal that the main effect of mechanical activation on the reaction kinetics of BM is after 600 °C, which is the temperature at which the cathode material ($LiCoO_2$ in LCO BM and $LiNi_{0.33}Mn_{0.33}Co_{0.33}O_2$ in NMC BM) transforms to simpler oxides [28]. Since the reactions were triggered when the temperature was not constant and it was gradually increasing, the reduction reaction shifted to a lower temperature range. In other words, the increase in the reduction rate, after 600 °C, lowers the temperature of the subsequent reduction of produced oxides (Co and Ni oxides).

Generally, the reduction behaviour of BM with different periods of mechanical activation shows that milling affects the reduction temperature of BM after transformation of the cathode material to its constituent oxides. Regarding the milling periods, it was seen that milling for 1 and 3 h has almost the same effect and shift the reduction to a lower temperature range. Milling for 5 h had an opposite effect in the LCO BM and a negligible effect in the NMC BM.
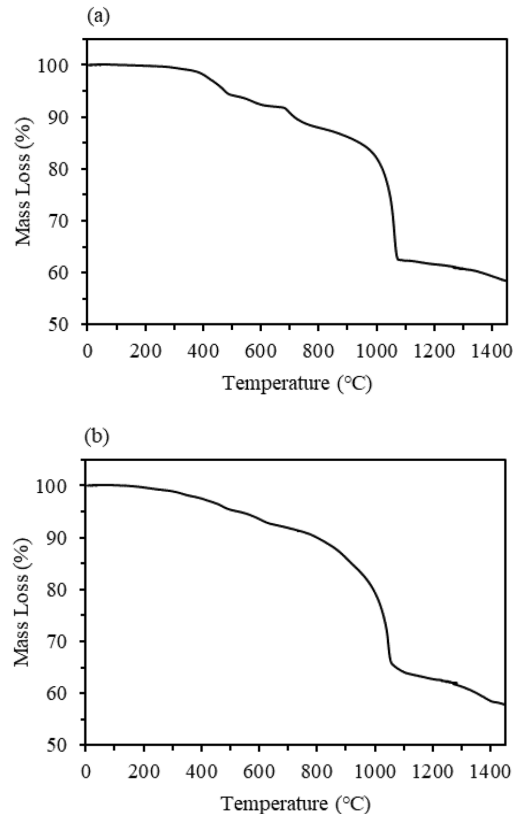
Reduction Behaviour of MeO-BM Mixture

To maximize the utilization of graphite and produce Fe/Cu-based alloys, Fe_2O_3 and CuO were added as described in Table 2.

Iron System

The mass loss during heating of the Fe_2O_3-BM mixture is plotted in Fig. 4. Mass losses of 44 and 43% for MixFeLCO and MixFeNMC are recorded until 1450 °C, respectively. The mass loss begins at 150–200 °C and continues until 1450 °C for both BMs.

The reduction of Fe_2O_3 occurs in multiple steps by reduction to Fe_3O_4, FeO, and finally Fe, which has been explained thoroughly in the literature [30, 31]. All these occurring

reduction reactions result in different slopes in the mass loss trend; since this is not the concern of this study, the details will not be investigated in this article. According to the literature, the reduction of Fe_2O_3 to Fe is complete after reaching a temperature of ~ 1150 °C [30]. The continuation of mass loss at temperatures higher than 1200 °C (with a different mass loss rate) can be attributed to the late reduction of some oxides. This can also be due to the reaction of irreducible oxides (by carbon under the present experimental conditions) such as Li_2O and MnO with F, which produces Li/Mn fluorides and O. O can then react with graphite and produce CO.

FactSage predicts the phases that are thermodynamically stable at 1450 °C. The results are presented in Fig. 5. All Fe_2O_3 is reduced to Fe alloys together with Co (and Ni in MixFeNMC) in the BM. Almost all Li remains in the slag phase (in the form of oxide and fluoride), Mn remains mainly in the oxide form, and the rest forms fluoride. Furthermore, no graphite remains after reduction, which is mainly related to the fact that thermodynamically CO is the only gaseous product of reduction of metal oxides at 1450 °C [28]. However, during the experiment, the reduction begins at lower temperatures where both CO and CO_2 are produced. Compared to CO as a reduction product, CO_2 production consumes less C. Hence, the C analysis indicates that graphite remains in the sample after reduction, which is not in line with the FactSage calculations at 1450 °C.

Copper System

Figure 6 presents the mass loss of the CuO-BM mixture as a function of temperature during heating in a reductive
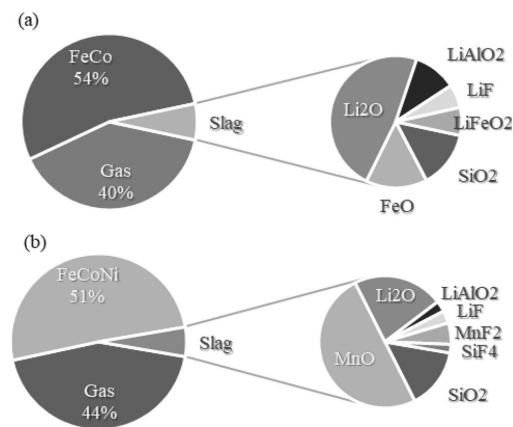

Fig. 5 **a** MixFeLCO and **b** MixFeNMC reduced at 1450 °C, calculated by FactSage: Phase distribution and slag calculated components
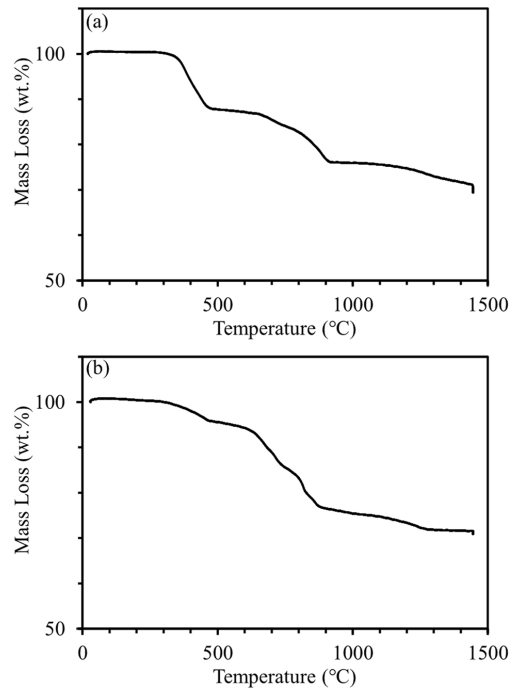
Fig. 6 Mass loss as a function of temperature during the reduction of **a** MixCuLCO and **b** MixCuNMC

atmosphere. 33 and 30% mass losses occur in MixCuLCO and MixCuNMC, respectively. The mass loss starts at ~250 °C and continues until 1450 °C.

Based on FactSage calculations, in the presence of CuO and C, Cu is thermodynamically stable at room temperature. It has been reported that practically, reduction begins at higher temperatures; for instance, 440 °C was reported in a study as the starting point of CuO carbothermic reduction [32]. In general, the reduction starting temperature depends on kinetic factors, such as the heating rate, the particle size, and the contact between the reducing agent and CuO. In the current study, CuO reduction begins at ~300 °C. The change in the mass loss at ~600 °C can be related to the transformation of $LiCoO_2/LiNi_{0.33}Mn_{0.33}Co_{0.33}O_2$ that has been discussed previously. Thermodynamic modeling reveals that Cu begins to melt at ~1000 and ~800 °C in MixCuLCO and MixCuNMC, respectively. The continuation of the mass loss at higher temperatures, as explained in the iron system, can be due to (i) the late reduction of the remaining oxides or (ii) the reaction of the irreducible oxides with F.
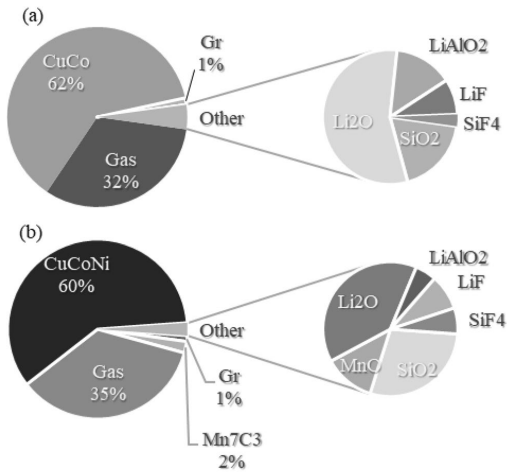
Fig. 7 **a** MixCuLCO and **b** MixCuNMC reduced at 1450 °C, calculated by FactSage: Phase distribution and slag calculated components

According to the results obtained from FactSage calculations at 1450 °C (Fig. 7), Cu-based alloys are the main products of the reduction. It seems that part of the excess graphite in MixCuNMC forms Mn carbide. Generally, in both systems, the slag compositions demonstrate that Li_2O, $LiAlO_2$, and LiF are thermodynamically the Li-containing compounds at that temperature.

Effect of Mechanical Activation on the Reduction of MeO-BM Mixture

TGA of the BM in Sect. "Effect of Mechanical Activation on BM Reduction" showed that milling for 5 h in the LCO BM is not beneficial, and in the NMC BM, is very insignificant, which makes further milling (5 h) unnecessary from an energy point of view. On the other hand, it has been observed that milling for 1 and 3 h has the same effect on the reduction of BM. Accordingly, 5 h of milling was omitted for the mixture of Fe_2O_3 and BM, while the condition of 3 h of milling was kept examining whether it has any significant influence with the addition of MeO.

Iron System

Figure 8 illustrates the mass loss profile of Fe_2O_3-BM mixtures with different periods of milling. The curves show the different behaviours in general. To observe this more specifically, the mass loss of the Fe_2O_3-LCO mixture at 900 °C is
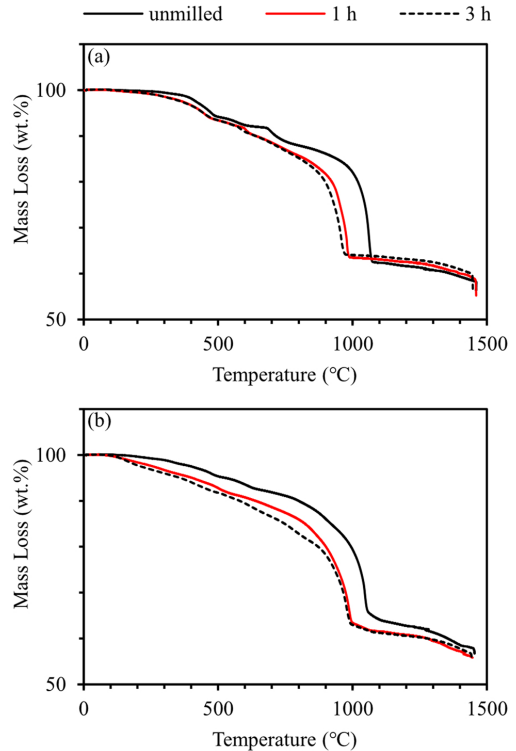

Fig. 8 Mass loss as a function of temperature during the reduction of **a** MixFeLCO and **b** MixFeNMC before and after milling for 1 and 3 h

taken into account. A mass loss of 12% is recorded at that temperature for the unmilled sample, which increases to 18% after milling for 1 h, and the mass loss difference between the mixture milled for 1 h and the one milled for 3 h is only 2%. Considering the same temperature in the Fe_2O_3-NMC mixture, the mass loss increases from 14% in the unmilled mixture to 20 and 22% in the mixtures milled for 1 h and 3 h, respectively. Generally, a significant effect is observed after 1 h of milling, while the effect of milling for 3 h compared to 1 h is negligible.

XRD measurements were performed on several samples with the same composition but different mechanical activation periods. For simplicity, only one measurement for each composition is presented. The reduced samples of mixtures milled for 1 h were selected for XRD measurements. Figure 9 demonstrates the XRD patterns of the
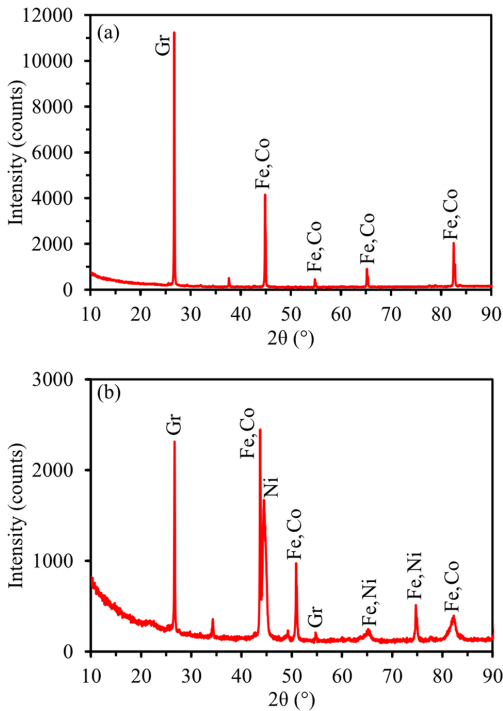
Fig. 9 XRD patterns of reduced **a** MixFeLCO and **b** MixFeNMC milled for 1 h

reduced Fe_2O_3-BM mixtures milled for 1 h. Peaks attributed to graphite (represented as Gr in the graphs) and metallics such as Fe, Co, and Ni are detected in these patterns. The interaction of the Fe matrix with Cu-tube radiation should also be taken into consideration. This interaction leads to fluorescence that increases the background level; hence, it is not reliable to compare the peak intensities in the pattern [33].

The chemical composition of unmilled and milled mixtures after reduction is listed in Table 3. The main elements

in the BM plus Fe in the added MeO are considered as the main elements, and the rest are reported as *other*. The main effect can be observed for the amount of C remaining in the reduced mixture, which increases with increasing milling time. The remaining C is almost constant after 1 and 3 h of milling.

The results in Fig. 8 show that mechanical activation affects the reduction rate after ~600 °C, and this effect continues to the temperature of ~1100 °C. Jung and Yi [30] stated that the reduction of FeO to Fe is completed at 1147 °C, the temperature at which the milling effect ends based on Fig. 8 [30].

The XRD patterns in Fig. 9 show that Fe-based alloy and graphite are both present in the sample. The chemical analysis of unmilled reduced mixtures (Table 3) also shows that C remains after reduction. It can be perceived that although Fe_2O_3 was added based on the C:O molar ratio of one, the graphite in the BM is capable of reducing more oxide. By increasing the milling time (especially after 1 h) and consequently decreasing the temperature range in which the reduction takes place, the amount of excess C (remained after reduction) increases. To explain this matter, the Boudouard reaction should be taken into account, which discusses the partial pressure of CO/CO_2 by changing the temperature in Eq. 1. Based on this reaction, by decreasing the temperature, the partial pressure of CO_2 increases. The production of CO_2 in a reduction reaction consumes less C compared to a reaction with CO as a product.

$$C + CO_2 \rightleftharpoons 2CO \tag{1}$$

To investigate this further, mass and energy calculations were performed to study the effect of a longer milling time on the required heat input for the system. Furthermore, the CO and CO_2 contents in the off-gas were calculated using the final excess carbon as a variable. The calculation results are shown in Fig. 10. The modeling indicates that by increasing the milling time, there is a decrease in the required input heat flow, which is accompanied by a decrease in CO and an increase in CO_2 content in the off-gas. This is what was expected from the TGA results (Fig. 4), i.e., by increasing the reduction rate, the reduction takes place in a lower

Table 3 Chemical composition of unmilled and milled Fe_2O_3-BM mixtures after reduction at 1450 °C

Mixture	Milling time	Chemical composition						
		Fe	Co	Mn	Ni	C	Li	Other
MixFeLCO	Unmilled	63.4 ± 0.2	26.9 ± 0.0	0.0	0.0	3.2 ± 0.0	2.3 ± 0.5	4.2
	1 h	62.7 ± 0.3	26.3 ± 0.0	0.0	0.0	6.0 ± 0.2	1.5 ± 0.3	3.4
	3 h	61.1 ± 1.0	26.1 ± 0.4	0.0	0.0	6.8 ± 0.1	2.5 ± 0.5	3.5
MixFeNMC	Unmilled	68.9 ± 0.0	8.2 ± 0.0	6.5 ± 0.0	7.5 ± 0.0	3.5 ± 0.0	2.5 ± 0.5	2.9
	1 h	70.5 ± 0.5	6.2 ± 0.1	5.2 ± 0.0	6.0 ± 0.1	7.6 ± 0.4	2.3 ± 0.5	2.3
	3 h	69.5 ± 0.9	6.4 ± 0.1	5.4 ± 0.1	6.1 ± 0.1	7.7 ± 0.3	2.9 ± 0.6	2.0

temperature range, which requires lower energy input. In addition, both the experimental and modeling results show that by increasing the milling time the CO/CO$_2$ ratio decreases and the final excess C increases.

Mass and energy balance simulations were also used to estimate the effect of milling on the CO$_2$ emissions of the process. The results of this estimation for MixFeLCO and MixFeNMC systems are presented in Fig. 11, in which the emissions are shown separately for direct emissions from the process (i.e., Scope I) and for indirect emissions from the energy production (i.e., Scope II). For Scope II emissions, specific CO$_2$ emissions of 0.820 kg/kWh, 0.030 kg/kWh and 0.012 kg/kWh were used for energy produced from fossil, renewable and nuclear sources, respectively [34]. The percentage values shown in the Fig. 13 indicate the reduction of CO$_2$ emissions due to milling in different cases.

The calculated exergy balances are depicted in Fig. 12. During the reduction of unmilled MixFeLCO, exergy emission is 2.27×10^5 kJ, which decreases to 2.09×10^5 and 2.04×10^5 kJ after 1 and 3 h of milling, respectively. This change in the reduction of MixFeNMC is from 2.40×10^5 kJ in the unmilled mixture to 2.15×10^5 and 2.14×10^5 kJ after 1 and 3 h of milling, respectively.
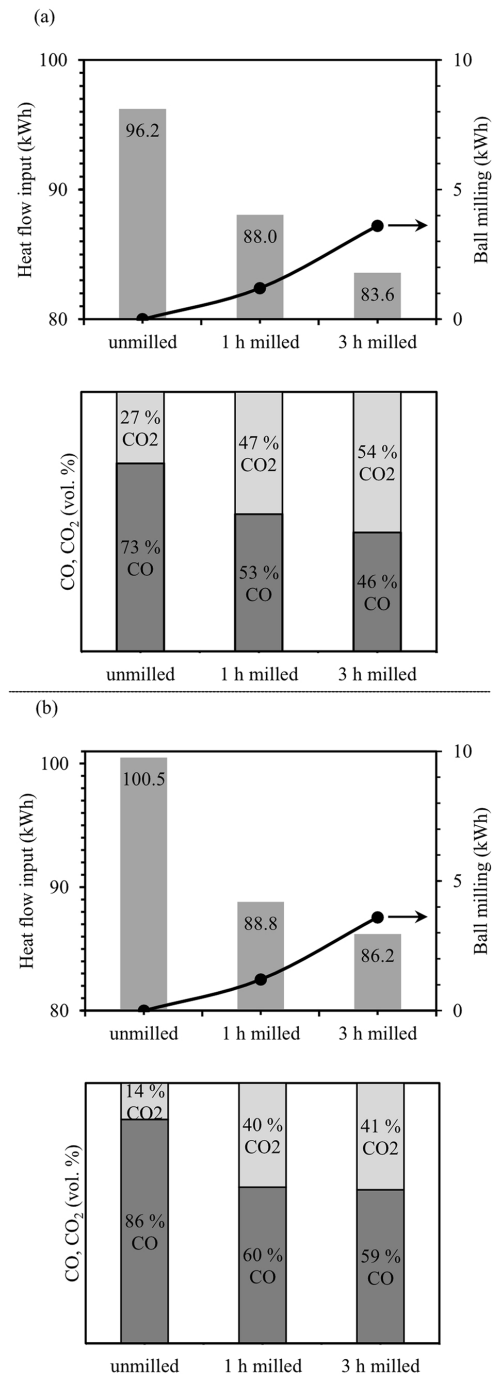
Copper System

As observed in the previous sections, milling for 3 h, compared to 1 h, does not significantly change the mass loss rate of the BM and Fe$_2$O$_3$-BM mixture. Therefore, the condition of 3 h of milling is omitted for the CuO-BM mixtures.

Figure 13 depicts the mass loss of the CuO-BM mixture during heating until 1450 °C. It can be seen that mass loss occurs with a higher rate after milling for 1 h. The effect of mechanical activation is mainly observable in the temperature range of 300–900 °C. For instance, at 700 °C, the mass loss increases by 4% and 11% after 1 h of milling in the LCO-CuO and NMC-CuO mixtures, respectively.

The XRD patterns of the reduced mixtures are presented in Fig. 14. Similar to what was observed in the iron system, in addition to graphite peaks, they are peaks of metallic phases, including Cu, Co, and Ni (particularly in Mix-CuNMC). The peak intensities in the iron and copper system are not comparable, because of different components, different grindability of materials and the fluorescence effect (even by using monochromator for suppressing the fluorescence) [33].

The chemical composition of the Cu-containing mixtures after reduction is listed in Table 4. The results of the unmilled and milled samples show that mechanical
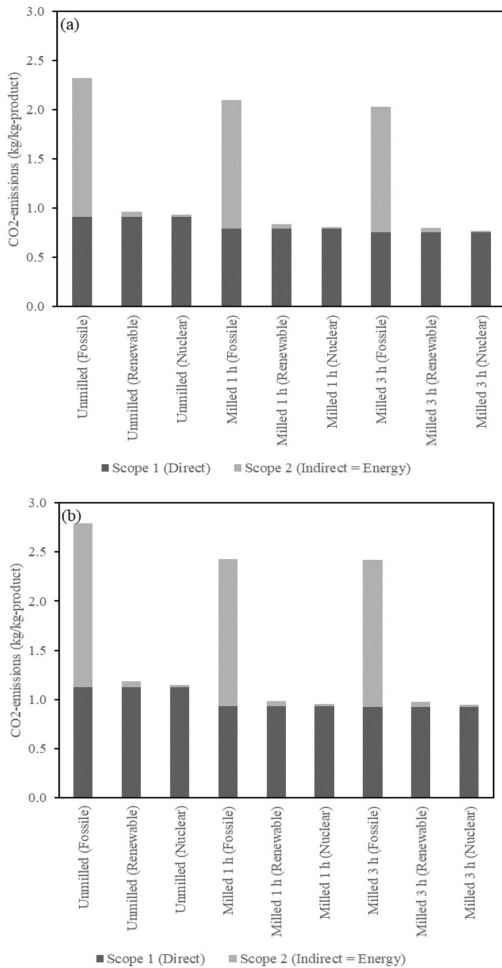
Fig. 11 Specific CO_2 emissions during reduction of **a** MixFeLCO, and **b** MixFeNMC at 1450 °C, calculated by HSC chemistry

Fig. 12 Calculated exergy balance of **a** MixFeLCO, and **b** MixFeNMC reduction at 1450 °C

is almost no change after mechanical activation at higher temperatures. Generally, mechanical activation changes the surface properties of solid particles. When the system's main component melts, there is no other solid surface, and thus mechanical activation no longer affects the reaction kinetics.

Figure 15 demonstrates the results from mass and energy balance calculations. Similar to what was discussed in Iron system, milling of the CuO-BM mixture leads to higher reaction rates, which shifts the reduction occur to a lower temperature range; thus, less energy input is required. This also results in a lower CO/CO_2 ratio that increases the final amount of excess C after reduction.

According to what has been discussed for the MeO-BM mixtures, it can be stated that by applying mechanical activation and increasing the reduction rate, the efficiency of the reduction process can be increased. The C in the BM can be used to reduce more MeO, and then a lower temperature is required for the reduction.

activation significantly increases the final C that remains in the sample after reduction.

By comparing the TGA graphs in Fig. 13, it is seen that the mechanical activation affects the system from ~200–300 °C (beginning of CuO reduction) to ~1000 °C (MixCuLCO) and ~800 °C (MixCuNMC), where Cu begins to melt according to FactSage calculations. There
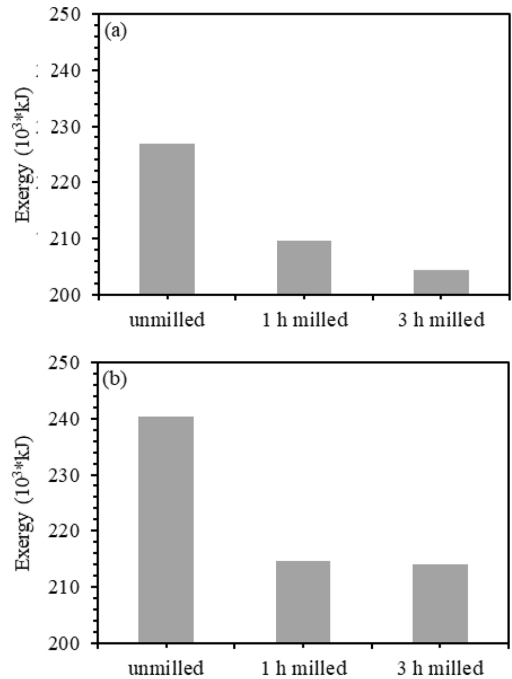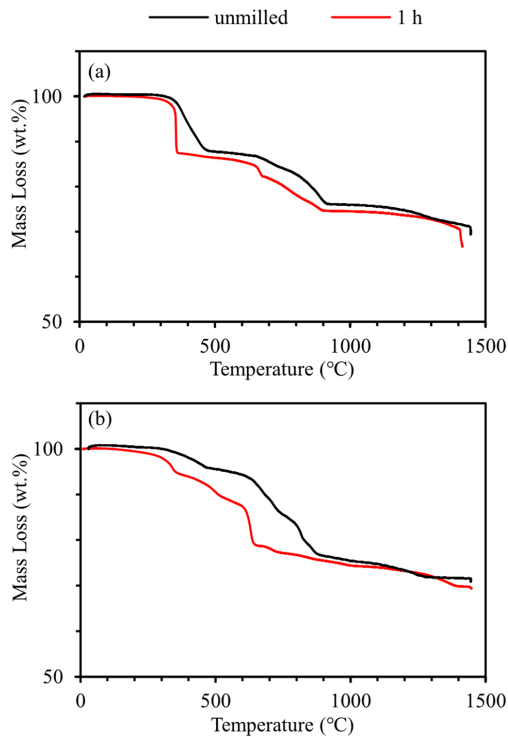
Fig. 13 Mass loss as a function of temperature during reduction of **a** MixCuLCO and **b** MixCuNMC before and after milling for 1 h

Fig. 14 XRD patterns of reduced **a** MixCuLCO and **b** MixCuNMC milled for 1 h

Mass and energy balance simulations were also used to estimate the effect of milling on the CO_2 emissions of the process. The results of this estimation for MixCuLCO and MixCuNMC systems are presented in Fig. 16, in which the emissions are shown separately for direct emissions from the process (i.e. Scope I) and for indirect emissions from the energy production (i.e. Scope II). For Scope II emissions, specific CO_2 emissions of 0.820 kg/kWh, 0.030 kg/kWh and 0.012 kg/kWh were used for energy produced from fossil, renewable and nuclear sources, respectively

[34]. The percentage values shown in the Fig. 16 indicate the reduction of CO_2 emissions due to milling in different cases.

Exergy balance has been calculated in the Cu mixtures. As shown in Fig. 17, the exergy emission is 1.23×10^5 kJ for the reduction of unmilled MixCuLCO, which decreases to 0.67×10^5 kJ after an hour of milling. In the

Table 4 Chemical composition of unmilled and milled CuO-BM mixtures after reduction at 1450 °C

| Mixture	Milling time	Chemical composition						
		Cu	Co	Mn	Ni	C	Li	Other
MixCuLCO	Unmilled	70.5±0.2	25.0±0.0	0.1±0.0	0.1±0.0	0.9±0.1	1.4±0.4	2.0
	1 h	70.5±0.1	17.0±0.1	0.0	0.0	8.9±0.0	1.9±0.6	1.8
MixCuNMC	Unmilled	84.9±0.8	4.4±0.0	3.2±0.0	3.5±0.0	2.0±0.7	1.3±0.4	0.7
	1 h	76.4±0.3	3.7±0.0	3.2±0.0	3.4±0.0	10.5±0.3	1.6±0.5	0.9

Fig. 15 Energy consumption and CO/CO₂ production during the ▶ reduction of **a** MixCuLCO and **b** MixCuNMC at 1450 °C, calculated by HSC chemistry

MixCuNMC, an hour of milling changes the exergy loss from 1.06×10^5 to 0.46×10^5 kJ.

Comparing to the iron system (Fig. 10), it has been seen in the copper system that mechanical activation has a more significant effect on lowering the required input energy. To explain, thermodynamics and kinetics of the reactions should be both taken into account. From the thermodynamic point of view, the reduction of CuO to metallic Cu is feasible at room temperature, while reduction of Fe_2O_3 requires elevated temperatures. Hence, the only factor that postpones the reduction of CuO to higher temperatures is kinetics of the reaction. Because of that, changing the kinetic parameters (decreasing the particle size) has a more significant effect on the copper system comparing to the iron system. By increasing the reduction rate, reduction shifts to a lower temperature range, which increases the CO_2/CO ratio. This results in consumption of a lower amount of C that equals to consumption of lower chemical energy, and consequently saving more energy.

Conclusions

In this research, it was attempted to address some of the major downsides of pyrometallurgical methods in recovering metallic elements from LIB BM: graphite loss, high energy consumption, and CO_2 emission. To avoid graphite loss, the feasibility of alloy making using BM was investigated by the addition of Fe_2O_3 and CuO to two types of BM (LCO and NMC). Regarding high energy consumption and CO_2 emission, mechanical activation was proposed as a solution. The experimental work showed that by adding MeO to BM (with a total C/O ratio of one), the added MeO was completely reduced to the metallic form, where Co (and Ni in NMC BM) would also be reduced. It was observed that mechanical activation increases the reduction rate; accordingly, the reduction reactions shift to a lower temperature range, and consequently, less energy is required for the reduction of BM and MeO-BM mixture. Another consequence of mechanical activation is that by lowering the temperature
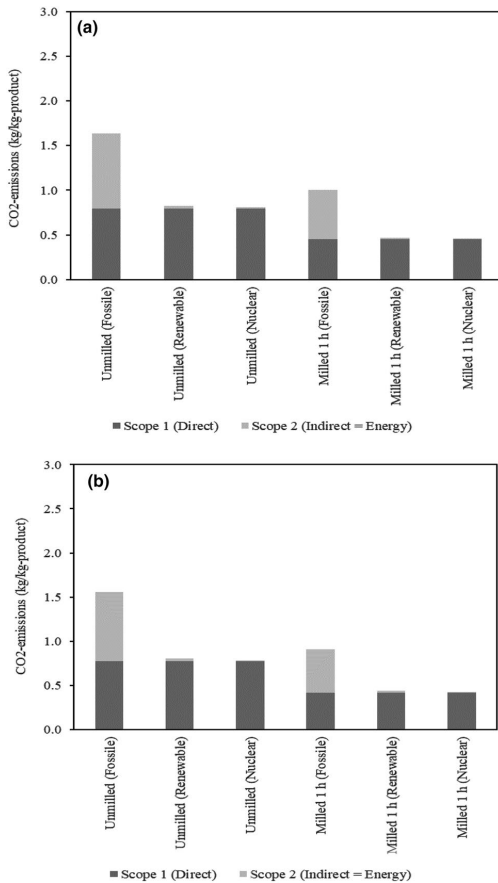
(a)

(b)
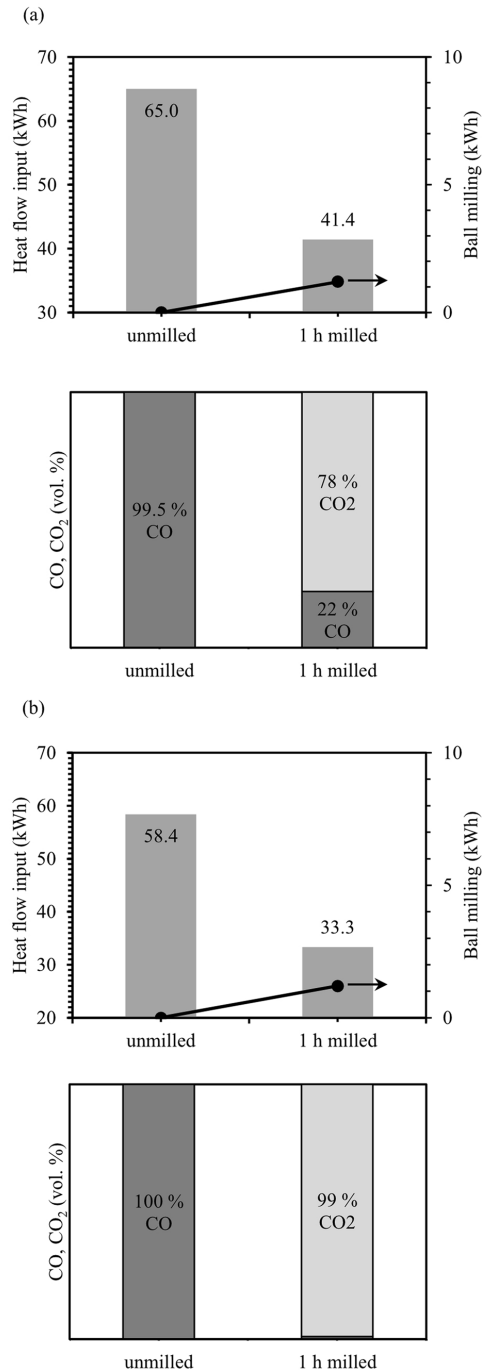
Fig. 16 Specific CO_2 emissions during reduction of **a** MixCuLCO, and **b** MixCuNMC at 1450 °C, calculated by HSC chemistry

range that reduction takes place, the ratio of CO_2/CO (as reduction products) increases, which leads to consumption of lower amount of C and lower total CO_2 emission. This effect increases the C remaining in the system. In general, mechanical activation enables the reduction of more MeO by the BM and decreases the energy consumption and CO_2 emission.
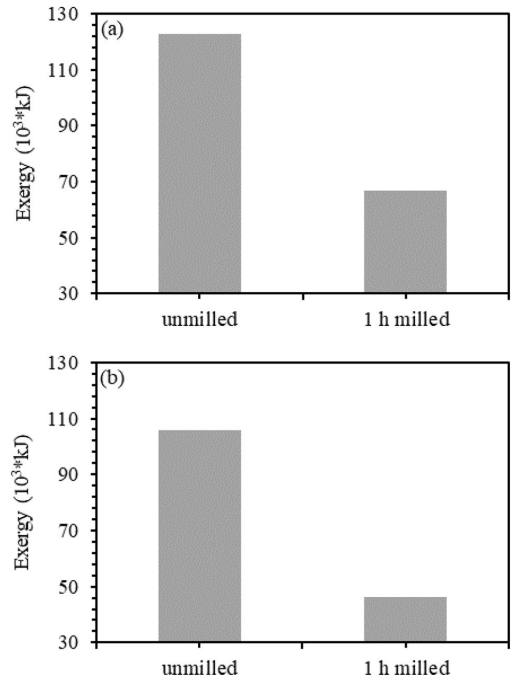

Fig. 17 Calculated exergy balance of **a** MixCuLCO, and **b** MixCuNMC reduction at 1450 °C

Declarations

Conflict of interest On behalf of all authors, the corresponding author states that there is no conflict of interest.

References

1. Kawamura H, LaFleur M, Iversen K, Cheng HWJ (2021) Lithium-ion batteries: a pillar for a fossil fuel-free economy. United Nations, Frontier Technology Issues, pp 1–10. https://www.un.org/development/desa/dpad/wp-content/uploads/sites/45/publication/FTI_July2021.pdf

2. Fan E, Li L, Wang Z, Lin J, Huang Y, Yao Y, Chen R, Wu F (2020) Sustainable recycling technology for li-ion batteries and beyond: challenges and future prospects. Chem Rev 120(14):7020–7063. https://doi.org/10.1021/acs.chemrev.9b00535

3. IEA (2020) Innovation in batteries and electricity storage. https://www.iea.org/reports/innovation-in-batteries-and-electricity-storage

4. The European Parliament and of the Council (2006) Directive 2006/66/EC of the European Parliament and of the Council of 6 September 2006 on batteries and accumulators and waste batteries and accumulators and repealing Directive 91/157/EEC. Official Journal of the European Union.

5. European Comission (2020) Critical raw materials resilience: charting a path towards greater security and sustainability. https://eur-lex.europa.eu/legal-content/EN/TXT/?uri=CELEX:52020DC0474

6. Pinegar H, Smith YR (2019) Recycling of end-of-life lithium ion batteries, Part I: commercial processes. J Sustain Metall 5(3):402–416. https://doi.org/10.1007/s40831-019-00235-9

7. Makuza B, Tian Q, Guo X, Chattopadhyay K, Yu D (2021) Pyrometallurgical options for recycling spent lithium-ion batteries: a comprehensive review. J Power Sources 491:229622. https://doi.org/10.1016/j.jpowsour.2021.229622

8. Pinegar H, Smith YR (2020) Recycling of end-of-life lithium-ion batteries, Part II: laboratory-scale research developments in mechanical, thermal, and leaching treatments. J Sustain Metall 6(1):142–160. https://doi.org/10.1007/s40831-020-00265-8

9. Meshram P, Pandey BD, Mankhand TR (2014) Hydrometallurgy Extraction of lithium from primary and secondary sources by pre-treatment, leaching and separation: a comprehensive review. Hydrometallurgy 150:192–208. https://doi.org/10.1016/j.hydromet.2014.10.012

10. Or T, Gourley SWD, Kaliyappan K, Yu A, Chen Z (2020) Recycling of mixed cathode lithium-ion batteries for electric vehicles: current status and future outlook. Carbon Energy 2(1):6–43. https://doi.org/10.1002/cey2.29

11. Velázquez-Martínez O, Valio J, Santasalo-Aarnio A, Reuter M, Serna-Guerrero R (2019) A critical review of lithium-ion battery recycling processes from a circular economy perspective. Batteries 5(4):68. https://doi.org/10.3390/batteries5040068

12. Mossali E, Picone N, Gentilini L, Rodrìguez O, Pérez JM, Colledani M (2020) Lithium-ion batteries towards circular economy: a literature review of opportunities and issues of recycling treatments. J Environ Manage 264:110500. https://doi.org/10.1016/j.jenvman.2020.110500

13. Zheng X, Zhu Z, Lin X, Zhang Y, He Y, Cao H, Sun Z (2018) A mini-review on metal recycling from spent lithium ion batteries. Engineering 4(3):361–370. https://doi.org/10.1016/j.eng.2018.05.018

14. Hanisch C, Loellhoeffel T, Diekmann J, Markley KJ, Haselrieder W, Kwade A (2015) Recycling of lithium-ion batteries: a novel method to separate coating and foil of electrodes. J Clean Prod 108:301–311. https://doi.org/10.1016/j.jclepro.2015.08.026

15. Hu X, Mousa E, Ye G (2021) Recovery of Co, Ni, Mn, and Li from Li-ion batteries by smelting reduction—Part II: a pilot-scale demonstration. J Power Sources 483:229089. https://doi.org/10.1016/j.jpowsour.2020.229089

16. Lombardo G, Ebin B, Foreman MR, Steenari BM, Petranikova M (2020) Incineration of EV Lithium-ion batteries as a pretreatment for recycling—determination of the potential formation of hazardous by-products and effects on metal compounds. J Hazard Mater 393(January):122372. https://doi.org/10.1016/j.jhazmat.2020.122372

17. Diaz F, Wang Y, Moorthy T, Friedrich B (2018) Degradation mechanism of nickel-cobalt-aluminum (NCA) cathode material from spent lithium-ion batteries in microwave-assisted pyrolysis. Metals 8(8):565. https://doi.org/10.3390/met8080565

18. Kwon OS, Sohn I (2020) Fundamental thermokinetic study of a sustainable lithium-ion battery pyrometallurgical recycling process. Resour Conserv Recycl 158:104809. https://doi.org/10.1016/j.resconrec.2020.104809

19. Lombardo G, Ebin B, St Foreman MRJ, Steenari BM, Petranikova M (2019) Chemical transformations in Li-ion battery electrode materials by carbothermic reduction. ACS Sustain Chem Eng 7(16):13668–13679. https://doi.org/10.1021/acssuschemeng.8b06540

20. Sommerfeld M, Vondersteln C, Dertmann C, Klimko J, Oráč D, Miškufová A, Havlík T, Friedrich B (2020) A combined pyro-and hydrometallurgical approach to recycle pyrolyzed lithium-ion battery black mass part 1: Production of lithium concentrates in an electric arc furnace. Metals 10(8):1–27. https://doi.org/10.3390/met10081069

21. Hu H, Chen Q, Yin Z, Zhang P (2003) Thermal behaviours of mechanically activated pyrites by thermogravimetry (TG). Thermochim Acta 398(1–2):233–240. https://doi.org/10.1016/S0040-6031(02)00390-8

22. Hu H, Chen Q, Yin Z, Zhang P, Ye L (2003) The thermal behaviour of mechanically activated galena by thermogravimetry analysis. Metall Mater Trans A 34(13):793–797. https://doi.org/10.1007/s11661-003-1007-y

23. Hu H, Chen Q, Yin Z, Zhang P, Zou J, Che H (2002) Study on the kinetics of thermal decomposition of mechanically activated pyrites. Thermochim Acta 389(1–2):79–83. https://doi.org/10.1016/S0040-6031(01)00850-4

24. Kosmac T, Courtney TH (1992) Milling and mechanical alloying of inorganic nonmetallics. J Mater Res 7(6):1519–1525. https://doi.org/10.1557/JMR.1992.1519

25. Pourghahramani P, Forssberg E (2007) Reduction kinetics of mechanically activated hematite concentrate with hydrogen gas using nonisothermal methods. Thermochim Acta 454(2):69–77. https://doi.org/10.1016/j.tca.2006.12.023

26. Zdujić M, Jovalekić Č, Karanović L, Mitrić M, Poleti D, Skala D (1998) Mechanochemical treatment of α-Fe2O3 powder in air atmosphere. Mater Sci Eng, A 245(1):109–117. https://doi.org/10.1016/s0921-5093(97)00715-6

27. Welham NJ (2002) Activation of the carbothermic reduction of manganese ore. Int J Miner Process 67(1–4):187–198. https://doi.org/10.1016/S0301-7516(02)00045-5

28. Babanejad S, Ahmed H, Andersson C, Samuelsson C, Lennartsson A, Hall B, Arnerlöf L (2022) High-temperature behaviour of spent Li-ion battery black mass in inert atmosphere. J Sustain Metall 8(1):566–581. https://doi.org/10.1007/s40831-022-00514-y

29. Bale CW, Bélisle E, Chartrand P, Decterov SA, Eriksson G, Gheribi AE, Hack K, Jung IH, Kang YB, Melançon J, Pelton AD, Petersen S, Robelin C, Sangster J, Spencer P, Ende M.-A. Van (2016) FactSage thermochemical software and databases—2010–2016. Calphad 54:35–53

30. Jung SM, Yi SH (2013) A kinetic study on carbothermic reduction of hematite with graphite employing thermogravimetry and quadruple mass spectrometry. Steel Res Int 84(9):908–916. https://doi.org/10.1002/srin.201200310

31. Szendrei T, Van Berge PC (1981) Thermogravimetry and evolved gas analysis of the reduction of hematite (Fe2O3) with graphite. Thermochim Acta 44(1):11–19. https://doi.org/10.1016/0040-6031(81)80266-3

32. Kirakosyan H, Minasyan T, Niazyan O, Aydinyan S, Kharatyan S (2016) DTA/TG study of CuO and MoO3 co-reduction by combined Mg/C reducers. J Therm Anal Calorim 123(1):35–41. https://doi.org/10.1007/s10973-015-4919-z

33. Mos YM, Vermeulen AC, Buisman CJN, Weijma J (2018) X-Ray diffraction of iron containing samples: the importance of a suitable configuration. Geomicrobiol J 35(6):511–517. https://doi.org/10.1080/01490451.2017.1401183

34. World Nuclear Association (2021) Carbon dioxide emissions from electricity. https://www.world-nuclear.org/information-library/energy-and-the-environment/carbon-dioxide-emissions-from-electricity.aspx

Department of Civil, Environmental, and Natural Resources Engineering
Division of Mineral and Metallurgical Engineering (MiMeR)

LULEÅ
UNIVERSITY
OF TECHNOLOGY